

**TRANSPORT AND MAGNETIC PROPERTIES OF
YBCO SUPERCONDUCTORS WITH
Mn AT *Cu* SITE**

DOCTOR OF PHILOSOPHY

E. ISAAC SAMUEL EDWIN



**SCHOOL OF PHYSICS
UNIVERSITY OF HYDERBAD
HYDERABAD - 500 046
INDIA**

September 1999

To

..... *My Lord*

..... ***My Savior***

..... ***& My Friend***

JESUS CHRIST

DECLARATION

I hereby declare that the work embodied in this thesis entitled "**Transport and Magnetic Properties of *YBCO* superconductors with *Mn* at *Cu* Site**" has been carried out by me under the supervision of Dr. V. Seshu Bai at the School of Physics, University of Hyderabad, Hyderabad. And this work has not been submitted to any other University for the award of any degree or diploma.

Date: Sept. 14, 1999

Place : Hyderabad



(E. ISAAC SAMUEL)

CERTIFICATE

This is to certify that the work embodied in this thesis **entitled** **"Transport and Magnetic Properties of YBCO Superconductors with Mn at Cu Site"** has been carried out by *Mr E. ISAAC SAMUEL EDWIN* **under my** supervision and the same has **not been submitted for the award of any degree or diploma in any other University.**


Date: 16-9-99

Place : Hyderabad

V. Seshu Bai

(Dr. V. SESHUBAI)

Research Supervisor


DEAN
SCHOOL OF PHYSICS
UNIVERSITY OF HYDERABAD

ACKNOWLEDGEMENTS

 My heart felt thanks to.....

Dr. V. Seshu Bai - for the guidance, encouragement and the wide lab facilities, also for her personal care and interest.

Prof. A.K.Bhatnagar, the Dean and Prof. K. N. Shrivastava and Prof. A. Pathak, former Deans - for allowing me to avail the school facilities.

Dr. Placid Rodriguez, Director, IGCAR, Dr. S. L. Mannan, Associate Director, Materials Development Group and Dr. K. Bhanu Sankara Rao, Head, Mechanical Metallurgy Division, IGCAR, Kalpakkam, - for their interest in this work and permitting me to submit this thesis.

Dr. T. Rajasekharan, DMRL, Hyderabad, - for the many helpful discussions and for extending the facilities of DMRL in sample preparation and characterization.

Dr. V. Ganesan, IUC DAEF, Indore - for providing the Seebeck coefficient measurement facility

Prof. S. K. Malik, TIFR, Mumbai - for providing DC magnetization measurement facility

My labmates, colleagues and friends - for the useful chats, for the helping hands and for adding the cherishing moments.

CIL staffs, school of Physics lab assistants - for the various technical assistance.

Office staffs of School of Physics, especially Mr. Abraham - for their consistent assistance at different times and needs.

UGC - for the financial assistance.

Parents, sisters and family - for the love, prayers and support.

GOD, who alone is wise - for providing the grace that was sufficient in all things.



(E. ISAAC SAMUEL)

PREFACE

With many potential applications, study of high temperature superconductors (HTSC) is still a hot subject eluding proper understanding. Following the discovery of superconductivity in ceramic *La-Ba-Cu-O* system in 1986 by Bednorz and Muller, Copper Oxide family of superconductors has added new challenges and promises to this field. This family of superconductors includes *Y-Ba-Cu-O* (YBCO), *Bi-Sr-Ca-Cu-O* (BSCCO), *Tl-Ba-Ca-Cu-O* (TBCCO) and *Hg-Ba-Ca-Cu-O* (HBCCO) systems. Detailed investigations on these HTSC materials, involving modification of their compositions through doping or additions and also the process of synthesis, are essential to widen their technological applicability, overcoming the technical difficulties. Hence the scientific interests in high temperature superconductivity can be classified under two main categories *via*. understanding the phenomena of superconductivity and optimization of superconducting properties for practical applications. Doping studies aid these goals in different ways. Primarily, doping into a parent compound may enhance or deteriorate the superconductivity of the parent compound thereby giving a clue to the origin of superconductivity in it. Secondly, doping may modify the field and temperature variations of physical properties to be more suitable for applications.

YBCO has proved to be of technological importance among the family of HTSC with its phase stability, chemical adaptability and high critical current density. Doping studies on the YBCO system without altering the parent structure can be done at V-site by Lanthanides, Ba-site by elements such as Lanthanum, Strontium, *etc.* and Cu-site by essentially 3-d elements. One of the established views is about the important role of Cu-O layer in the superconductivity of the high temperature ceramic cupric superconductors. In an orthorhombic $YBa_2Cu_3O_{7-x}$ crystal, while the CuO chain along the *b*-axis acts as a charge reservoir, the CuO_2 sheet in the *ab* plane acts as the conduction plane for the superconducting electrons. It is this fact that makes studies on doping at Cu site important for the understanding of superconductivity in these cuprates. Fe and Co are known to occupy Cu(I) site along the *b*-axis, whereas Ni and Zn are known to take Cu(II) site in the *ab* plane. Of these dopants Zn had been found to decrease T_c drastically at a rate of almost 10 K/at.% doping. Unlike in the conventional superconductors, magnetic pair breaking caused by the magnetic impurity is known to have least effect on HTSC but the local disorder introduced by the substituents in the CuO_2 plane can kill the superconductivity even at low doping levels, as in the case of Zn. Due to low solubility

limit a detailed study on the effect of *Mn* at *Cu* site is scarcely found in the literature. *Mn* with its higher magnetic moment is known to occupy *Cu(I)* site from the neutron diffraction experiments. But T_c remains least altered, indicating the magnetic pair breaking to be insignificant in this system. Hence this system with doping of *Mn* having high magnetic moment was taken up for detailed study.

Organization of the Thesis is as follows:

The first chapter introduces the field of superconductivity and presents a detailed account of the effect of various substituents on the properties of YBCO, as is known from literature.

The second chapter deals with the details of sample preparation and their characterization through XRD, temperature variation of resistivity and susceptibility. The experimental details of the characterization techniques are also discussed.

The third chapter on the transport study explains the temperature variation of resistivity and the Seebeck coefficient measurements. From the temperature variation of resistivity, the effect of dopant concentration on the transition temperature and width and the normal state resistivity are discussed. The normal state Seebeck coefficient data is analyzed in terms of various models such as metallic diffusion model, Nagaosa Lee model and Gasumyants narrow band model and the parameters obtained are discussed.

The fourth chapter begins with the details of the theoretical modeling, which is used in analyzing the magnetic properties. This chapter further can be grouped into three sections namely (a) the temperature and field variation of ac susceptibility, (b) DC SQUID magnetization measurements and (c) ac MH loops. The magnetic parameters such as H_{c1} , J_c , H_c^* , flux profile (ρ/R) and losses respectively for the grain and intergranular region derived from various measurements are discussed and correlated. The intergranular properties show a strong influence of microstructural features that shadow the variation with Mn content. The grain properties vary systematically with dopant concentration. This could be because the nature of the intergranular regions is highly process dependent.

Finally, the fifth chapter summarizes the results and the puts forth the conclusions made from the various studies presented in this thesis.

Table of Contents

INTRODUCTION	1
1.1 THEORIES	4
1.2 JOSEPHSON EFFECT	7
1.3 HIGH TEMPERATURE SUPERCONDUCTORS	a
1.3.1 STRUCTURE OF YBCO	8
1.3.2 SUBSTITUTIONAL STUDIES:	11
1.4 REFERENCES:	15
SAMPLE PREPARATION AND CHARACTERIZATION	18
2.1 SAMPLE PREPARATION :	19
2.2 CHARACTERIZATION TECHNIQUES :	19
2.2.1 X - RAY DIFFRACTION :	20
2.2.2 MICROSTRUCTURE :	20
2.2.3 DC RESISTIVITY :	20
2.2.4 AC SUSCEPTIBILITY :	23
2.3 SAMPLE CHARATERIZATION :	27
2.3.1 SAMPLES STUDIED :	27
2.3.2 TEMPERATURE DEPENDENCE OF DC ELECTRICAL RESISTIVITY :	33
2.3.3 TEMPERATURE VARIATION OF AC SUSCEPTIBILITY :	35
2.4 REFERENCES :	36
TRANSPORT PROPERTIES	37
3.1 RESISTIVITY :	39
3.1.1 RESULTS AND DISCUSSION :	40
3.2 SEEBECK COEFFICIENT:	42
3.2.1 EXPERIMENTAL	44
3.2.2 RESULTS AND DISCUSSIONS:	45
3.3 REFERNECES:	55

4.1	ANALYTICAL FRAME WORK	59
4.1.1	GRANULAR SUPERCONDUCTOR :	61
4.1.2	NUMERICAL PROCEDURE:	62
4.2	TEMPERATURE AND FIELD VARIATIONS OF AC SUSCEPTIBILITY	66
4.2.1	EXPERIMENTAL:	66
4.2.2	TEMPERATURE VARIATION OF AC SUSCEPTIBILITY:	67
4.2.3	TEMPERATURE DEPENDENT AC LOSS :	67
4.2.4	FIELD VARIATION OF AC SUSCEPTIBILITY:	79
4.3	DC MAGNETIC PROPERTIES :	84
4.3.1	EXPERIMENTAL:	85
4.3.2	RESULTS AND DISCUSSION:	85
4.4	AC MH LOOPS:	94
4.4.1	EXPERIMENTAL:	95
4.4.2	RESULTS AND DISCUSSION:	96
4.5	REFERENCES:	109

SUMMARY & CONCLUSIONS	112
----------------------------------	------------

5.1	TRANSPORT PROPERTIES:	113
5.1.1	RESISTIVITY:	114
5.1.2	SEEBECK COEFFICIENT :	114
5.2	MAGNETIC PROPERTIES :	115
5.2.1	TEMPERATURE AND FIELD VARIATION OF AC SUSCEPTIBILITY :	115
5.2.2	DC MAGNETIZATION :	117
5.2.3	AC MH LOOP:	117

CHAPTER - 1

INTRODUCTION

The twentieth century has been a century of discoveries and inventions that had transformed human life style and understanding to a great extent. Nevertheless, many of the phenomena are yet to be unveiled completely. Among such stands the superconductivity which was discovered way back in 1911 by Kammerling Onnes [1] as a consequence of his invention of liquefaction of Helium. It has taken almost half a century to learn different characteristics associated with it such as Meissner effect (1933) and Josephson effect (1963).

The phenomenon of superconductivity as understood today is characterized not only by the zero resistivity (to the limit of measuring sensitivity) below a critical temperature T_c but also by a perfect diamagnetism in that high conducting state which was discovered by Meissner and Ochsenfeld and referred to as *Meissner effect*. This is contrary to the predictions of Maxwell's equation $\nabla \times \mathbf{E} = \partial \mathbf{B} / \partial t$, according to which in a perfect conducting state $\mathbf{E} = 0$ and so $\partial \mathbf{B} / \partial t$ will be zero i.e. the magnetic flux density within a perfect conductor will depend on its history. This differentiates a superconductor from a perfect conductor that possesses infinite conductivity alone. Another basic

implication of the Meissner effect is that the superconducting state is a thermodynamic phase. Thus superconductor is a distinct phase of matter with its characteristic thermodynamic and physical properties [2].

The important physical properties are zero resistivity and Meissner effect. In the presence of a magnetic field, as the superconductor is cooled below T_c , it expels the magnetic flux from within. But inspite of the energy spent on expelling the flux, the superconductor must be in a lower energy state than being in normal state to be a stable phase. This superconducting condensation energy can be given as

$$g_n(T, H) - g_s(T, 0) < \mu_0 \int_0^H M \cdot dH \quad (1.1)$$

Consequently, if the applied magnetic field is higher than a critical value the energy required to expel the flux may be more than the condensation energy across the superconducting transition. This critical field above which the superconductivity is quenched is called the *critical magnetic field* (H_c). Also the observed zero resistivity in a superconductor is destroyed if the current density exceeds a critical value called *critical current density* (J_c). Thus the superconductor is stable only within these three boundary values in Temperature, Magnetic field and Current density scales. Any increase in one of these variables reduces the other two critical parameters.

The zero flux density inside a superconductor can be represented as

$$B = \mu_0 (\vec{H} + \vec{M}) = 0 \quad (1.2)$$

where H is the applied magnetic field and M is the intensity of magnetization. Writing magnetization in terms of susceptibility (χ), we have

$$B = \mu_r \mu_0 \cdot \vec{H} \quad \mu_0 \cdot \vec{H} (1 + \chi) \quad (1.3)$$

Hence we get $M = -H$ or $\chi = -1$ for the flux density inside the superconductor to be zero. This magnetization (magnetic moment per unit volume) observed in the superconducting state is too high to be accounted for by local dipoles. This can be understood in two

ways (a) either the superconductor can be supposed to be a bulk diamagnet having zero relative permeability (i.e. $\mu_r = 0$) and hence zero flux density or (b) from Ampere's theorem supercurrents flowing perpendicular to the applied magnetic fields can be inferred which generate fields in such a direction as to cancel the field inside and these supercurrents are hence called *screening currents*. From Maxwell's equation $\nabla \times \mathbf{B} = \mu_0 \mathbf{J}$, when $\mathbf{B} = 0$ at the interior of a superconductor \mathbf{J} will also be zero. Hence any current through a superconductor has to flow only at the surface. The distribution of current on the surface of a superconducting metal is analogous to the electrostatic charge distribution on a conducting body. And the distribution of supercurrent on the surface of a perfectly diamagnetic superconductor has the same form as that of the electrostatic charge distribution on a charged conductor of the same shape.

However, the screening currents flowing at the surface cannot be confined strictly to the surface but die over a distance called *penetration depth* (λ). Thus the magnetic flux density also diminishes over this distance from the surface of the superconductor. Penetration depth is one of the intrinsic properties of a superconductor, which asymptotically increases at T_c . Another intrinsic length associated with a superconductor is the length over which the coherence of the superconducting order parameter occurs across a normal-superconductor phase boundary, called *Coherence length* (ξ).

Alexi Abrikosov discovered that in some superconductors the flux within the sample is expelled completely upto the critical field whereas in some others flux expulsion occurs over a range of fields. The former type of materials is classified as Type I or soft superconductors and the later are classified as Type II or hard superconductors. In a hard superconductor, as the applied field is increased the flux starts penetrating into the superconductor above the *lower critical field* (H_{c1}) and the material becomes completely normal above the *upper critical field* (H_{c2}). Though the lower critical fields in general are low, the upper critical fields are as high as 10^2 T, thus widening the prospective applications of the hard superconductors. There are some fundamental differences in properties between these classes of superconductors. Type I superconductors have positive surface energy whereas the Type II have negative

surface energy. The surface energy will depend on the ratio of the coherence length to the penetration depth.

The negative surface energy of Type II superconductor favors formation of larger superconducting - normal boundary. This leads to a situation, at fields above the lower critical field, where the superconductor is threaded by cylinders of normal regions called *vortices*. The motion of these vortices due to Lorentz force cause energy dissipation which can be effectively arrested by pinning of these vortices by impurities or local non-superconducting regions. For effective pinning the size of the pinning site should be comparable to the diameter of the vortex which will be of the order of the coherence length, ξ . Perfectly homogeneous type II superconductors are characterized by irreversible magnetization, however any impurity or a crystal defect acts as a pinning center leading to irreversible magnetization.

Another important property of a superconductor is a discontinuous jump in the specific heat capacity at T_c . This confirms that the superconducting transition, in the absence of a magnetic field, is a *second order phase transition*. Rutgers' formula predicts the magnitude of the specific heat jump as

$$[C_s - C_n]_{T_c} = v T_c \mu_0 \left(\frac{dH_c}{dT} \right)_{T_c}^2 \quad (1.4)$$

where v is the volume per unit mass. However, in the presence of magnetic field superconducting transition is of *first order*, which is confirmed by the observation of latent heat through the transition.

1.1 THEORIES

Physics of superconductivity was a puzzle to theoretical Physicists and has called for some brilliant phenomenological and microscopic insights into condensed matter physics. The earlier disappointments in giving an appropriate theoretical explanation to superconductivity is well reflected in these lines by F.London [3] "...so Bloch concluded that the only theorem about superconductivity which can be proved is

that any theory of superconductivity is refutable, and until now experience has always verified this theorem... ", in early 1930s. Later on a few successful phenomenological and microscopic theories were proposed. Two fluid model by Gorter and Casimir[4] is a phenomenological model that addressed the thermodynamic aspect of the superconductivity. According to this model at any temperature below T_c the electrons were assumed to be of two types, namely, superconducting electrons and normal electrons, with densities n_s and n_n respectively. The total current density is then given as $J = e (n_s v_s + n_n v_n)$ where v_s and v_n are the velocities of the respective types of electrons.

Following the discovery of the Meissner effect, in 1934 F. London and H. London proposed a electrodynamic model considering the superconductor as a single macroscopic diamagnetic atom governed by the current equation,

$$\Lambda(\nabla \times J_s) = -B \quad (1.5)$$

where, Λ is the London's constant, found to be $(m/n_s e^2)$, m and e are the mass and charge of the electron. This combined with Maxwell's equation gives spatial variation of flux density within a superconductor as,

$$B(z) = B_0 e^{-z/\lambda_L} \quad (1.6)$$

λ_L is called the London's penetration depth.

In 1950, V. L. Ginzburg and L. D. Landau introduced a novel phenomenological description of superconducting phase using an *order parameter*. This parameter is expressed in complex wave field as,

$$\psi(r) = |\psi(r)| \exp(i\phi(r)) \quad (1.7)$$

where $n_s = |\psi|^2$ is the density of the superconducting carriers of mass m^* and charge e^* . The phase $\phi(r)$ represents the macroscopic coherence property of the superconducting state. The expression for free energy in terms of this order parameter is [5],

$$F_s(\psi, T, B) = \int f_s(\psi, T) \cdot dV + \frac{1}{2} \int (\mu_0^{-1} B^2 - \mu_0 H_a^2) \cdot dV \quad (1.8)$$

where f_s is the intrinsic free energy which is assumed based on the gauge invariance arguments as,

$$f_s = a(T)|\psi|^2 + \frac{1}{2} b(T)|\psi|^4 + \frac{1}{2m^*} \left| -i\hbar \nabla \psi - e^* A \psi \right|^2 \quad (1.9)$$

where $a(T)$ and $b(T)$ are temperature dependent constants, with $a(T) <(>) 0$ for $T <(>) T_c$, $b(T) > 0$ and A is the vector potential defined as $B = \text{Curl } A$ and $\text{div } A = 0$. This free energy expression with a gauge invariant gradient term is a true masterpiece contribution to phenomenological theories. Ginzburg - Landau theory yields positive interphase energy for the boundary, between normal and superconducting phases for $\lambda > \xi/\sqrt{2}$, which defines the Type I superconductor. For the Type II superconductors $\lambda < \xi/\sqrt{2}$ and Ginzburg - Landau theory yields a negative interphase energy. Thus Ginzburg - Landau theory demarcates the Type I and Type II superconductors on the basis of λ/ξ ratio.

First step towards a microscopic theory came from H. Frohlich [6] in 1950, when he pointed out that the electron - lattice can give rise to indirect interaction between two electrons. This was strongly supported by just then discovered *isotope effect* [7] (variation of T_c with isotopic mass). In 1956 L. N. Cooper [8] established from simple two electron system calculations that two electrons with attractive interaction in the presence of filled Fermi sphere always form a bound pair, later termed after him as *Cooper pair*. In 1957, J. Bardeen, L. N. Cooper and J. R. Schreiffer [9] considering many body correlations constructed a variational wave function for superconducting ground state which is separated from the band of single particle excitations by an energy gap and this model is referred to as BCS theory.

Success of BCS theory is revealed in its ability to predict even the magnitude of physical parameters such as energy gap, specific heat jump at T_c etc. The energy gap is directly related to the binding energy of the Cooper pair.

1.2 JOSEPHSON EFFECT

The most fascinating feature of superconductors is the manifestation of quantum phenomena in macroscopic measurables. In 1962, B. D. Josephson [10] calculating the tunneling current between two superconductors separated by a thin layer of insulator included the tunneling term due to Cooper pairs in addition to the ordinary single particle tunneling term. This lead to the conclusion that when a *dc* voltage *V* is applied across the junction, in addition to the *dc* current an *ac* current of frequency $2eV/h$ also flows with an amplitude proportional to the effective matrix element for pair transfer. Even in the absence of an applied *dc* voltage a *dc* supercurrent flows across the junction. These effects are called *Josephson effects*.

When two such identical superconductor-insulator-superconductor junctions are connected in parallel in the presence of a uniform magnetic field, the total Josephson current is given as,

$$I = I_0 \left| \frac{\sin(\pi\phi_B/\phi_0)}{\pi\phi_B/\phi_0} \right| \cdot \sin(\varphi - \pi\phi_T/\phi_0) \quad (1.10)$$

where ϕ_B is the flux within the junction, ϕ_T is the total flux, φ is the relative phase difference and $\phi_0 = 2\pi\hbar/e^*$. This equation for current measured across the junction reflects the interference due to the total flux ϕ_T in addition to the diffraction pattern due to the flux, ϕ_B , enclosed within a junction. This has been experimentally proven by R. C. Jaklevic *et al* [11]. Superconducting Quantum Interference Device (SQUID) is a device operating on this phenomenon of superconductors, which can detect magnetic fields as small as 10^{-15} T.

1.3 HIGH TEMPERATURE SUPERCONDUCTORS

Discovery of superconductivity in copper oxides by Bednorz and Muller[12] came as renaissance to the field in 1986. Because till then highest T_c being 23.3 K only, as found in Nb_3Ge alloy and the theories setting possible upper limit of critical temperature as 30-40 K, applications of superconductivity looked remote. Subsequent discovery of superconductivity by Chu *et al* [13] in Y-Ba-Cu-O system, brought the superconductivity above Liquid Nitrogen temperature. Now the copper oxide family of superconductors includes four major systems, namely Y-Ba-Cu-O, Bi-Sr-Ca-Cu-O, Tl-Ba-Ca-Cu-O and Hg-Ba-Ca-Cu-O superconductors. The highest T_c in the above systems are 92 K in $YBa_2Cu_3O_7$, 110 K in $Bi_2Sr_2Ca_2Cu_3O_{10}$, 125 K in $Tl_2Ba_2Ca_2Cu_3O_y$ and 133 K in $HgBa_2Ca_2Cu_3O_y$.

$YBa_2Cu_3O_7$ (YBCO) has proved to be highly adaptable chemically as it can accommodate a wide variety of cationic and anionic substitutions. Though other HTSCs have higher T_c , YBCO is of technological importance. The toxic nature of Tl and Hg mask the commercial applicability of these materials while the critical current density of the Bi-SrCa-Cu-O system falls rapidly with temperature due to thermally activated creep [14,15]. Besides, Bi is a scantily available metal. But, YBCO has higher critical current density and advantageous magnetic properties suitable for application.

1.3.1 Structure of YBCO

YBCO has an O_2 deficient triple perovskite ABO_3 structure [16] stacked along c - axis with Y or Ba taking central cation site (A) and Cu the corner sites (B). Cu has two distinct sites (Fig. 1.1). Cu(I) is coordinated to four oxygen atoms in square planar configuration, corner sharing to form a chain along b - axis. Cu(2) is square pyramidally coordinated corner shares CuO_2 sheet in ab plane.

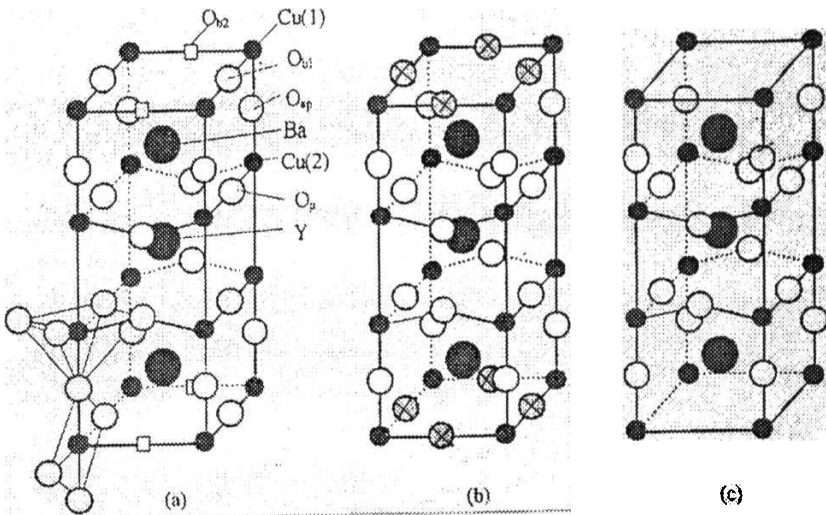


Figure 1.1 Crystal Structure of $YBa_2Cu_3O_{7-\delta}$. (a) $\delta = 0.0$ (ORTHO1), (b) $\delta = 0.5$ (ORTHO2) and (c) $\delta = 1.0$ (TETR). The squares represent vacancies, crossed circles represent half - occupied sites.

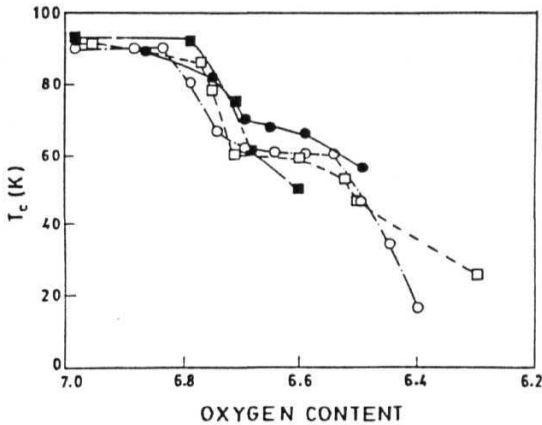


Figure 1.2 Plot of critical temperature as a function of oxygen content. (O - Beyers [17], □ - Cava [18], • - Raveau [19] and ■ - Tokumoto [20])

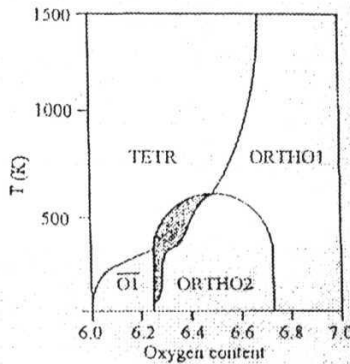


Figure 1.3 Theoretical phase diagram for $YBa_2Cu_3O_{7-x}$. ORTHO1 is the fully oxygenated $x = 0.0$ region, ORTHO2 is the $x = 0.5$ region where superstructure is observed. O1 is the orthorhombic phase when basal planes half filled. TETR is the tetragonal phase.

YBCO can take a wide O₂ stoichiometry [21] of $6 < (7 - \delta) < 7$, whilst retaining the perovskite structure, however, the symmetry changes from Orthorhombic to Tetragonal as Oxygen content falls below 6.5. The critical temperature T_c is strongly dependent on O₂ content. Figure 1.2 shows typical double plateau behavior with T_c at 90 K and 60 K for an oxygen content of 6.8 to 7.0 and 6.5 to 6.7 respectively. The double plateau is accounted for by the ordering of the oxygen atoms within the basal plane [22,23]. Fast cooling preserves the high temperature disordered state whereas slow cooling allows ordering of the vacancies leading to a superstructure along a and c axes observed by High Resolution Electron Microscopy (HREM) [24]. Figure 1.3 shows the theoretical phase diagram for the oxygen ordering in YBCO as a function of temperature and oxygen content. The fully oxygenated ORTHO1 phase becomes tetragonal phase (TETR) on oxygen depletion at high temperatures. At low temperatures ($< 600^\circ \text{C}$) when most of the CuO chains are empty O1 is observed. ORTHO2 represents the superstructure observed also at temperatures below 600 C when the oxygen content is ~ 6.5 as shown in Figure 1.1.

1.3.2 Substitutional Studies:

Substitutional studies had proven to be one of the powerful tools to gain insight into the nature of superconductivity of the HTSC. Primarily, doping an impurity element into the parent superconducting compound may enhance or deteriorate the superconducting properties of the parent compound thereby giving a clue to the origin of superconductivity in it. Secondly doping can be used to enhance the physical properties such as density, ductility etc. which may add to the technological advantage of the material. As is evident from the structure of YBCO there are three cationic and one anionic sites for possible substitutions. Substitutional studies alone have grown into such a wide topic in HTSC that it has produced many books and reviews [25,26,27]. Only major and relevant studies are touched upon here, with the emphasis on Cu site doping which is the interest of this thesis.

Y-site can be replaced to a considerable degree by most of the Lanthanides (La, Nd, Sm, Gd, Dy, Ho, Er, Tm, Yb and Lu) without quenching superconductivity. Ionic radius of Y is 1.015 Å whereas these substituents have radii varying from 1.18 Å for La

to 0.97 Å for Lu. For substituents of higher radii such as La, Nd and Sm a part of the dopant is known to go into Ba site also [28,29], which decreases T_c . Also, Antiferromagnetic ordering is a common phenomenon observed on lanthanide - doping. This confirms the coexistence of magnetic ordering and superconductivity. The lattice parameters decrease linearly with decreasing rare earth (RE) size [30,31]. From a study of Pr and Ca doped YBCO systems, tetravalent Pr is found to deplete holes per CuO_2 layer, thereby reduce T_c drastically while divalent Ca substitution for the Y site adds holes to the conduction plane leading to retrieval of critical temperature. When Y is substituted by Ca in YBCO and is fully oxygenated ($\delta = 7.0$), the critical temperature comes down, whereas T_c reaches a maximum at an oxygen content of $\delta = 6.9$ and 6.85 for 10 and 20 % Ca doping, respectively [32]. This clearly indicates the need for an optimum hole concentration in these HTSC. From the analysis of hole content in CuO_2 sheet, it is evident that not the overall copper valence but the specific hole content in the CuO_2 sheet that influences T_c directly.

Among the Ba-site doping, La dopant is an important substituent studied widely. It is reported to have a solubility of 35 %. Lattice parameters decrease with La content [33,34], as expected from the relative sizes of Ba and La. At low concentrations of La, T_c is found to increase and is considered as an evidence for overdoping [32]. The normal state resistivity increases with increasing La content and a metal to semiconductor transition is observed between 15 and 17.5 % of La.

In cuprate superconductors, the Copper Oxide planes and chains form the heart of the superconductivity and hence doping studies at the copper site have attracted much attention. Besides, antiferromagnetic ordering of Cu atoms at Cu(II) site is reported for the non-superconducting state. The intraplanar interaction is stronger than the interplanar interaction and hence the spin fluctuation in the CuO_2 plane continues even at $T > T_c$. Also doping at these two sites for Cu namely the chain and plane site affect superconductivity in an altogether different manner. The major doping elements for the copper site include the 3d transition elements such as V, Mn, Fe, Co, Ni, Zn and few other elements such as Al, Ga etc. As mentioned these substituents have different effect primarily based on the site they occupy. Elements with higher oxidation states like Al, Fe, Co etc. are known to take the Cu(I) chain site whereas the divalent elements like

Zn, Ni etc. are known to take the Cu(II) plane site. Doping at Cu(II) site had been found to be highly detrimental to superconductivity while the doping at Cu(I) site affects the charge transfer. Orthorhombic to Tetragonal (OT transition) structural change is also a regular feature observed on doping.

In conventional superconductors, superconductivity is quenched even at ppm level of magnetic impurities [35]. This has been satisfactorily explained by Abrikosov and Gorkov [36] on the basis of conduction electron –impurity spin exchange interaction leading to magnetic pair breaking. However, in YBCO non-magnetic Zn suppresses T_c more than the magnetic dopants such as Fe, Co etc. This suggests that rather than the pair breaking mechanism, disorder introduced in the CuO_2 conduction plane is effective in quenching superconductivity in these Copper Oxide superconductors.

Co substitutes at Cu(I) site upto 33 % and OT transition is observed at ~2.5 - 3.0 % of doping. Superconductivity is lost at around 15 % of doping. Solid solubility limit for Fe in $\text{YBa}_2(\text{Cu}_{1-x}\text{Fe}_x)_3\text{O}_8$ is reported to be between 10 - 27 %. An OT transition is observed at ~25 %. Fe is known to take Cu(I) site at low concentrations of doping and Cu(II) site at higher levels of doping. Superconductivity is lost at a doping level of ~10%. Reported solubility limit of Ni in $\text{YBa}_2(\text{Cu}_{1-x}\text{Ni}_x)_3\text{O}_8$ ranges from 15 % to 20 %. No OT transition is observed throughout the doping. Ni is known to occupy Cu(II) site from neutron diffraction experiments. Normal state resistivity increases with dopant concentration and the thermal coefficient of resistivity changes sign at ~8%. Negative thermopower is reported for Ni doping. Zn has a maximum solubility of 10 % in the YBCO structure with no OT transition throughout the solubility range. Rate of T_c suppression is highest in Zn doped system in the range of 10 - 13 K per atomic percent doping. The 60 K plateau shifts towards low temperature side on doping.

To summarize, the Cu(I) site dopants such as Co, Fe, Al etc. have least effect on T_c and show OT transition, whereas the Cu(II) site dopants such as Ni, Zn etc. drastically suppress the T_c and no OT transition is observed. Magnetic moment of the dopant seems to have least effect on superconductivity. On synthesizing under high pressure, Shi *et al.* [37] have observed a reversal in depression of T_c in Fe and Co doped YBCO, however, Ni dopant has not shown the same behavior. This processing induced

enhancement of superconducting behavior is rationalized in terms of specific dopant centered local structure. Besides, $(RE)Ba_2(Cu_{1-x}M_x)_3O_8$ systems with the lanthanides being substituted for RE and 3d elements for M are also widely studied [38,39,40].

Among the Cu site dopants, Mn with its higher magnetic moment is least studied due to its low solubility[41] limit. Mn is known to occupy $Cu(I)$ site from the neutron diffraction experiments[42]. Dhingra *et al.*[43] have reported a reduction in diamagnetic signal and broadening of transition beyond 1% Mn doping. Saini *et al.*[44] also have reported reduction in superconducting fraction and broadening of transition. But detailed study on the magnetic properties of the Mn doped system is lacking in the literature. Nevertheless, Mn doped system will be interesting to study, for its higher magnetic moment and $Cu(I)$ occupancy, which can provide dopant magnetic moment effect on the superconductivity of the YBCO system. Hence detailed study of transport and magnetic properties of Mn doped YBCO within the low solubility regime is taken up in the present work.

With this aim, temperature variation of dc electrical resistivity, Seebeck coefficient, ac magnetic susceptibility and DC SQUID measurements are carried out on $YBa_2(Cu_{1-x}Mn_x)_3O_7$ system and the results obtained are analyzed.

1.4 REFERENCES:

1. H.Kammerling Onnes, *Z. Phys.* (1911).
2. Michel Cyrot and Davor Pavuna, *Introduction to superconductivity and High T_c Materials*, (World Scientific Publishing Co. Pte. Ltd, 1992).
3. F. London, *Proc. Royal Society, A* **149**, 71 (1935).
4. C. J. Gorter and H. Casimir, *Physica* **1**, 306 (1934).
5. "Introduction to Superconductivity" by M. Tinkham (McGraw Hill, Inc, Singapore, 1996) p110,
6. H. Frohlich, *Phys. Rev.*, **79**, 845 (1950).
7. E. Maxwell, *Phys. Rev.*, **78**, 477 (1950).
8. L N. Cooper, *Phys. Rev.*, **104**, 1189 (1956).
9. J. Bardeen, L N. Cooper and J. R. Schreiffer, *Phys. Rev.*, **108**, 1175 (1957).
- 10 B. D. Josephson, , *Phys. Lett.*, **1**,251 (1962).
- 11 R. C. Jaklevic, J. Lambe, J. E. Mercereau and A. H. Silver, *Phys. Rev.*, **140**, **A1628** (1957).
- 12 J. G. Bednorz and K. A. Muller, *Z. Phys.*, **B 64**, 189 (1986).
- 13 C. W. Chu, P. H. Hor, R. L Meng, L. Gao, Z. J. Huang, Y. K. Wang, *Phys. Rev. Lett*, **58**,405(1987).
- 14 Y. Xu and M. Suenaga, *Phys. Rev.* **B43**, 5516 (1991).
- 15 G. F. Sun, K. W. Wong, B. R. Xu, Y. Xin and D. F. Lu, *Phys. Lett.* **A192**, 122(1994).
16. W. I. F. David, W. T. A.Harrison, J. M. F. Gunn, O. Moze, A. K. Soper, P. Day, J. D. Jorgensen, D. G. Hinks, M. A. Beno, L. Soderholm, D. W. Capone II, I. K. Schuller, C. U. Segre, K. Zhang and J. D. Grace, *Nature*, **327**, 310 (1987).
- 17 R. Beyers, B. T. Ann, G. Gorman, V. Y. Lee, S. S. P. Parkin, M. L. Ramirez, K. P. Roche, J. E. Vazquez, T. M. Gur and R. A. Huggins, *Nature*, **340**, 619 (1989).
- 18 R. J. Cava, B. Batlogg, C. H. Chen, E. A. Rietman, S. M. Zahurak and D. Werder, *Nature*, **329**,423 (1987).
- 19 B. Raveau, F. Deslandes, C. Michel and M. Hervieu, in "*High T_c Superconductors - Proc. Int. Disc. Phys.*", Ed. H. W. Webber (Plenum publishers, NY, 1988) p3.

- 20 M. Tokumoto, H. Ihara, T. Matsubara, **M. Hirabayashi, N. Terada, H. Oyanagi, K. Murata**, and Y. Kimura, *Jpn. J. Appl. Phys.*, **26**, 1565 (1987).
- 21 J. DJorgensen, B. W. Veal, W. K. Kwok, G. W. Crabtree, A. Umezawa, L. j. Nowicki and A. P. Paulikas, *Phys. Rev. B* **36**, 5731(1987).
- 22 A. Ourmazd and J. C. H. Spence, *Nature* **329**, 425 (1987).
- 23 H. F. Poulsen, N. H. Andersen, J. V. Andersen, H. Bohr and O. G. Mouritsen, **I**, **349**, 594(1991).
- 24 J. Reyes Gasga, T. Krekels, G. Van Tendeloo, J. Van Landuyt, W. H. M. Bruggink, Mverweji, S. Amelinckx, *Solid State Communication*, **71**, 269 (1989).
- 25 J.M. Tarascon and B. G. Baglay in "Chemistry of Superconducting Materials", Ed. T. A. Vanderah (Park Ridge, NJ, Nokes, 1989) p 310.
- 26 A. V. Narlikar, C. V. Narshimha Rao and S. K. Agarwal In "Studies of High Temperature Supercondutors" Ed. A. V. Narlikar (Nova Science, New York, 1990), Vol **1**, p 370.
- 27 J. M. S. Skakle, Materials Science and Engineering, **R23**, **1**, (1998).
- 28 P. Karen, H. Fjellvag, O. Braaten, A. Kjekshus and H. Bratsberg, *Acta Chem. Scan.*, **44**,994(1990).
- 29 W. H. Tang, J. Gao, *Physica C* **315**, 59 (1999).
- 30 T. Tamegai, A. Watanabe, I. Ogur and Y. Iye, *Jpn. J. Appl. Phys.*, **26**, L1304 (1987).
- 31 V. N. Narozhnyi and V. N. Kochetkov, *Phys. Rev.* **B53**, 5856 (1996).
- 32 J. L. Tallon and N. E. Flower, *Physica C* **204**, 237 (1994).
- 33 S. Mazumder, H. Rajagopal, A. Wequira, R. Venkatramani, S. P. Garg, A. K. Rajaraja, L C. Gupta and R. Vijayaraghavan, *J. Phys.*, **C 21**, 5967 (1988).
- 34 X. S. Wu and J. Gao, *Physica C* **315**, 215 (1999).
- 35 T. H. Geballe, B. T. Matthias, E. Corenzwit and G. W. Hull, *Phys. Rev. Lett.*, **8**, **313** (1962).
- 36 A. A. Abrikosov and L P. Gorkov, *Sov. Phys. JETP*, **b**, 1243 (1961).
- 37 F. Shi, R. Harris, W. J. Bresser, D. Mc Daniel and P. Boolchand, *J. Phys.: Condens. Matter*, **9**, L307 (1997).
- 38 T. A. Mary, N. R. S. Kumar and U. V. Varadaraju, *Phys. Rev.* **B48**, 16727 (1993).

- 39 P. Sumana Prabhu and U. V. Varadaraju, **Phys. Rev. B**53, **14637** (1996).
- 40 V. P. S. Awana, J. Horvat, H. K. Liu, S. X. Dou, Rajvir Singh, **A. V. Narlikar and M. P. Das**, *Physica* **C301**, 205 (1998).
- 41 R. F. Jardim and S. Gama, *Physica* **C159**, 306 (1989).
- 42 N. L. Saini, K. B. Garg, H. Rajagopal and **A. Sequeira**, *Sol. St. Comm.*, **82**, 895-899(1992).
- 43 I. Dhingra, S. C. Kashyap and B. K. Das, **J. Mater. Res.** **9**, 2771(1994).
- 44 **N. L. Saini**, P. Srivastava, B. R. Sekhar and K. B. Garg, *Int. J. Modern Phys.*, **B6**, 3575(1992).

CHAPTER - 2

SAMPLE PREPARATION AND CHARACTERIZATION

In this chapter, the method of preparation of the samples studied viz. $\text{YBa}_2(\text{Cu}_{1-x}\text{Mn}_x)_3\text{O}_{7-\delta}$ with x taking values 0.00, 0.005, 0.010, 0.015, 0.020, 0.025, 0.035 and 0.050, $\text{YBa}_2(\text{Cu}_{0.075}\text{Fe}_{0.025})_3\text{O}_{7-\delta}$, $\text{YBa}_2(\text{Cu}_{0.075}\text{Ni}_{0.025})_3\text{O}_{7-\delta}$ and $\text{YBa}_2(\text{Cu}_{0.075}\text{Zn}_{0.025})_3\text{O}_{7-\delta}$ and the details of the experimental techniques adapted in the characterization of these samples are discussed. Solid state reaction was employed for the preparation of samples which were then characterized for phase purity with the help of X-ray diffraction patterns and Scanning Electron Micrographs (SEM), the zero resistance temperature, $T_c(\text{zero})$, was determined by measuring temperature dependence of dc resistivity, $\rho(T)$, and the onset of diamagnetism was established from the temperature variation of ac susceptibility, $\chi(T)$. The samples that showed presence of impurity phases, or those that gave rise to broad transitions in $\rho(T)$ or $\chi(T)$ were resynthesized and characterized again. The best possible samples were chosen for the detailed study of physical properties.

2.1 SAMPLE PREPARATION :

In literature, ceramic superconductors are reported to have been prepared through various techniques such as solid state reaction [1,2], nitrate route [3-5], citrate route [6,7], combustion technique [8] and co-precipitation techniques [9,10]. In the chemical liquid phase methods a precursor solution is prepared by dissolving the compounds containing the metal elements in a solvent. This solution is evaporation dried as in the case of nitrate route or added with combustion compounds so that it could be fired at low temperatures as in the case of citrate method of preparation. In co-precipitation techniques the solvent used is so chosen that the metal ions co-precipitate to give the finely mixed precursor. However, complete precipitation of the components had proved to be difficult [11] and require fine control of pH and other factors during precipitation and is suitable for large scale preparation. For preparation of precursors of ~5 to 10 gms solid state route has been effective in achieving the stoichiometry wherein the loss of the starting material on mixing will be low. Hence the solid state route of preparation was preferred in the current study.

Samples for this study are prepared from starting materials of analytical grade quality Y_2O_3 (*Indian Rare Earth Chemicals*), $BaCO_3$ (*E-Merk, Germany*), CuO (*BDH, England*), Fe_2O_3 (*Sigma Chemicals, USA*), Ni_2O_3 (*Alfa products, USA*) and ZnO (*Sigma Chemicals, USA*). Sample preparation involved three steps namely (i) preparation of the precursor, (ii) calcination and pelletization (iii) heat treatment and oxygen annealing. The precursor was prepared by mixing the stoichiometric ratios of the required Y_2O_3 , $BaCO_3$, CuO and Fe_2O_3 or Ni_2O_3 or ZnO in an agate mortar for about half an hour. This mixture was then presintered at $900^\circ C$ for ~12 hrs. Mixing and presintering at $900^\circ C$ was repeated thrice, for homogeneity. Thus prepared presintered powders were pressed into square pellets of size 1 cm x 1 cm x 0.5 cm under a uniaxial pressure of -6 Tons. These pellets were sintered at $930^\circ C$ for 36 hrs. and furnace cooled. The sintered pellets were O_2 annealed at $450^\circ C$ for ~60 hrs.

2.2 CHARACTERIZATION TECHNIQUES :

Samples for detailed study are selected after an examination through the following characterization techniques:

2.2.1 X - Ray Diffraction :

The samples were first characterized for structural purity using powder X-ray diffraction (XRD) method. The XRD patterns were recorded on the square pellets using *Siemens* X-Ray Diffractometer provided with Cu - K α radiation of wavelength $\lambda = 1.5418$ Å. Characteristic diffraction lines corresponding to various (hkl) values were recorded for 2θ values ranging from 10° to 60° . The lattice parameters a , b and c were obtained from the 2θ values by least square refinement of Bragg equation.

2.2.2 Microstructure :

Since the sensitivity of the XRD is limited to 5 %, to ensure the phase purity the samples were characterized by Optical and Scanning Electron Micrograph for the absence of secondary phase segregation. *Leitz* made reflected light optical microscope (at DMRL, Hyderabad) with facility for polarized light was used in the magnification range of 50 to 100, to look into the grain distribution and segregation if any. Also *JEOL JSM 840* - scanning electron microscope (at DMRL, Hyderabad) was used to measure the grain size at higher magnifications. The average grain size was taken through the mean linear intercept method. In this method the number of grains (N) falling on a line drawn across the micrograph is counted and the width of each grain (L) falling on the line is taken as the distance between the grain boundary intercepts with the line. And the average grain size d is given as

$$d = \frac{\sum L}{N}$$

Typically the grain sizes varied from $1 \mu m$ to $12 \mu m$.

2.2.3 dc Resistivity :

To measure the dc resistivity, parallelepiped samples of dimensions $\sim 0.5 \times 1.0 \times 10.0$ mm were cut from the square pellet. Standard four probe technique was adapted to measure the resistivity (Fig. 2.1) whereby the contact resistance was eliminated. Four contact leads were connected using silver paint and *SWG #38* copper wire along the length of the parallelepiped sample. The outer two leads were used to pass current and the inner leads were used to measure the voltage drop. A current, I was driven across the outer leads of the sample using a *Keithley 224* programmable constant current source and the voltage (V^*) developed across the

sample was measured across the two inner leads using a *Keithley 181* nano Voltmeter. The current direction was reversed (to nullify the thermo emf induced) and the developed voltage was measured as V . The resistance across the sample was then calculated as $R = (V^+ - V^-)/2I$. Absolute resistivity was calculated as

$$\rho = \frac{Rbt}{d}$$

where, b and t are the breadth and the thickness of the parallelepiped sample, d is the distance between the voltage leads and R is the measured resistance of the sample. The accuracy of the measured resistivity is $1 \mu\Omega\text{cm}$.

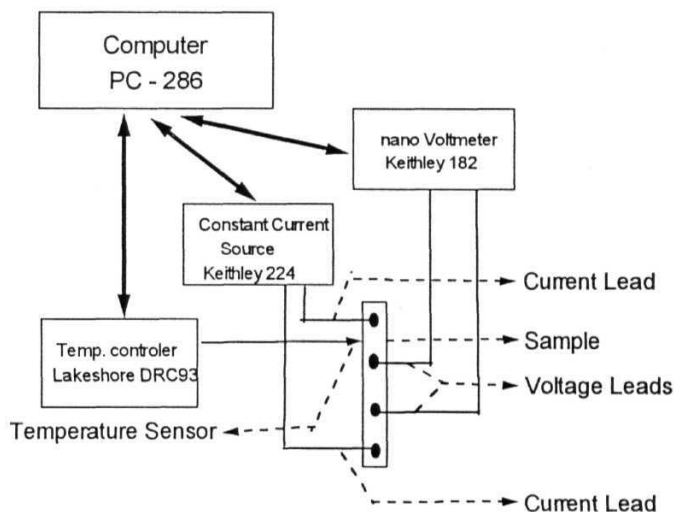


Figure 2.1 Schematic diagram of the experimental setup used for the resistivity measurements.

Figure 2.2 shows the APD make helium gas exchange cryostat, with *Cu-B_e* sample tube, cooled by the closed cycle helium refrigeration that was used for the measurements of the temperature variation of resistivity and susceptibility. A standard sample holder made of glass cloth/ epoxy tube of inner diameter 0.95 cm was used to carry the sample and Si diode temperature sensor into the cryostat. The electrical connections to the sample for resistivity measurements and the

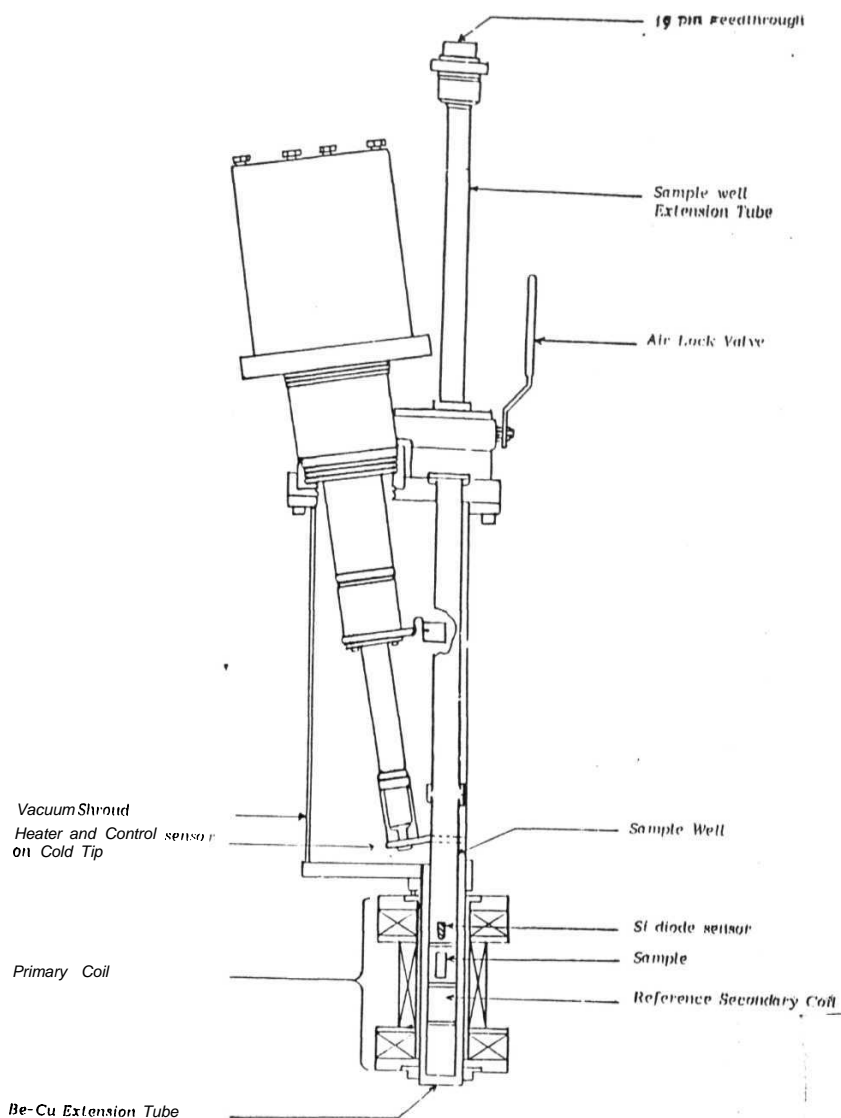


Figure 2.2 Schematic diagram of the Helium **exchange gas** filled cryostat used for the precisely controlled low temperature measurements of resistivity and susceptibility.

connections to the sensor were made through **the** 19-pin connector **at the end of** the sample holder. The cold tip of the expander valve of the closed cycle refrigerator cooled the cryostat. This expander valve was provided with another Si diode control sensor and a heater which were monitored and controlled by a *Lakeshore - DRC93* temperature controller. The temperature of the cryostat was thus controlled through the temperature controller. The accuracy of the temperature measurement was better than 50 mK. The constant current source and digital nano voltmeter **and the** above temperature controller were connected to a computer through *IEEE 488 (GPIB)* interface. A computer programme written in BASIC language was used to control the various equipment and for the data acquisition during the entire temperature variation of resistivity measurement.

2.2.4 ac Susceptibility :

Temperature variation of ac susceptibility at a constant ac field amplitude was carried out using a mutual inductance bridge assembly made of two secondary coils connected in series opposition and a coaxially seated primary on the top of these two secondaries. Since the secondaries are connected in **series** opposition, the net induced voltage in the secondaries is zero. When a sample is kept in one of the secondaries the induced voltage in the secondaries is proportional to the susceptibility of the sample as follows:

$$\left[\begin{array}{l} \text{Net Voltage across} \\ \text{the secondary (V)} \end{array} \right] = \left(\begin{array}{l} \text{Voltage across the sample} \\ \text{secondary (Vs)} \end{array} \right) - \left(\begin{array}{l} \text{Voltage across the reference} \\ \text{secondary (Vr)} \end{array} \right)$$

$$V = C \frac{d(\phi_s - \phi_r)}{dt} = CA \frac{d(B_s - B_r)}{dt}$$

The flux density in the sample secondary is given as $B_s = \mu_o(H + M)$, where M is the magnetization of the sample. The flux density inside the reference secondary coil is $B_r = \mu_o H$. Hence the net Voltage across the secondaries is given by,

$$dT$$

where C and C' are constants. Thus the voltage across the **secondaries**, V can be calibrated to obtain volume susceptibility directly.

The schematic diagram for the susceptibility measurement is given in Figure 2.3. As shown in Figure 2.2 the primary coil was seated around the *Be-Cu* cryostat. The primary can generate a maximum field of 325 Oe at 1 Amp applied current. The primary coil was energized by a *WaveTek 178* waveform synthesizer of 50 Ω output impedance. Sine wave of magnitude from 0.02 V_{rms} to 3.5 V_{rms} was used at a frequency of 33 Hz. The current through the primary was calculated from the voltage developed across a 10 Ω resistor connected in series with the primary coil. This voltage ($V_{10\Omega}$) was measured using a *Keithley 196* multimeter, which was calibrated to give the field strength as:

$$H_a = \frac{4\pi N V_{10\Omega}}{100} \text{ Gauss}$$

where N and l are the number of turns and length of the primary respectively.

The secondaries were fixed inside the cryostat around the sample holder. Each secondary was of 3250 turns of SWG #38 gauge standard insulated copper wire. The sample was placed in the sample secondary, which was the upper secondary in the Figure 2.2. The output from the secondaries was connected to a dual phase - phase sensitive detector (EG&G PAR 5210 - Lock in amplifier). Conventionally, the voltage drop across a resistor in series with primary is fed to the reference channel of the lock-in amplifier. But, the voltage drop across the resistor was too low at low excitation fields (H_{ac}) to achieve phase-locking. Hence, a synchronous TTL reference signal (a constant 5 V) from the Wavetek oscillator was fed to the phase sensitive detector for phase reference. However, since the TTL reference fed an voltage component across the primary whereas the field will be inphase with the current, a correction for the phase lag introduced by the impedance of the primary was made in the settings of lock-in amplifier to have the reference in phase with the current in the primary. This was done following the criterion that at small H_{ac} , loss (χ'') component is zero at $T \ll T_c$, as well as $T \gg T_c$. From the voltage measured across the secondaries, the absolute values of volume susceptibility were calculated numerically following the equation given by Murphy et al [11] and Couach and Khoder [12]. If V_R and V , are the 90° out of phase signal and the inphase signal measured across the secondary in the dual phase - phase sensitive detector, then the real (χ') and imaginary (χ'') parts of susceptibility according to Murphy et al[11] are,

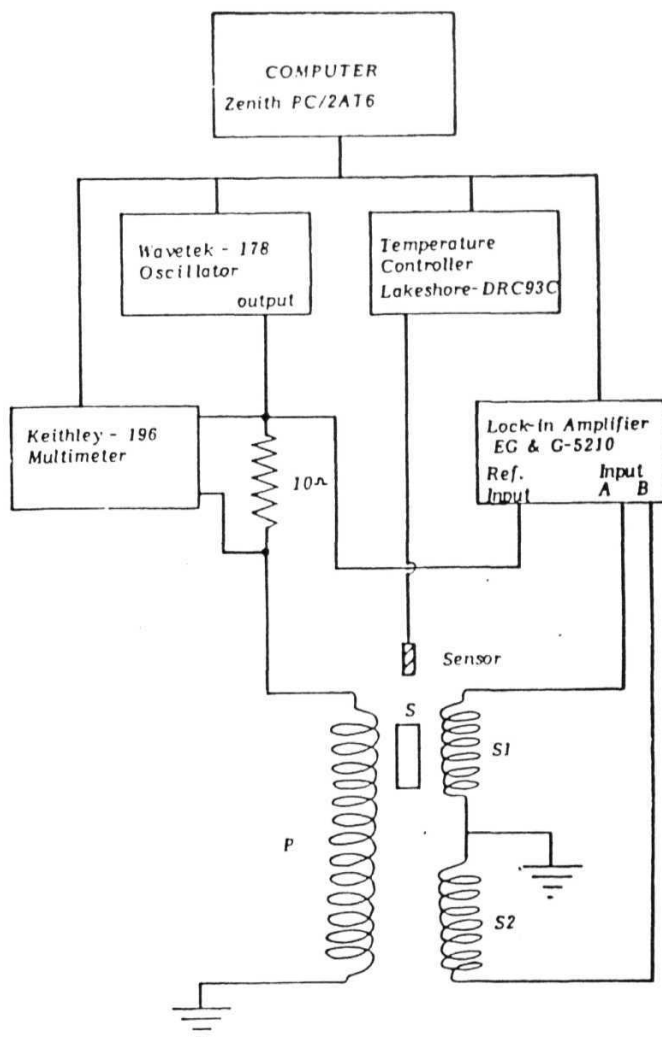


Figure 2.3 Schematic diagram of the experimental setup used for the susceptibility measurements.

$$\chi' = \frac{\chi_R - D(\chi_R^2 + \chi_I^2)}{(1 - \chi_R D)^2 + D^2 \chi_I^2}$$

$$\chi'' = \frac{\chi_I}{(1 - \chi_R D)^2 + D^2 \chi_I^2}$$

where,

$$\chi_R = \frac{V_R}{\alpha \omega A N_s \mu_0 H_m (1 - D)}$$

and

$$\chi_I = \frac{V_I}{\alpha \omega A N_s \mu_0 H_m (1 - D)}$$

with $\omega = 2\pi f$ where f is the operational frequency, a is the filling factor [12], A is the area of cross section of the sample, N_s is the effective number of turns of the secondary over the sample, H_m is the field amplitude and D is the demagnetizing factor given as [13]

$$D = \left(\frac{8}{2\pi} \right) \cot^{-1} \left(\frac{\sqrt{x^2 + y^2 + z^2} \cdot z}{xy} \right)$$

where x , y and z are the thickness, breadth and length of the sample, with field applied along z , parallel to the length of the sample.

Temperature variation of ac susceptibility was measured by sweeping the temperature from 10 K to 110 K at a sweeping rate of 10 - 15 K / hr at temperatures away from the transition and at 3 - 5 K/hr through transition. The silicon diode sensor placed near the sample was used for temperature measurement. The control and data acquisition was carried out through the computer.

2.3 SAMPLE CHARACTERIZATION :

2.3.1 Samples Studied :

The samples selected for detailed **study, after preliminary characterizations** are listed below and the results of the **characterization of the screened samples** are presented subsequently.

The samples studied in this thesis are :

$\text{YBa}_2\text{Cu}_3\text{O}_{7-\delta}$	-Pure
$\text{YBa}_2(\text{Cu}_{0.990} \text{Mn}_{0.010})_3\text{O}_{7-\delta}$	- 1.0 % Mn doped
$\text{YBa}_2(\text{Cu}_{0.985} \text{Mn}_{0.015})_3\text{O}_{7-\delta}$	- 1.5 % Mn doped
$\text{YBa}_2(\text{Cu}_{0.980} \text{Mn}_{0.020})_3\text{O}_{7-\delta}$	- 2.0 % Mn doped
$\text{YBa}_2(\text{Cu}_{0.975} \text{Mn}_{0.025})_3\text{O}_{7-\delta}$	- 2.5 % Mn doped
$\text{YBa}_2(\text{Cu}_{0.965} \text{Mn}_{0.035})_3\text{O}_{7-\delta}$	- 3.5 % Mn doped
$\text{YBa}_2(\text{Cu}_{0.950} \text{Mn}_{0.050})_3\text{O}_{7-\delta}$	- 5.0 % Mn doped
$\text{YBa}_2(\text{Cu}_{0.975} \text{Fe}_{0.025})_3\text{O}_{7-\delta}$	- 2.5 % Fe doped
$\text{YBa}_2(\text{Cu}_{0.975} \text{Ni}_{0.025})_3\text{O}_{7-\delta}$	- 2.5 % Ni doped
$\text{YBa}_2(\text{Cu}_{0.975} \text{Zn}_{0.025})_3\text{O}_{7-\delta}$	- 2.5 % Zn doped

Though the doping of $\text{YBa}_2\text{Cu}_3\text{O}_{7-\delta}$ with Mn **at Cu site was the objective** interest of the thesis, samples with 2.5 % Fe, Ni and Zn dopants **were also** prepared to study the marked similarities and contrast of **the** Mn doping **with the** other 3d elemental doping, especially in the context **of its** doping **sites namely Cu(I)** and Cu(II).

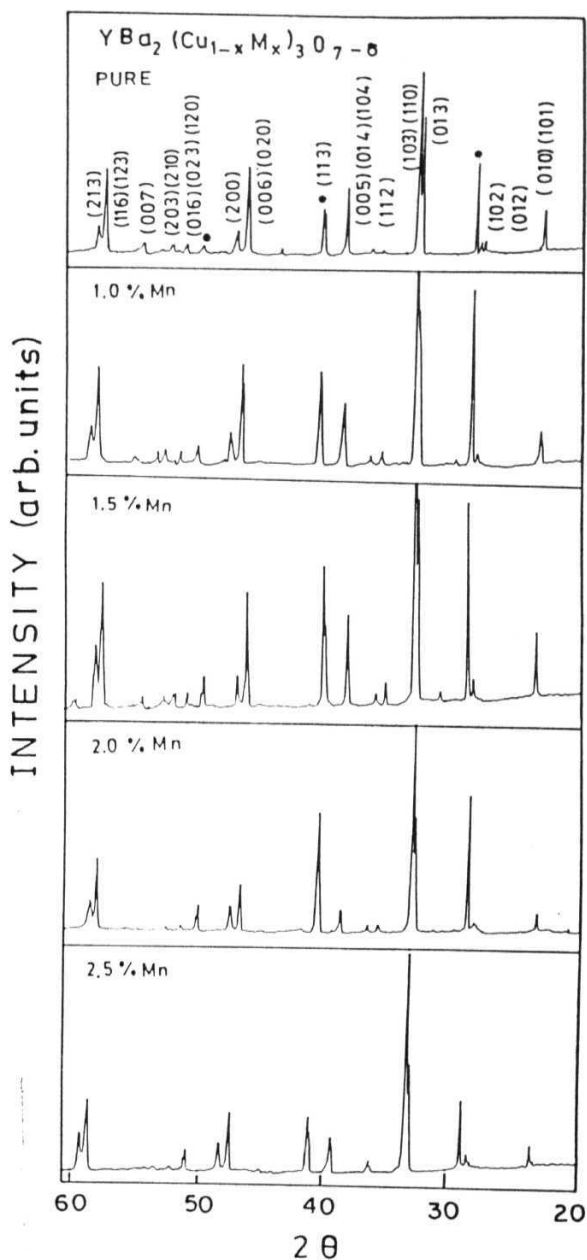


Figure 2.4a The XRD patterns for the YBa₂(Cu_{1-x}Mn_x)₃O_{7-δ} samples with $x = 0.0, 0.01, 0.015, 0.02$ and 0.025 • - *KCl lines*

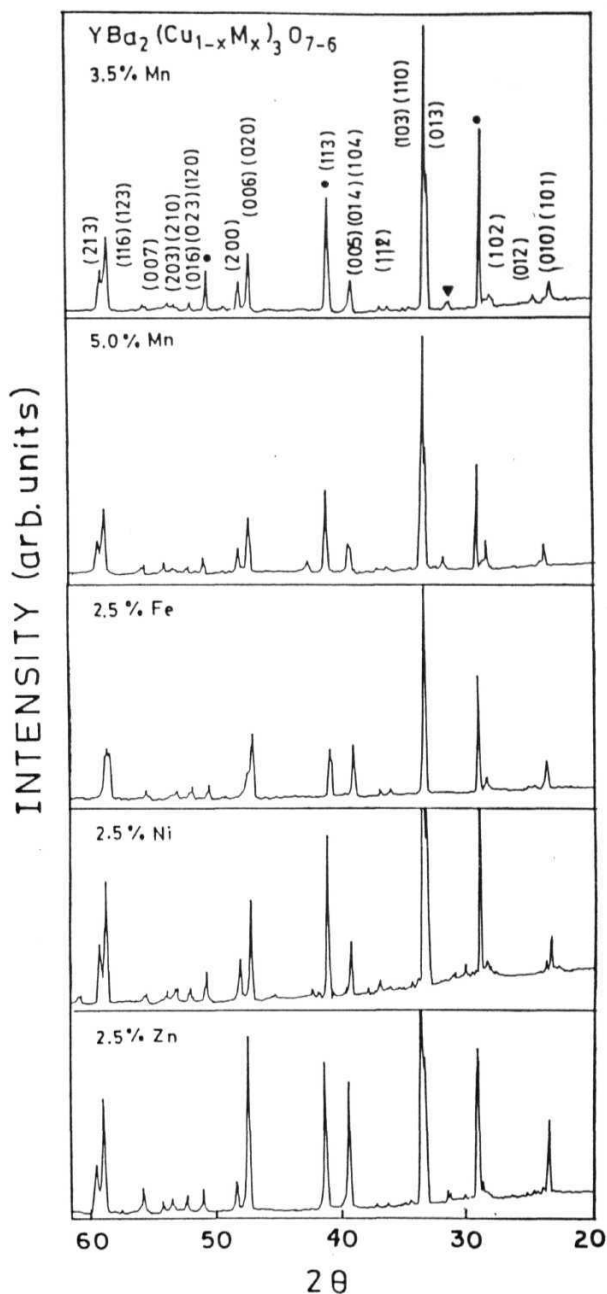


Figure 2.4b The XRD pattern of the YBa₂(Cu_{1-x}Mn_x)₃O₇₋₆ samples with x taking values 0.035 and 0.050, YBa₂(Cu_{0.075}Fe_{0.025})₃O₇₋₆, YBa₂(Cu_{0.075}Ni_{0.025})₃O₇₋₆ and YBa₂(Cu_{0.075}Zn_{0.025})₃O₇₋₆ samples.
 • KCl lines ▼ - Ba₂Mn₂O₈ lines

XRD and SEM :

Figures 2.4a and 2.4b show XRD pattern of the $\text{YBa}_2(\text{Cu}_{1-x}\text{Mn}_x)_3\text{O}_{7-\delta}$ samples with x taking values 0.00, 0.005, 0.010, 0.015, 0.020, 0.025, 0.035 and 0.050, $\text{YBa}_2(\text{Cu}_{0.075}\text{Fe}_{0.025})_3\text{O}_{7-\delta}$, $\text{YBa}_2(\text{Cu}_{0.075}\text{Ni}_{0.025})_3\text{O}_{7-\delta}$ and $\text{YBa}_2(\text{Cu}_{0.075}\text{Zn}_{0.025})_3\text{O}_{7-\delta}$ samples, selected for detailed study. The XRD pattern was indexed with (hkl) values by comparing with a standard XRD pattern of $\text{YBa}_2\text{Cu}_3\text{O}_{7-\delta}$ [14]. All the observed peaks could be indexed to the orthorhombic $\text{YBa}_2\text{Cu}_3\text{O}_{7-\delta}$ structure except in the case of 3.5 and 5.0 % Mn doped samples where signature of $\text{Ba}_3\text{Mn}_2\text{O}_8$ is seen at $\sim 28^\circ$ and $31^\circ - 2\theta$ values. For the lattice parameter calculations, the sample was powdered and added with a small amount of KCl for reference and XRD patterns were recorded. With reference to the known 20 peaks of the standard KCl , other 20 peak positions were precisely measured and indexed as earlier. From the indexed 20 values the lattice parameters were calculated by least square refinement. The lattice parameters obtained are tabulated in Table 2.1.

Table 2.1 The lattice parameters, a , b and c , the grain size calculated from SEM and the relative density of the samples studied.

Sample	a (Å)	b (Å)	c (Å)	Grain size (μm)	$D_{\text{obs}}/D_{\text{theo}}$ $\times 100$
Pure	3.82	3.88	11.67	7.75	74.0
1.0 % Mn	3.82	3.87	11.67	8.25	64.2
1.5 % Mn	3.82	3.88	11.67	9.42	75.2
2.0 % Mn	3.81	3.88	11.67	9.65	75.0
2.5 % Mn	3.81	3.83	11.66	15.18	68.8
3.5 % Mn	3.82	3.88	11.66	11.20	69.8
5.0 % Mn	3.81	3.87	11.67	11.33	63.4
2.5 % Fe	3.83	3.87	11.65	13.28	76.9
2.5 % Ni	3.82	3.88	11.66	9.45	79.3
2.5 % Zn	3.82	3.89	11.67	9.50	62.3

Figures 2.5a and 2.5b show the typical micrographs for the pure, 2.5% Mn doped 2.5 % Fe doped and 2.5 % Ni doped samples, showing an absence of secondary phase segregation. The grain sizes estimated for these samples were 7.75, 15.18, 13.28, and 9.45 μm respectively. The grain size estimated for the other

given in Table 2.1. It can be seen from the table that the grain size increases gradually from $7.74\ \mu\text{m}$ for the pure YBCO sample to $15.15\ \mu\text{m}$ for the 2.5 % Mn doped sample, beyond which it remains at around $11.2\ \mu\text{m}$.

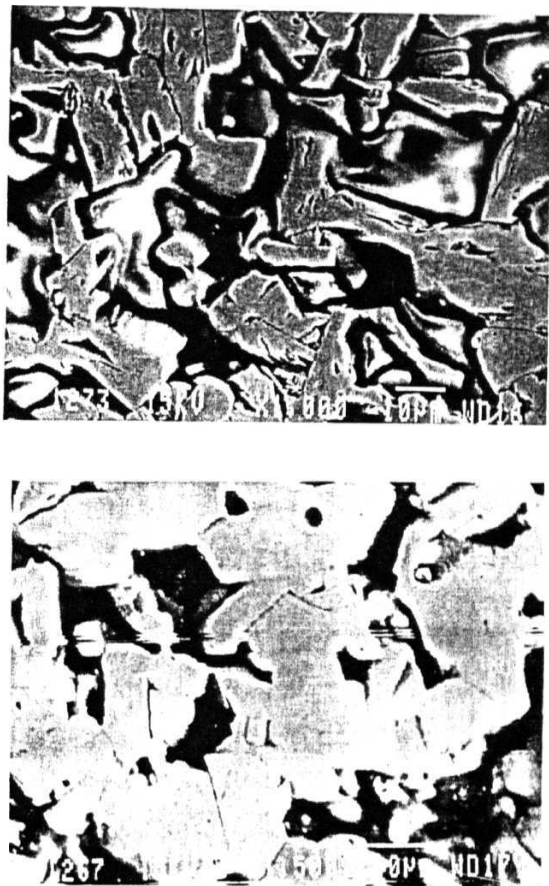


Figure 2.5 Scanning Electron Micrograph of the $\text{YBa}_2(\text{Cu}_{1-x}\text{Mn}_x)_3\text{O}_{7-\delta}$ samples with x taking values (a) 0.00 and (b) 0.025 samples.

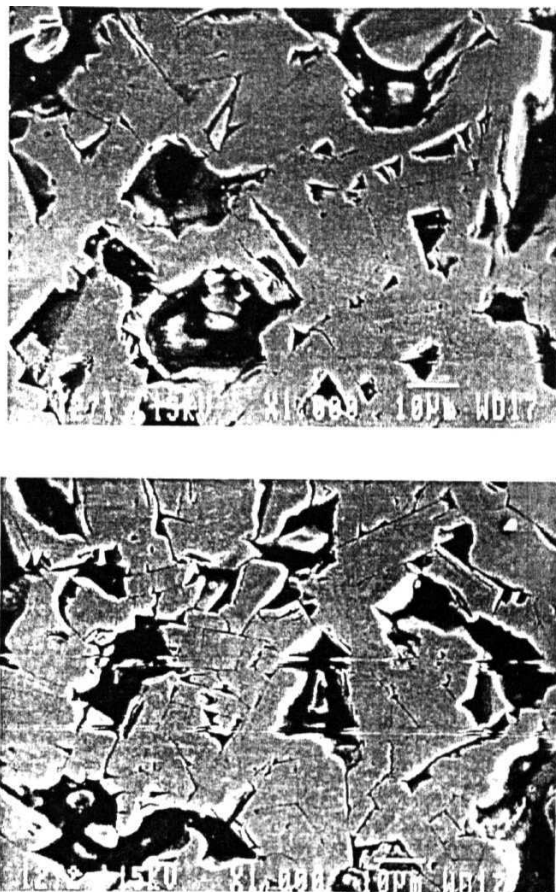


Figure 2.5 Scanning Electron Micrograph of the (c) $\text{YBa}_2(\text{Cu}_{0.075}\text{Fe}_{0.025})_3\text{O}_{7.8}$, and (d) $\text{YBa}_2(\text{Cu}_{0.075}\text{Ni}_{0.025})_3\text{O}_{7.8}$ samples

The density (D_{obs}) of the sample was calculated as mass per unit volume. The relative density which is the ratio of the observed density to the theoretical one (D_{obs}/D_{theo}) varied between 62.3 % to 79.3 % as tabulated in Table 2.1. This data shows that the samples with 1.0 % and 5.0 % Mn dopant are comparatively less densely packed (or more porous) than the other Mn doped samples, while 2.5 % Zn doped has the least relative density of all.

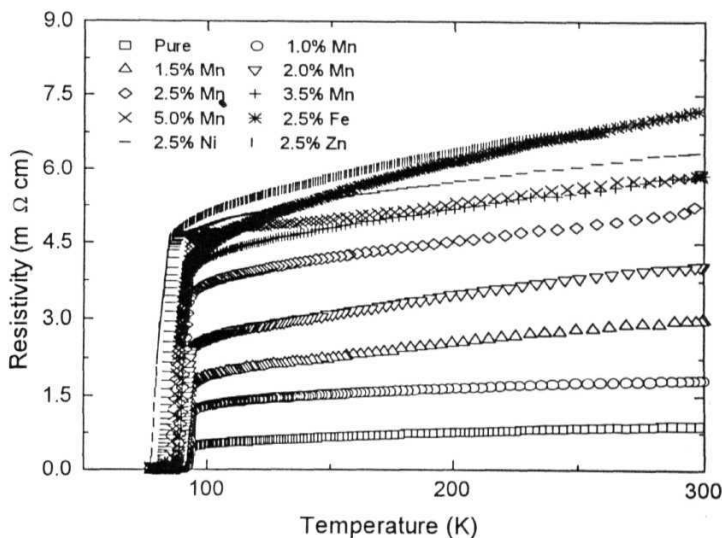


Figure 2.6 Plot of temperature variation of resistivity for the $YBa_2(Cu_{1-x}Mn_x)_3O_{7-\delta}$ samples with x taking values 0.00, 0.005, 0.010, 0.015, 0.020, 0.025, 0.035 and 0.050, $YBa_2(Cu_{0.075}Fe_{0.025})_3O_{7-\delta}$, $YBa_2(Cu_{0.075}Ni_{0.025})_3O_{7-\delta}$ and $YBa_2(Cu_{0.075}Zn_{0.025})_3O_{7-\delta}$ samples.

2.3.2 Temperature Dependence of dc Electrical Resistivity :

On the structurally characterized above samples, temperature variation of dc resistivity was carried out. Figure 2.6 shows the plot of temperature variation of resistivity for the $YBa_2(Cu_{1-x}Mn_x)_3O_{7-\delta}$ samples with x taking values 0.00, 0.005,

0.010, 0.015, 0.020, 0.025, 0.035 and 0.050, $\text{YBa}_2(\text{Cu}_{0.075}\text{Fe}_{0.025})_3\text{O}_{7-\delta}$, $\text{YBa}_2(\text{Cu}_{0.075}\text{Ni}_{0.025})_3\text{O}_{7-\delta}$ and $\text{YBa}_2(\text{Cu}_{0.075}\text{Zn}_{0.025})_3\text{O}_{7-\delta}$ samples. The resistivity measurements were carried out on parallelepiped samples of dimension $\sim 0.5 \times 1.0 \times 10.0$ mm, cut after annealing the square pellets in Oxygen. A constant dc current of 10 mA was driven across the sample. The normal state resistivity showed metallic behavior followed by a sharp transition into superconducting state showing zero resistivity to the best of the measurable sensitivity ($< 1 \mu\Omega \text{ cm}$), below the transition temperature. The room temperature resistivity was as low as 1 to 10 $\text{m}\Omega \text{ cm}$. The transition width (ΔT_c) was typically of the order of 3.5 K, while the 2.5 % Zn doped sample showed 5.92 K width and 5.0 % Mn doped sample exhibited a width of $\Delta T_c = 7.01$ K. Table 2.2 gives the values of resistive transition temperature, taken as an average of $T_{c(\text{onset})}$ and T_{zero} and the transition width (ΔT_c).

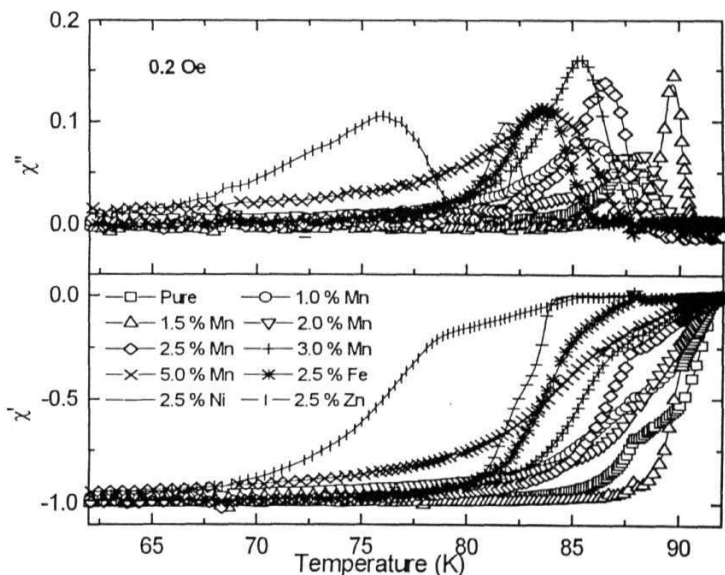


Figure 2.7 Plot of temperature variation of real and imaginary parts of ac susceptibility for the $\text{YBa}_2(\text{Cu}_{1-x}\text{Mn}_x)_3\text{O}_{7-\delta}$ samples with x taking values 0.00, 0.005, 0.010, 0.015, 0.020, 0.025, 0.035 and 0.050, $\text{YBa}_2(\text{Cu}_{0.075}\text{Fe}_{0.025})_3\text{O}_{7-\delta}$, $\text{YBa}_2(\text{Cu}_{0.075}\text{Ni}_{0.025})_3\text{O}_{7-\delta}$ and $\text{YBa}_2(\text{Cu}_{0.075}\text{Zn}_{0.025})_3\text{O}_{7-\delta}$ samples, at an energizing field of 0.2 Oe.

Table 2.2 Resistivity transition temperature, transition width and magnetic transition temperature at 0.2 Oe field.

Sample	Resistivity T_c (Average) K	Resistivity Transition Width (ΔT_c) K	Magnetic T_c K
Pure	91.60	1.67	91.26
1.0 %Mn	91.10	3.64	91.47
1.5 % Mn	91.60	2.19	91.24
2.0 % Mn	91.10	3.32	91.01
2.5 % Mn	89.65	3.78	90.75
3.5 % Mn	89.90	3.47	90.53
5.0 % Mn	89.30	7.01	89.37
2.5 % Fe	89.40	3.35	86.37
2.5 % Ni	83.68	3.47	83.55
2.5 % Zn	80.79	5.92	77.69

2.3.3 Temperature variation of ac Susceptibility :

The temperature variation of ac susceptibility was carried out on the above samples, for which an energizing field of amplitude 0.2 Oe was used **and the** temperature was swept from 10 K to 110 K in zero field cooled condition. Figure 2.7 shows the variation of real (χ') and imaginary (χ'') parts of ac susceptibility **with** temperature for these samples. Typically, the χ' showed the characteristic transition of volume susceptibility going from zero at 110 K to -1 at temperatures below **the** transition temperature. All samples showed perfect shielding (*i.e.* (χ') = -1) at **low** temperatures. χ'' showed a strong peak of width between 2 to 5 K for different samples. Table 2.2 also gives the magnetic transition temperature measured as **the** peak position of dx'/dT vs. T curve.

On these characterized samples, detailed study **of transport and magnetic** properties were carried out.

2.4 REFERENCES :

1. R. J. Cava, R. B. Van Dover, B. Batlogg and E. A. Rietman, *Phys. Rev. Lett*, **58**, 408(1987).
2. C. W. Chu, P. H. Hor, R. L. Meng, L. Gao, Z. J. Huang, Y. K. Wang, *Phys. Rev. Lett*, **58**, 405(1987).
3. A. M. Stacy, J. V. Badding, M. J. Geselbracht, W. K. Ham, C. F. Millikan and H. C. Zur Loye, *J. Am. Chem. Soc.*, **109**, 2528(1987).
4. S. Davidson, K. Smith, R. Kershaw, K. Dwight and A. Wold, *Mat Res. Bull.*, **22**, 1659(1987).
5. M. L. Kalpan and J. J. Huaser, *Mater. Res. Bull.*, **23**, 287(1987).
6. F. R. Sale and F. Mahlooji, *Ceramic International*, **14**, 229 (1988).
7. R. S. Liu, W. N. Wang, C. T. Chang and P. T. Wu, *Jpn. J. Appl. Phys.*, **28**, L2155(1989).
8. R. Gopalan, Y. S. N. Murthy, T. Rajasekharan, S. Ravi and V. Seshu Bai, *Mat Lett.*, **8**, 441(1987).
9. J. D. Jorgensen, H. B. Schuttler, D. G. Hinks, D. W. Capone II, K. Zhang, M. B. Brodsky and D. J. Scalapino, *Phys. Rev. Lett.*, **58**, 1024(1987)
10. D. W. Capone, D. G. Hinks, J. D. Jorgensen, K. Zhang, *Appl. Phys Lett*, **58**, 543(1987).
11. S. D. Murphy, K. Renouard, R. Crittenden and S. M. Bhagat, *Solid State Communication*, **69**, 367 (1989).
12. M. Couach and A. F. Khoder in "Magnetic Susceptibility of Superconductors and Other Spin Systems", Ed. R. A. Hein, T. L. Francavilla and D. H. Liebenberg (Plenum Publishers, New York, 1991). p25.
13. S. M. Bhagat, S. Haraldson and O. Beckman, *J. Phys. Chem. Solids*, **38**, 593 (1977).
14. A. M. T. Bell, *Supercond. Sci. Tech.*, **3**, 55 (1990).

CHAPTER - 3

TRANSPORT PROPERTIES

Understanding the transport phenomena of materials is **the first step** in understanding the role of charge carriers, phonons and the scattering processes involving them. Measurements of thermal and electrical properties of a material, such as resistivity, Hall effect, thermal conductivity, Seebeck coefficient, *etc.* reflect the transport behavior of the material. Over the decade, since the discovery of high T_c superconductors, study of transport properties has been a rich source of information on Fermi surface and phonon spectrum, complimented by theory [1,2,3,4,5,6,7] and experiments [8,9,10,11,12] alike. As the temperature is swept down through the superconducting transition, a phase transition marked by the onset of charge carrier condensation occurs which is responsible for the sharp changes in the electromagnetic and kinetic properties of the superconductor. It has been recognized that even the normal metallic state of the HTSC exhibits many unusual transport properties. However, in the case of HTSC probing the normal state properties are limited to temperatures above their high transition temperatures, except in the measurement of thermal conductivity.

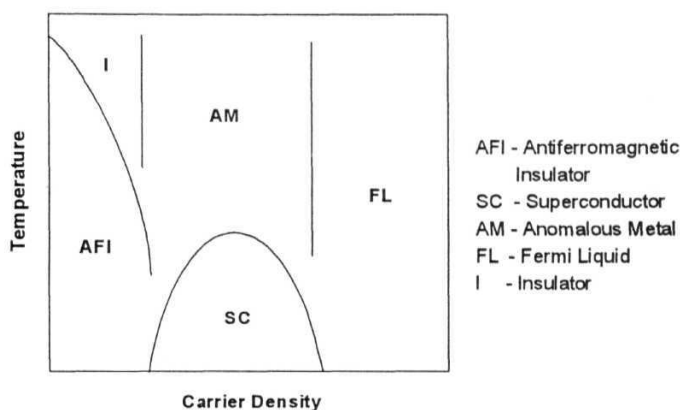


Figure 3.1 Model generic phase diagram of high Tc Cuprate system

In HTSC, CuO_2 planar network is believed to be the principal site of electronic activity. The left end of the generic phase diagram of the HTSC (Fig.3.1) materials represent the insulating parent material with CuO_2 having copper ions in divalent state with $\text{Cu}(3d^9)$ configuration. This corresponds to a half filled $d_{x^2-y^2}$ band, which is characteristic of metallic behavior. Hence, a strong electron - electron correlation is supposed to be the cause for the insulating property of the parent material [13]. The insulating parent material shows antiferromagnetic ordering described by two dimensional $S = \frac{1}{2}$ Heisenberg model [14]. As holes are introduced into the CuO_2 plane of the insulating parent material, either by cationic substitution or by oxygen intercalation, it undergoes a insulator-to-metal transition where superconductivity also occurs [15,16]. There appears to be no normal metallic ground state between the insulating and superconducting ground states in Figure 3.1. So is the case when superconductivity is quenched by substitution of Cu with Ni, Co, Zn, etc. or by substitution of Pr for Y in $\text{YBa}_2\text{Cu}_3\text{O}_{7-x}$ [17]. Hence it could be inferred that addition of few extra holes into the CuO_2 plane destroys the long range antiferromagnetic order [15]. This makes the Cu site doping studies valuable.

In $\text{YBa}_2\text{Cu}_3\text{O}_{7-x}$ system, the effect of dopant induced variation of carrier density on superconducting properties is widely studied [18,19,20]. In the present work, temperature

variation of resistivity and Seebeck coefficient are studied to understand **the transport phenomena** in 0, 1.0, 1.5, 2.0, 2.5, 3.5 and 5.0 % Mn doped $\text{YBa}_2\text{Cu}_3\text{O}_{7-x}$ system and the results are compared with that of 2.5 % Fe doped material in which **Fe** occupies **Cu(I)** site like Mn does.

3.1 RESISTIVITY:

Resistivity measurement has become a routine laboratory test to establish superconductivity. Nevertheless, a detailed study on it can **expose different transport** parameters. A low magnitude of room temperature resistivity, $\rho(300)$, is a rough indication of good sample quality [17].

In the cuprate HTSCs with increasing carrier density at CuO_2 plane, **the** temperature dependence of resistivity exhibits a variation from semiconductor like behavior **to metallic** behavior. At low level of carrier doping the temperature variation of resistivity is semiconductor like and is well described by the Mott's formula for variable **range hopping** conduction [13], given as

$$\rho(T) \propto \exp \left(- \left(\frac{T_0}{T} \right)^{1/D+1} \right)$$

where D is the dimensionality of the system.

At an optimal doping level of holes, when superconductivity **sets** in, a **linear** dependence of resistivity on T is observed. This is in contrast **with the T^2 -dependence** predicted for canonical Fermi fluids when no other scattering is present. However, invoking scattering by phonons or other Bosonic excitations give a linear dependence of resistivity on T, for temperatures above the characteristic energy scale of the Bosons. **Bloch-Grüneisen** formula describes the variation of such phonon-limited resistivity **with** temperature as

$$\rho(T) \propto \left(\frac{T}{\Theta} \right)^5 \int_0^{T/\Theta} \frac{x^5 dx}{(e^x - 1)(1 - e^{-x})}$$

Where Θ is an effective transport Debye temperature. In $\text{YBa}_2\text{Cu}_4\text{O}_8$ system, Martin *et al.* [21] explained the normal state resistivity with Bloch-Grüneisen formula and have obtained physically reasonable parameters.

Numerous reports and reviews on normal state resistivity of the HTSC can be found in the literature. Friedman *et al.*[22] have measured resistivity on $\text{YBa}_2\text{Cu}_3\text{O}_{7-\delta}$ single crystal and reported $\rho(300)$ along a , b and c axes as 172, 72 and 5422 $\mu\Omega\text{cm}$ respectively. Anderson and Zou[23] have reported $1/T$ dependence of c - axis resistivity of the YBCO crystals. Nianhua *et al.* [24] have studied Fe, Ni and Zn doped $\text{YBa}_2\text{Cu}_3\text{O}_{7-\delta}$ compound and demonstrated that the suppression of superconductivity by oxygen depletion and substitution of Cu by 3d elements are very different.

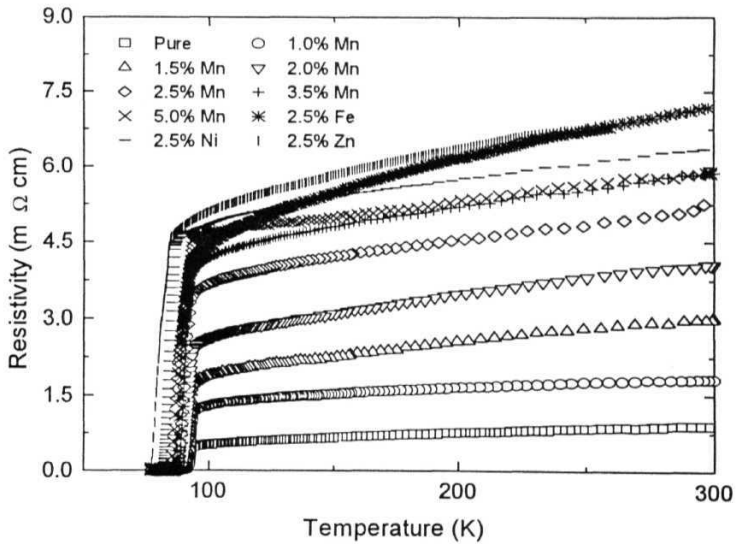


Figure 2 Temperature variation of resistivity $\text{YBa}_2(\text{Cu}_{1-x}\text{Mn}_x)_3\text{O}_{7-\delta}$ samples with $x=0, 0.01, 0.015, 0.02, 0.025, 0.035, 0.05$ and a $\text{YBa}_2(\text{Cu}_{0.975}\text{Fe}_{0.025})_3\text{O}_{7-\delta}$ sample.

3.1.1 RESULTS AND DISCUSSION :

Figure 3.2 shows the temperature variation of resistivity for the $\text{YBa}_2(\text{Cu}_{1-x}\text{Mn}_x)_3\text{O}_{7-\delta}$ with $x=0, 0.01, 0.015, 0.02, 0.025, 0.035, 0.05$ and $\text{YBa}_2(\text{Cu}_{0.975}\text{Fe}_{0.025})_3\text{O}_{7-\delta}$ sample. Typically the resistivity drops linearly with temperature from the room temperature value of $\rho(300)$ as the temperature is reduced close to $2T_c$, which is

around 200 K. At temperatures below 200 K a negative deviation from the linearity, increasing with decreasing temperature is observed. This observed excess conductivity at temperatures below 200 K is due to the superconducting fluctuation which manifests itself as rounding-off of resistivity curve above T_c [25,26]. The onset of resistivity transition, $T_{c(\text{onset})}$ did not vary much, but the zero resistivity temperature T_{zero} dropped significantly on doping (Table 3.1.). The transition width was typically of the order of 3.5 K , except for the 2.5 % Zn doped sample which showed 5.92 K width and the 5.0 % Mn doped sample that exhibited $\Delta T_c=7.01$ K. Normal state resistivity increases monotonically with the dopant concentration. The $\rho(T)$ observed above 200 K was fitted to the linear equation and the obtained parameters, slope ($d\rho/dT$) and the intercept ($\rho(0)$) are tabulated in Table 3.1. $\rho(0)$, calculated from the linear extrapolation of the $\rho(T)$ to zero Kelvin is also found to increase monotonically with Mn content.

Table 3.1 Experimental resistivity transition Onset , $T_{c(\text{onset})}$, zero resistivity temperature, T_{zero} , the linear fit parameters for $\rho(T)$ above 200 K: the slope ($d\rho/dT$) and the intercept ($\rho(0)$).

Sample	$T_{c(\text{onset})}$ (K)	T_{zero} (K)	ΔT_c (K)	$d\rho/dT$ ($\mu\Omega \text{ cm/K}$)	$\rho(0)$ ($\mu\Omega \text{ cm}$)
Pure	93.5	89.7	1.67	1.31	0.51
1.0 % Mn	93.8	88.4	3.64	1.22	1.47
1.5 % Mn	93.5	89.7	2.19	3.77	1.86
2.0 % Mn	93.3	88.9	3.32	5.17	2.52
2.5 % Mn	92.6	86.7	3.78	6.83	3.13
3.5 % Mn	92.6	87.2	3.47	7.14	3.74
5.0 % Mn	93.5	85.1	7.01	4.41	4.55
2.5 % Fe	92.1	86.7	3.35	10.20	4.14

$\rho(300)$ increases linearly and saturates above 3.5 % of Mn doping which could be due to the solubility limit of Mn in YBCO [27]. $\rho(\text{onset})$ and $\rho(0)$ also shows a slower rate of

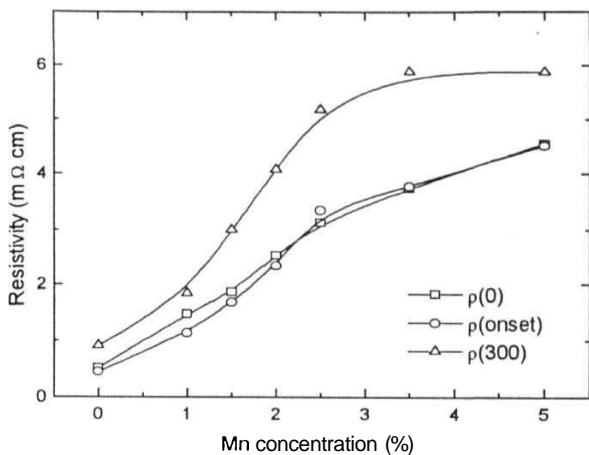


Figure 3.3 Plot of variation of $\rho(0)$, $\rho(\text{onset})$ and $\rho(300)$ for $\text{YBa}_2(\text{Cu}_{1-x}\text{Mn}_x)\text{O}_{7-x}$ sample, for varying dopant concentration of $x = 0, 0.01, 0.015, 0.02, 0.025, 0.035$ and 0.05 sample

increase with dopant concentration above $x=0.025$. Figure 3.3 shows variation of $\rho(0)$, $\rho(\text{onset})$ and $\rho(300)$ with the dopant concentration. The thermal coefficient of resistivity ($d\rho/dT$) increased from $1.31 \mu\Omega\text{cm K}^{-1}$ for the undoped sample to $7.14 \mu\Omega\text{cm K}^{-1}$ for the 3.5 % Mn doped sample. The Fe doped sample showed the highest thermal coefficient of $10.2 \mu\Omega\text{cm K}^{-1}$ as well as a larger normal state resistivity than that for the 2.5 % Mn doped samples.

3.2 SEEBECK COEFFICIENT:

Compared to resistivity and Hall coefficient measurements, Seebeck coefficient measurement is a faithful technique in probing the transport phenomena with minimal distortion arising from the defect structures etc., which are not characteristic of the sample studied. Seebeck coefficient measurement has been reported on $\text{La}_{2-x}(\text{Sr,Ba})_x\text{CuO}_4$ system [28], $\text{YBa}_2\text{Cu}_3\text{O}_{7-x}$ (YBCO) system [10,12,29,30], $\text{Bi}_2\text{Sr}_2\text{Ca}_1\text{Cu}_2\text{O}_{8+y}$ system [31,32,33], $\text{Tl}_2\text{Ba}_2\text{Ca}_2\text{Cu}_3\text{O}_y$ system [34,35] and $\text{HgBa}_2\text{Ca}_2\text{Cu}_3\text{O}_{8+x}$ [36,37] system and the results

obtained in the transport measurements were analysed in the light of energy band calculations to understand the transport mechanism involved [10,12,38 ,39].

The Fermi Energy (E_f) of $YBa_2Cu_3O_{7-\delta}$ system falls in the vicinity $Cu-3d$ and $O-2p$ orbitals and these orbitals constitute the superconductivity in this system. This was supported by the angle resolved photo emission experiments [40,41,42] and the band calculations [7,43]. Consequently doping at the Cu site of $YBa_2Cu_3O_{7-\delta}$ or varying Oxygen content [8,9,44,45] directly alters the charge carriers at the vicinity of E_f and thus modify the transport properties. Variation of hole concentration shows a parabolic effect on T_c , with an optimum value of hole concentration, p_h where the T_c is maximum [46]. Similar effects of hole depletion is observed in $YBa_2Cu_3O_{7-\delta}$ samples with Pr doped at the Y site [47]. Das *et al.* [48] have measured thermopower on $Nd_{1-x}Pr_xSrBaCu_3O_7$ and established decrease in hole density with Pr content. Fisher *et. al* [38] reported resistivity and thermopower measurements on $YBa_2Cu_{3-x}Co_xO_{7-\delta}$ system and concluded the presence of a very narrow band at the E_f . This narrow band scenario is supported by Houssa *et al.*[49] from the thermal conductivity studies on $YBa_2(Cu_{1-x}Zn_x)_3O_{7-\delta}$ samples. Obertelli *et. al.* [9] have brought forth the close correlation existing between the thermo electric power (TEP) and the superconductivity on several cuprate superconductors. They have pointed out the crossing over of the sign of the TEP at the vicinity of T_c maximum on optimal hole doping. Seebeck coefficient measurement along a and b axes of high quality single crystals [29] pointed out the clear distinction between the CuO_2 plane and CuO chain thermopower. The a - $axis$ thermo power has been found to be more closer to the inplane thermo power of other cuprate superconductors, whereas the b - $axis$ value of Seebeck coefficient is highly sensitive to Oxygen content and is quite temperature independent at high temperatures, indicating the charge carriers along the chain may be from a very narrow band.

Measurement of temperature variation of Seebeck coefficient was carried out on the Mn doped polycrystalline $YBa_2Cu_3O_{7-\delta}$ aimed at probing the alteration of the Fermi surface by the Mn dopant and to compare it with the Fe doped sample. In this report, we present the Seebeck coefficient results $YBa_2(Cu_{1-x}Mn_x)_3O_{7-\delta}$ with x varying from 0 to 0.05, analyzed in terms of the existing theoretical structure, *via.* metallic thermopower model, Nagaosa and Lee model and Gasumyants' narrow band model.

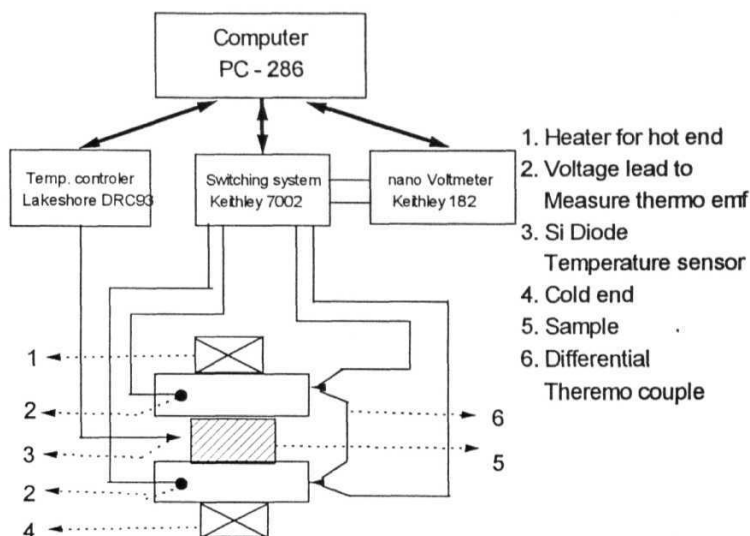


Figure 3.4 Schematic diagram of the setup used for Seebeck coefficient measurement

3.2.1 EXPERIMENTAL

The schematic diagram of the experimental setup for the measurement of temperature variation of Seebeck coefficient is shown in Figure 3.4. The measurements were carried out following the conventional differential technique. Pressure contacts were made against the freshly prepared sample surfaces using two spring held - high pure copper blocks, which served as heat source and sink to the sample as well as were used to measure the differential thermo *emf* developed across the sample. The upper copper block was provided with a heater to enable constant heat supply. The two junctions of the differential thermo couple were fixed on the copper blocks to monitor the temperature difference across the sample. The sample and the copper block arrangements were contained in vacuum tight containment, which was evacuated and filled with Helium exchange gas. A radiation shield also was provided around the sample within the vacuum containment. A temperature gradient of 1-3 K was maintained across the sample during the measurement. A Keithley 7002 switching system was employed to control the Keithley 182

nano Voltmeter in measuring the voltage across the differential copper-constantan thermocouple and the thermo *emf* (AV) developed across the sample. Copper correction was done to obtain the absolute thermo power, S.

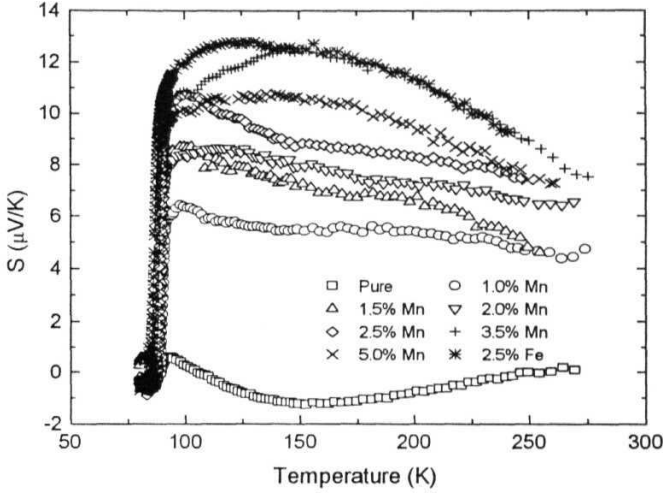


Figure 3.5 Temperature variation of Seebeck coefficient for $YBa_2(Cu_{1-x}Mn_x)_3O_{7-\delta}$ samples with $x=0, 0.01, 0.015, 0.02, 0.025, 0.035, 0.05$ and a $YBa_2(Cu_{0.975}Fe_{0.025})_3O_{7-\delta}$ sample

3.2.2 RESULTS AND DISCUSSIONS:

Figure 3.5 shows the temperature variation of Seebeck coefficient, S for the above mentioned samples. The normal state $S(T)$ shows a change over from a concave behavior for the pure and low dopant concentration, to a convex behavior for doping above 3.5% of Mn and the Fe doped sample. The $S(T)$ for the pure sample is much similar to the *b*-axis thermopower reported by Cohn *et. al.* [29] on the untwinned $YBa_2Cu_3O_{7-\delta}$ crystal. Tallon *et al.* have identified $S(290)$ as reliable gauge for measuring hole concentration, since $S(290)$ vs. p_h follows a universal curve for the high T_c cuprate superconductors, given as [50],

$$S(290) = 372 \cdot \exp(-32.4 p_h) \text{ for } 0.00 < p_h < 0.05 \quad (3.3)$$

$$S(290) = 992 \exp(-38.1 p_h) \text{ for } 0.05 < p_h < 0.155 \quad (3.4)$$

$$S(290) = -139p_h + 24.2 \quad \text{for } p_A > 0.155 \quad (3.5)$$

Following the above equation, p_h was determined and is given in the Table 3.2. The hole concentration, p_h , a decreasing trend with increasing dopant concentration.

Table 3.2 Fit parameters to the metallic diffusion model and p , the hole concentration calculated from the $S(290)$, following Eqn. 3.3-3.5. a , the weightage factor to the metallic diffusion contribution; b , the weightage factor to the phonon drag contribution and c , the additional constant.

Sample	a $\mu\text{V/K}^2$	b μV	c	p_n
Mn				
0.0	3.865×10^2	1010.34	-13.691	0.177
1.0	1.604×10^2	460.094	-	0.145
1.5	1.643×10^2	706.167	-	0.132
2.0	1.620×10^2	814.422	-	0.139
2.5	1.942×10^2	896.475	-	0.123
3.5	-7.902×10^2	-1711.178	35.541	0.130
5.0	-6.012×10^2	-1083.394	26.860	0.115
Fe				
2.5	-6.997×10^2	-1248.157	13.691	0.123

3.2.2.1 Modeling and Analysis :

Classically the temperature variation of thermo electric power in metals was explained from the Fermi distribution of the charge carriers under a temperature gradient. The Seebeck Coefficient, S , calculated from the extra energy required in transporting an electron from the lower temperature end to the higher temperature end in terms of electronic specific heat is given as [51]

$$S = \int \frac{C_e(T)}{neT} dT \quad (3.6)$$

where $C_e(T)$ is the electronic specific heat capacity, n , the electron density and e , the electronic charge. But this simple expression neglects various scattering processes the electron transport encounters on a real situation arising from crystal defects, phonons, etc. $S(T)$ under strong scattering conditions was given by Mott and Davis [52] as

$$S(T) = \frac{k}{e\sigma} \int \sigma(\varepsilon) \left(-\frac{\partial f}{\partial \varepsilon} \right) \frac{\varepsilon - \varepsilon_f}{kT} d\varepsilon \quad (3.7)$$

where $\sigma(\varepsilon)$ is the transport function and the other symbols take the usual notations. Using appropriate transport function, $\sigma(\varepsilon)$, the effect of different transport mechanism on $S(T)$ can be derived.

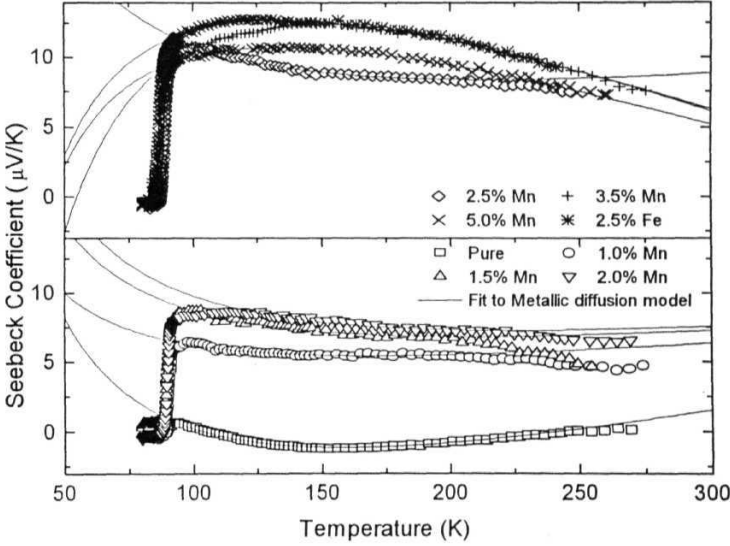


Figure 3.6 Metallic diffusion model fit to the $YBa_2(Cu_{1-x}Mn_x)_3O_{7-\delta}$ samples with $x=0, 0.01, 0.015, 0.02, 0.025, 0.035, 0.05$ and a $YBa_2(Cu_{0.975}Fe_{0.025})_3O_{7-\delta}$ sample. Solid lines are the theoretical simulations.

3.2.2.2 Metallic Diffusion Model :

Kaiser *et. al.* [53] have proposed an enhanced phonon-electron contribution to explain the nonlinear behavior of $S(T)$ observed at the high temperature region of $YBa_2Cu_3O_{7-\delta}$. Unlike resistivity, Seebeck coefficient increases with electron-phonon interaction which explains the linear variation of $p(T)$ even as $S(T)$ changes in a non-linear

fashion. But Vijayashree *et al.* [54], from their TEP study on Zn doped $\text{YBa}_2\text{Cu}_3\text{O}_{7-x}$, found $S(T)$ to vary more steeply than any electron-phonon enhancement could account for. Several authors have tried to account for the peak in 100 - 150 K to phonon drag effect [10,39] arising from momentum transfer between the phonons and the charge carriers. Following the Debye's law, phonon drag is expected to increase as T^3 at low temperature and diminish as T^{-1} at higher temperatures ($T > \Theta_D$, the Debye temperature), because of the anharmonic phonon-phonon scattering, thus accounting for a peak at low temperatures. But the peak observed near T_c in the high temperature superconductors is at too high temperatures to be accounted for by the above phenomena. But Cohn *et al.* [39] have argued that at low temperature the freezing of carrier-optical phonon interaction, responsible for phonon drag at temperatures below 160 K, could result in an enhancement of S and have obtained good fit for the ab - plane thermo power measured on crystalline YBCO samples. We have fit our experimental results to the metallic thermo power given as [39]

$$S = a.T + \frac{b}{T} \quad (3.8)$$

Here, the first term corresponds to the diffusion thermopower and the second one to the phonon drag. For some of the samples, an additional constant was necessary to obtain a good fit. Figure 3.6 shows the experimental and simulated plots for the metallic diffusion thermopower model given by Eqn.3.8 and the fit parameters are given in Table 3.2. The phonon contribution is enhanced with increasing amount of dopant. The sign of the phonon contribution indicates the direction of momentum transfer [55] and is affected by the hole concentration. In our samples, for $x > 0.035$ the phonon drag contribution is found to be negative, indicating a reversal in momentum transfer.

3.2.2.3 Nagaosa and Lee Model :

Nagaosa and Lee [3] have studied the Resonating Valence Band (RVB) wherein they assume that the Fermions and the spinless Bosons are coupled by a gauge field. On integrating the fluctuation in the gauge field, the transport properties will be the sum of the Boson contribution and the Fermion contribution [56]. Thus the Seebeck coefficient can be written as [3]

$$S = S_f + S_B \quad (3.9)$$

where,

$$S_f = - \left(\frac{k_B}{e} \right) \frac{k_B T}{E_f} \quad (3.10)$$

$$S_B = \frac{k_B}{e} \left(1 - \ln \frac{2\pi p}{mk_B T} \right) \quad (3.11)$$

In the above equation for Bosonic contribution of thermopower **we assume the** Bosons to be the cooper pairs and the effective mass is taken as **$2m_\phi$** . Thus this **model** gives us a direct correlation between $S(T)$, hole concentration and E_f .

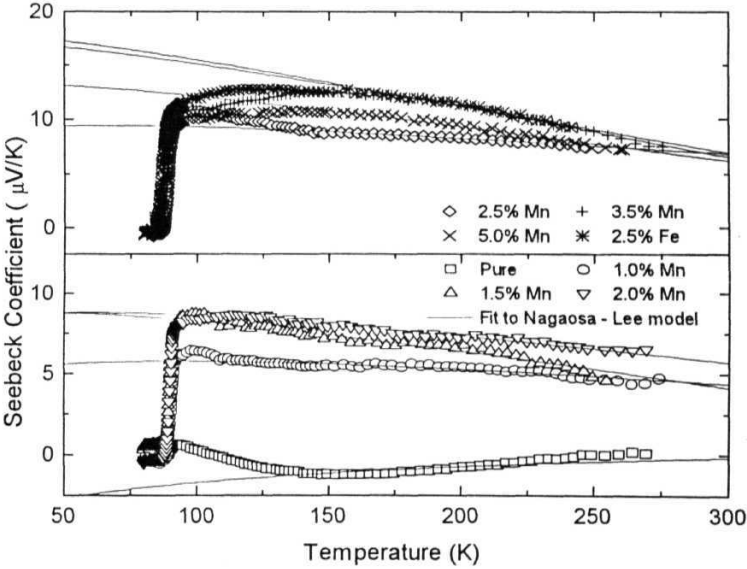


Figure 3.7 Nagaosa and Lee model fit to $\text{YBa}_2(\text{Cu}_{1-x}\text{Mn}_x)_3\text{O}_{7-\delta}$ samples with $x=0, 0.01, 0.015, 0.02, 0.025, 0.035, 0.05$ and a $\text{YBa}_2(\text{Cu}_{0.975}\text{Fe}_{0.025})_3\text{O}_{7-\delta}$ sample. Solid lines represent simulated curves.

Our experimental results are compared with the simulated ones following the **above** equation. A weightage factor, F_{NL} , was used to determine the contribution coming from S_B .

Thus obtained simulated plots are shown in Figure 3.7. **The fit parameters are given in Table 3.3 and are in the reasonable range except for the pure sample. For samples upto 2.0 % Mn fit was done in the temperature range of 100 K -250 K, whereas for samples with dopants above 2.5 %, it could be fitted in the temperature range of 150 K - 250 K only. As the Boson formation due to thermodynamic fluctuations is very unlikely above**

Table 3.3 Fit parameters to the Nagaosa and Lee model. E_f , the Fermi energy, p_h , the hole concentration and F_{NL} , the weightage factor to the Bosonic contribution in the total Seebeck coefficient measured.

Sample	E_f meV	p_h	F_{NL}
Mn			
1.0	442.8	0.154	1.496×10^2
1.5	271.3	0.167	1.434×10^2
2.0	348.6	0.167	1.439×10^2
2.5	389.0	0.169	1.429×10^2
3.5	146.2	0.033	1.285×10^2
5.0	205.2	0.029	1.382×10^2
Fe			
2.5	157.9	0.031	1.302×10^2

$2T_c$, the Bosonic contribution to the Seebeck coefficient, S_B , will diminish at higher temperatures. Thus the samples with higher dopant concentration whose measured data could be fitted only at higher temperature range are expected to have low Bosonic contribution. This is feebly indicated by F_{NL} parameter obtained. But the abrupt drop by an order in the magnitude of p_h estimated from the Bosonic contribution to Seebeck coefficient for samples with $x > 0.035$ of Mn doping and the Fe doped sample could be due to the fall in magnitude of S_B . The Fermi energy, E_f , estimated from the fit decreases from 442 meV for the 1 % Mn doped sample to 146 meV for the 3.5 % Mn doped sample. The E_f for the 2.5 % Fe doped sample is estimated to be 157 meV. This fall in the E_f could be an indication of the reduction of the charge carriers on doping, both Mn and Fe alike.

3.2.2.4 Gasumyants Narrow Band Model :

The temperature independent region of **thermopower** observed in $YBa_2Cu_3O_{7-x}$ system had been explained by considering a narrow band at the E_f [12,29,38]. The saddle point observed at the high resolution angle resolved photo emission on the cuprate superconductors [10,57] points to a logarithmic density of states singularity (*Van Hove Singularity*) close to the E_f . Gasumyants *et al* [6] have attempted a quantitative estimation of the transport properties, under the narrow band considerations, using a few phenomenological parameters such as band width(W_D), width of the conduction window(W_σ) and degree of band filling(F). The narrow band could be either a single narrow band in the DOS, or a narrow peak on a broad background.

On applying the narrow band limitation $W \ll k_B T$, to the Eqn.2, we get [53]

$$S = \frac{k_B}{e} \ln \left(\frac{F}{1-F} \right) \approx \frac{E - \mu}{eT}$$

To highlight the influence of the band width value Gasumyants *et al* [6] have performed the calculations of the transport integrals, retaining only the terms upto second or third power in the distribution function expanded as a *Taylor's* series. Under this approximation, $S(T)$ for $W \approx k_B T$ is given as [6]

$$S = \frac{k_B}{e} \left(\frac{W_\sigma^*}{\sinh[W_\sigma^*]} \left[e^{\mu^*} + \cosh[W_\sigma^*] - \frac{\cosh[\mu^*] + \cosh[W_\sigma^*]}{W_\sigma^*} \ln \left(\frac{e^{\mu^*} + e^{W_\sigma^*}}{e^{\mu^*} + e^{-W_\sigma^*}} \right) \right] - \mu^* \right) \quad (3.13)$$

$$\mu^* = \frac{\mu}{k_B T} = \ln \left(\frac{\sinh[F W_\sigma^*]}{\sinh[(1-F) W_\sigma^*]} \right) \quad (3.14)$$

where, μ is the chemical potential,

$$W_\sigma^* \equiv W_\sigma / 2k_B T \text{ and } W_D^* \equiv W_D / 2k_B T$$

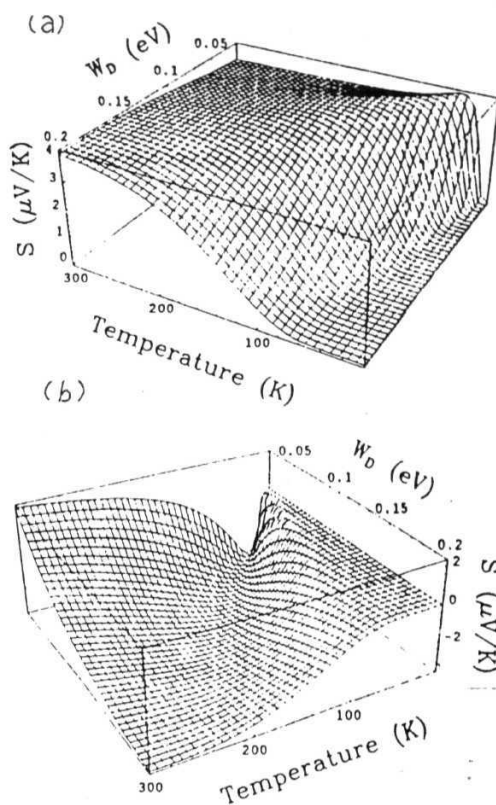


Figure 3.8a Temperature variation of Seebeck coefficient for **varying band width(W_D)**, given by Gasumyants' narrow band model. **(b)** Effect of a small asymmetry factor of $b=0.02$ W_D added about E_F .

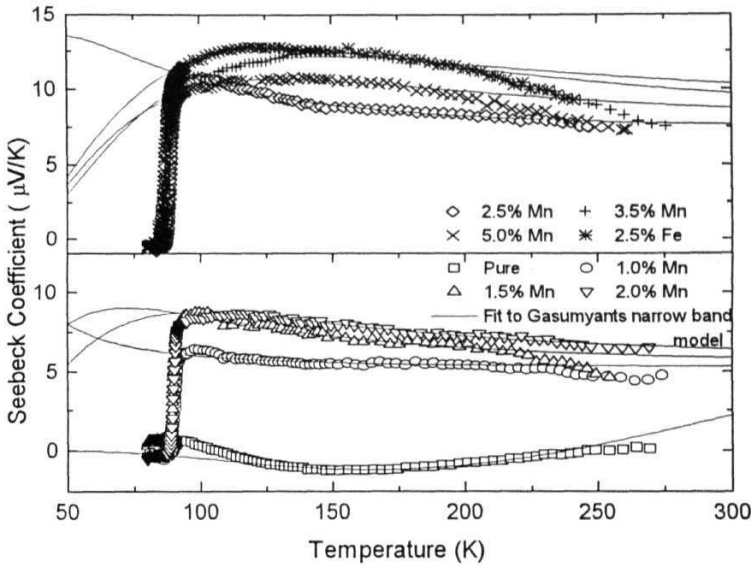


Figure 3.9 Gasumyants' narrow band model fit to $YBa_2(Cu_{1-x}Mn_x)_3O_{7-\delta}$ samples with $x=0, 0.01, 0.015, 0.02, 0.025, 0.035, 0.05$ and a $YBa_2(Cu_{0.975}Fe_{0.025})_3O_{7-\delta}$ sample. Theoretical simulations are shown as solid lines.

We have used the above equation to simulate the *TEP* profile as a function of Temperature and the band width, W_D . Figure 3.8a shows the temperature variation of S for varying W_D . It is evident from the figure that the low temperature hump observed in the high T_c superconductors can be explained in terms of the narrowness of the expected band. It can be seen that as the bandwidth decreases a broad hump on S vs. T appears and moves toward the lower temperature as W_D further decreases. Further, to illustrate the effect of asymmetry added to the Eqn.3.13 we have plotted in Figure 3.8b the temperature variation of S for varying W_D with a small asymmetry factor, $b=0.02 W_D$, added to the band about E_F . Here, $S(T)$ varies just in the same fashion as in the symmetric case but on the negative side, at higher W_D . And at low W_D , $S(T)$ shows some interesting features such as $S(T)$ going negative at low temperature and then raising smoothly until it saturates at high

temperatures. This kind of behavior is reported on the *b*-axis thermopower measured on untwined $YBa_2Cu_3O_{7-x}$ single crystal [29]. In our measurements the undoped sample shows similar behavior.

Table 3.4 Fit parameters to the Gasumyants narrow band model. F, the filling factor, W_D , the band width and c, the ratio of conduction window to the total band width(W/W_D).

Sample	F	W_D	c
	meV		
Mn			
0.0	0.607	144.778	0.652
1.0	0.515	23.040	0.039
1.5	0.515	72.389	0.323
2.0	0.516	88.578	0.355
2.5	0.521	53.502	0.292
3.5	0.524	119.494	0.385
5.0	0.521	108.963	0.379
Fe			
2.5	0.521	133.089	0.317

We have fitted the experimental results to the Eqn.10 by least square refinement, keeping F, W_D and c ($=W_c/W_D$) as fitting parameters. Also using a small **asymmetry** factor good fit was obtained for the pure sample. But the parameters obtained are not continuous with those calculated from symmetric fit. Figure 3.9 shows the calculated and **experimental** S(T) plots. The fit parameters are given in the Table 3.4. The width of the **narrow band**, as seen from the W_D , increases from 23 meV for the $x=0.01$ sample to 119 meV for the $x=0.035$ sample. The filling factor increases from 0.515 for the 1% Mn doped sample to 0.524 for the 3.5 % Mn doped sample. The conduction window (W_c) varies marginally around 35% of W_D for the different samples studied but shows no systematic change. This means Anderson localization [58] is invariant with doping.

3.3 **REFERNECES:**

1. P. W. Anderson, *Science*, 235, **1196** (1987).
2. S. Massida, J. Yu and A. J Freeman, *Physica*, **C152**, 251 (1988).
3. N. Nagosa and P. A. Lee, *Phys. Lett.*, **64**, 2450 (1990).
4. C. M. Varma, P. B. Littlewood, S. Schmitt-Rink, E. Abrahams and A. E. Ruckenstein, *Phys. Lett.* 63, 1996(1989)
5. J. Ruvald and A. Virosztek, *Phys. Rev.*, **B42**, 329 (1990)
6. Gasumyants, V. I. Kaidanov and E. V. Vladimirkaya, *Physica* **C248**, 255 (1995).
7. D. M. Newns, C. C. Tsuei, R. P. Huebener, P. J. M. Van Bentum, P. C. Pattnaik and C. Chi, *Phys. Rev. Lett*, 73, 1695 (1994).
8. J. D. Jorgensen, B. W. Veal, A. Paulikas, L. J Nowicki, G. W. Crabtree, H. Claus and K. W. Kwok, *Phys. Rev.*, **B41**, 1863 (1990).
9. S. D. Obertelli, J. R. Cooper and J. L. Tallon, *Phys. Rev.*, **B46**, 14928 (1992).
10. J. W. Cochrane, A. Hartmann and G. J. Russell, *Physica* C265, 135 (1996).
11. B. Fisher, J. Genossar, L. Patlagan, G. M. Reisner and A. Knizhnik, *J. Appl. Phys.*, 80, 898(1996).
12. K. R. Krylov, A. I. Ponomarev, I. M. Tsidilkovski, V. I. Tsidilkovski, G. V. Bazuev, V. L. Kozhevnikov and S. M. Chesnitski, *Phys. Lett, A* **131**, 203 (1988).
13. N. F. Mott, *"Metal Insulator Transitions"*, (Taylor & Francis, London, 1974).
14. S. Chakravarty, B. I. Halperin and D. R. Nelson, *Phys. Rev. Lett.*, 60, 1057(1988).
15. R. J. Birgeneau and G. Shirane, in *"Physical Properties of High Temperature Superconductors"*, Ed. D. M. Ginsberg (World Scientific, Singapore, 1989), Vol. I, p. 152.
16. H. Takagi, S. Uchida, H. Iwabuchi, H. Eisaki, K. Kishio, K. Kitazawa, K. Feuki and S. Tanaka, *Physica* **B148**, 349(1987)
17. Y. Iye in *"Physical Properties of High Temperature Superconductors"*, Ed. D. M. Ginsberg (World Scientific, Singapore, 1989), Vol. III, p. 294.
18. D. R. Harshman and A. P. Mills Jr., *Phys. Rev.* **B45**, 10684 (1992).
19. Raju P. Gupta and Michele Gupta, *Phys. Rev.* **B59**, 3381 (1999).
20. V. E. Gasumyants, M. V. Elizarova and I. B. Patrina, *Phys. Rev.* **B59**, 6550 (1999).

- 21 S. Martin, M. Gurvitch, C. E. Rice, A. F. Hebard, P. L. Gammel, R. M. Flemming and A. T. Fiory, *Phys. Rev.* **B38**, 834 (1989).
- 22 T. A. Friedmann, M. W. Rabin, J. Giapintzakis, J. P. Rice and D. M. Ginzberg, *Phys. Rev.*, **B42**, 6217(1990).
- 23 P. W. Anderson and Z. Zou, *Phys. Rev. Lett*, 60, 132 (1988).
- 24 Nianhua Peng and W. Y. Liang, *Physica C*233, 61 (1994).
- 25 W. J. Skocpol and M. Tinkham, *Rep. Progr. Phys.*, 38, 1049 (1975).
- 26 R. Srinivasan in "Int. Conf. On Superconductivity - ICSC" Jan, 10 - 14, 1990. Bangalore, India. Editors, S. K. Joshi, C. N. R. Rao and S. V. Subramanyam, (World Scientific, Singapore, 1990) p.147.
- 27 R. F. Jardim and S. Gama, *Physica C***159**, 306 (1989).
- 28 M.Sera and M. Sato, *Physica C***185-189**, 1339 (1991).
- 29 J. L. Cohn, E. F. Skelton, S. A. Wolf and *Phys. Rev.*, **B45**, 13140 (1992).
- 30 P. Gerdanian and C. Picard, *Physica C***246**, 145 (1995).
- 31 L. Forro, J. Lukatela and B. Keszer, *Sol. St. Comm.*, 73, 501 (1990).
- 32 J. B. Mandal, S. Keshri, P. Mandal, A. Poddar, A. N. Das and B. Gosh, *Phys. Rev.* **B46**, 11840(1992).
- 33 R. Wang, H. Sekine and H. Jin, *Supercond. Sci. Tech.* 9, 529(1996).
- 34 Y. Xin, K. W. Wang, C. X. Fan, Z. Z. Sheng and F. T. Chang, *Phys. Rev.* **B48** 557(1993).
- 35 N. Mitra, J. Trefny, B. Yarar, G. Pine, Z. Z. Sheng and A. M. Hermann, *Phys. Rev.* **B38**, 7064(1988).
- 36 C. K. Subramaniam, M. Paranthaman and A. B. Kaiser, *Phys. Rev.* **B51**, 1330(1995).
- 37 Y. T. Ren, J Clayhold F. Chen, Z. J. Huang, X. D. Qiu, Y. Y. Sun, R. L Meng, Y. Y. Xue and C. W. Chu, *Physica C***217**, 6(1993).
- 38 B. Fisher J. Genossar, L. Patlagan and G. M. Reisner, *Phys. Rev.* **B48**, 16056(1993).
- 39 J. L. Cohn, S. A. Wolf, V. Selvamanickam and K. Salama, *Phys. Rev. Lett*, **66** 1098(1991).
- 40 T. Takahashi, H. Matsuyama, H. K. Yoshida, Y. Okabe, S. Hosoya, H. Seki, H. Fujimoto, M. Sato and H. Inokuchi, *Phys. Rev.*, **B39**, 6636(1989).
- 41 R. Manzsche, T. Buslaps, R. Claessen, M. Skibowski and J. Fink, *Physica C***162-164**, 1381(1989).

- 42 C. G. Olson, R. Liu, D. W. Lynch, R. S. List, **A. J. Arko, B. W. Veal, Y. C. Chang, P. Z. Jiang** and A. P. Paulikas, *Phys. Rev.*, **B42**, 381(1990).
- 43 S. Massida, J. Yu and A. J. Freeman, *Physica* **C152,251(1988)**.
- 44 J. M. Tarascon, P. Barboux, P. F. Miceli, L. H. Greene, G. W. Hull, **M. Eibschutz** and **S. A. Sunshine**, *Phys. Rev.* **B37**, 7458(1988).
- 45 R. J. Cava, A. H. Hewat, E. A. Hewat, B. Batlogg, M. Marezio, K. M. Rabe, J. J. Krajewski, W. F. Peck Jr. and L. W. Rupp Jr., *Physica* **C165**, 419(1990).
- 46 M. R. Presland, J. L. Tallon, R. G. Buckley, R. S. Liu and N. E. Floer, *Physica*, **C176**, 95(1991).
- 47 A. P. Goncalves, I. C. Santos, E. B. Lopes, R. T. Henriques, **M. Almeida** and **M. O. Figueiredo**, *Phys. Rev.* **B37**, 7476(1988).
- 48 A. Das, R. Suryanarayanan, I. Zelelnay and B. Dabrowski, *Physica* **C273**, 301 (1997).
- 49 M. Houssa, M. Ausloos and R. Cloots, *Phys. Rev.* **B56**, 6226 (1997).
- 50 J. L. Tallon, C. Bernhard, H. Snaked, R. L. Hitterman and J. D. Jorgensen, *Phys. Rev.* **B51**, 12911(1995).
- 51 "Low Temperature Solid State Physics" by Rosenberg, (Clarendon, Oxford - 1965).
- 52 "Electron processes in non crystalline materials" by N. F. Mott and E. A. Davis, (Clarendon, Oxford - 1979)
- 53 A. B. Kaiser and G. Mountjoy, *Phys. Rev.*, **B43**, 6266(1991).
- 54 V. Radhakrishnan, C. K. Subramanian, V. Sankaranarayanan, G. V. **Subba Rao** and R. Srinivasan, *Phys. Rev.*, **B40**, 6850(1989).
- 55 H. J. Trodahl, *Phys. Rev.*, **B51**, 6175(1995).
- 56 L. B. Ioffe and A. I. Larkin, *Phys. Rev.*, **B39**, 8988(1989).
- 57 A. A. Abrikosov, J. C. Campuzano and K. Gofron, *Physica* **C73**, 214(1993).
- 58 P. W. Anderson, *Phys. Rev.*, **109** 1492(1958).

CHAPTER - 4

MAGNETIC PROPERTIES

Magnetization or susceptibility measurements on a superconductor detect signals arising from the circulating persistent shielding currents, in addition to the signals arising from the magnetic properties of the material, usually employing an inductive technique. The zero field cooled (ZFC) curve of dc susceptibility demonstrates the flux shielding (flux exclusion) property of the superconductor while the field cooled (FC) curve demonstrates the Meissner effect (flux expulsion). But, irrespective of ZFC or FC condition, in the absence of any dc biasing field, ac susceptibility always measures the shielding property of the superconductor. In a defect free ideal superconductor the equilibrium magnetization M_{eq} is associated with surface screening currents flowing over London's penetration depth, both in Meissner state ($H < H_{c1}$) and in mixed state ($H > H_{c1}$). However, in real situation any crystal defect, grain boundaries, etc. act as pinning centers that trap the flux to give the resultant flux gradient and hence the current flow within the sample, even beyond London's penetration depth. In Type II superconductors if flux pinning is present Meissner effect will not be pronounced, because of the large trapped flux at the pinning sites. Nevertheless, these pinning sites arrest the vortex motion and hence enhance critical current density (J_c) appreciably.

In sintered $\text{YBa}_2\text{Cu}_3\text{O}_{7-\delta}$ superconductors, Evetts and Glowacki [1] reported that the hysteretic behavior of critical current density was due to the field from trapped flux. Also, uniform dispersion of fine particles ($-0.5 - 1.0 \mu\text{m}$) of Y_2BaCuO_5 in $\text{YBa}_2\text{Cu}_3\text{O}_{7-\delta}$ grains act as pinning centers and enhance J_c effectively at higher magnetic fields and temperature [2]. Xu *et al* [3] have measured irreversibility temperature on pure and 2 % Ni, Zn, Al and Fe doped $\text{YBa}_2\text{Cu}_3\text{O}_{7-\delta}$ superconductors from DC magnetization measurement and suggest that the irreversibility line could represent the depinning line.

In high temperature superconductors (HTSC), the granular nature has also added to the complexity in the understanding of the magnetic properties of these materials. ac measurements are useful in studying the weak link nature of the superconductor while DC magnetization measurements are widely used to probe the grain properties, because of the higher field capabilities possible in DC magnetization measurements. Study of magnetic properties on doped $\text{YBa}_2\text{Cu}_3\text{O}_{7-\delta}$ has been of fundamental importance in the understanding and optimization of the properties of this technologically potential material.

Due to the low solubility [4] limit of Mn in $\text{YBa}_2\text{Cu}_3\text{O}_{7-\delta}$ a thorough study on magnetic properties of this system is not present in the literature. Dhingra *et al* [5] have reported reduction in diamagnetic signal and broadening of transition beyond 1% Mn doping. Saini *et al* [6] also have reported reduction in superconducting fraction and broadening of transition. Mn is known to take Cu(I) site [7] from the neutron diffraction experiments. In the current work we have studied the temperature variation of ac susceptibility, DC magnetization and ac MH loop measurements on Mn doped YBCO within the low solubility regime and have compared the results with those of a Cu(I) site dopant - Fe and Cu(II) site dopants - Ni and Zn, prepared under similar conditions.

4.1 ANALYTICAL FRAME WORK

The irreversible magnetization of Type II superconductors is a manifestation of their critical current density. Due to the short coherence length and the consequent intrinsic pinning, the irreversible magnetization has become prominent in HTSC. Mendelssohn [8] explained the hysteresis observed in the hard superconductor by assuming the superconductor to be made of a mesh threaded with superconducting regions of higher critical field, while the mesh itself is superconducting with critical field of lower magnitude. This forms the basis for the critical state models [9]. The irreversible magnetization of the type II superconductors can be quantitatively

analyzed in terms of critical state models. In the critical state, the pinning force balances the Lorentz force exerted by the penetrated supercurrent. Also, the density of the penetrated supercurrent equals the critical current density $J_c(H_i)$ of the material and is a function of the internal field, H_i . From Ampere's law the magnetic flux density profile inside a cylindrical superconductor of radius, R , is given as

$$B(r) = \mu_0 H_a - \mu_0 J_c (R - r) \quad (4.1)$$

From this flux density profile within the sample, magnetization is calculated by integrating the flux density over the entire cross section of the sample, as

$$M = \frac{2}{R^2} \int_0^R r \cdot B(r) dr - H \quad (4.2)$$

Further, by taking Fourier transform of the magnetization relation, complex susceptibility can be derived, as

$$\chi_n' = \frac{1}{\pi H_m} \int_0^{2\pi} M(t) \sin(n\omega t) d(\omega t) \quad (4.3)$$

$$\chi_n'' = \frac{-1}{\pi H_m} \int_0^{2\pi} M(t) \cos(n\omega t) d(\omega t) \quad (4.4)$$

where the applied field is given as,

$$H(t) = H_m \sin(\omega t) \quad (4.5)$$

The first critical state model proposed by Bean [9] assumed the critical current density to be independent of the internal field. Following this model many other critical state models with varied $J_c(H_i)$ were proposed and were applied to different HTSC systems [10,11,12,13,21]. Following are some of the important relations:

Kim's model [14]:

$$J_c(H_i) = \frac{k}{H_0 + |H_i|} \quad (4.6)$$

Power law model [15]:

$$J_c(H_i) = k |H_i|^{-n} \quad (4.7)$$

Exponential model [16]:

$$J_c(H_i) = J_0 \exp\left(-\frac{|H_i|}{H_0}\right) \quad (4.8)$$

Generalized model [17]:

$$J_c(H_i) = \frac{k}{(H_0 + |H_i|)^n} \quad (4.9)$$

In the above relations k , n , J_0 and H_0 are constants and H_i is the internal field.

Kim's relation has been found to adequately explain the weak link magnetization behavior in many of the HTSC [10,12,13]. Analytical solution for the magnetization using the Kim's relation had been derived in the literature, for infinite orthorhombic sample geometry [18] and with superimposed DC field [19]. Chaddah *et al.* [20] have derived analytical solution using exponential model for infinite slab and cylindrical sample geometry. Many other generalized models and analytical solutions are also present in the literature [21,22]

4.1.1 Granular Superconductor :

HTSC are of granular nature and can be considered as superconducting grains weakly linked through Josephson Junctions. This is reflected in magnetic properties as two distinct types of behavior corresponding to the grains and the weak link regions. If M_g is the magnetization due to the grains and M_w is the magnetization due to the weak links then the total observed magnetization will be [10, 23]

$$M = f_g M_g + (1 - f_g) \cdot M_w \quad (4.10)$$

where f_g is the *effective* volume fraction of the grains. Similarly if χ_g is the complex susceptibility of the grains and χ_w is that of the weak links then the total observed complex susceptibility will be

$$\chi = f_g \chi_g + (1 - f_g) \cdot \chi_w \quad (4.11)$$

In the limit of very low applied fields ($H \ll H_{c1g}$), the grains will be in the perfect diamagnetic state, hence $M_g = -H$ and $\chi_g = -1$. Applying this to the above Eqn. 4.10 and 4.11 we get, total magnetization as

$$M = f_g H + (1 - f_g) \cdot M_w \quad \text{for } H \ll H_{c1g} \quad (4.12)$$

and the complex susceptibility as,

$$\chi = -f_g + (1 - f_g) \cdot \chi_w \quad \text{for } H \ll H_{c1g} \quad (4.13)$$

Hence at low fields ($H \ll H_{c1g}$), the weak link magnetization and susceptibility can be calculated from the experimental one using the above relations. Whereas at high fields ($H \gg H_{c2w}$), the weak link becomes completely normal and the magnetization signal from the normal regions will be negligibly small. In such a limit the total magnetization is

$$M = f_g M_g \quad \text{for } H \gg H_{c2w} \quad (4.14)$$

and the complex susceptibility is,

$$\chi = f_g \chi_g \quad \text{for } H \gg H_{c2w} \quad (4.15)$$

Thus at high fields ($H \gg H_{c2w}$), the granular magnetization and susceptibility can be obtained from the experimentally measured one using the above relations.

4.1.2 Numerical Procedure:

Though many $J_c(H_i)$ models were proposed, magnetization equations and susceptibility equations for varied sample geometries were not derived for many of the $J_c(H_i)$ relations because of the mathematical complexity involved in obtaining the analytical solutions. However, these difficulties in computational limitations were effectively overcome by using numerical methods. Following Chen *et al.* [24], we have developed a FORTRAN programme to numerically calculate the magnetization and susceptibility for any arbitrary functional dependence of critical current density on internal field (APPENDIX - I). This procedure is applicable for an infinitely long column of cross-section $2a \times 2b$, with $a < b$. The field, H_a , is applied along the length of the column and hence the screening currents flow around the cross section in a rectangular path which is equidistant from the surface.

For calculation of magnetization, the internal field profile within the sample for the complete field cycle has to be first calculated. To calculate the internal field (H_i) profile, the rectangular cross-section is divided into n rectangular tubes of thickness $dx = a/n$. Field at each tube is calculated applying Ampere's law as:

$$\left(\text{Field at } i^{\text{th}} \text{ tube} \right) = \left(\text{Field at } (i-1)^{\text{th}} \text{ tube} \right) - \left\{ \text{Thickness} \times \left\{ \text{Current density} \right\} \text{ at } (i-1)^{\text{th}} \text{ tube} \right\}$$

$$H_i = H_{i-1} - dx \cdot J_c(H_{i-1}) \quad (4.16)$$

The field at the first tube will be taken as the applied field itself.

The applied field cycle to generate field profile within the sample can be classified into two major categories: (i) Initial magnetization (0 to H_m) and (ii) reverse magnetization (H_m to $-H_m$). During the initial magnetization, as the applied field strength, H_a , is increased from zero to the maximum applied field strength, H_m , the first flux entry into the virgin sample in the form of circulating currents will occur. During the initial magnetization the internal field strength, H_i , within the sample diminishes according to Eqn.(4.16). The induced circulating current will take a direction so as to oppose the increasing applied field. Whereas, in the reverse magnetization, as the field is decreased from the maximum applied field, H_m , the circulating currents are generated in a direction so as to oppose the change and hence will have an opposite sign to the current induced during the Initial magnetization. Depending upon the magnitude of deviation from H_m , reverse current flows upto certain number of tube, i_r , beyond which the initial current continues to flow. Consequently, the field within the sample also increases from H_a at the surface to a maximum value at i_r^{th} tube and decreases beyond that. Thus in the reverse case, circulating currents will change the direction of flow at the i_r^{th} tube from the surface depending upon the magnitude of H_a with respect to H_m . In other words, the tubes 1 to $(i_r - 1)$ carry the current due to reverse magnetization, while the one from i_r to n carry currents due to the initial magnetization. For any tube, the field calculated from the reverse magnetization case cannot be greater than the field calculated from the initial magnetization case. Based on this, one can identify the tube where the current changes direction, i.e. i_r^{th} tube the tube at which, the numerical value of the field calculated from the reverse magnetization case to be greater than the field calculated from the initial magnetization case,.

Numerically, these field profiles within the sample can be generated as follows:

Step 1. Calculation of internal field profile for initial magnetization.

If the maximum applied field, H_m , is greater than the full penetration field, H_p , i.e. $H_m > H_p$, then,

$$H_{i+1} = H_i - J_c(H_i).dx \quad \text{for } i = 1, 2, 3, \dots, n \quad (4.17)$$

If the maximum applied field, H_m , is less than the full penetration field, H_p , then beyond a certain tube, i_p , the above equation will give negative values for the internal field ($H_i < 0$). In such a case, where $H_i < 0$ at tubes beyond i_p , the H_i is taken as zero. In other words,

If $H_m < H_p$, then,

$$H_{i+1} = H_i - J_c(H_i).dx \quad \text{for } i = 1, 2, 3, \dots, i_p \quad (4.18)$$

And

$$H_i = 0 \quad \text{for } i = i_p+1, i_p+2, i_p+3, \dots, n \quad (4.19)$$

Using the above relation field profile can be generated for applied fields, H_a , from zero to H_m for the initial magnetization case..

Step 2. Calculation of internal field profile for reverse magnetization.

In the reverse magnetization case, as the field is reduced from H_m reverse currents flow over tubes, starting from the surface upto i_r^{th} tube. Beyond the i_r^{th} tube initial magnetization currents will continue to flow.

a. Field profile for tubes upto which the reverse current flows, *i.e.* ($i < i_r$)

$$H_{i+1} = H_i + J_c(H_i).dx \quad \text{for } i = 1, 2, 3, \dots, (i_r - 1) \quad (4.20)$$

If the H_i calculated from the above Eqn. 4.20 is greater than the H_i calculated from Eqn. 4.17, that tube is taken as i_r^{th} tube.

b. Field profile for the tubes beyond the change of current direction, where the initial current flows, *i.e.* ($i > i_r$)

If $H_m > H_p$, then,

$$H_{i+1} = H_i - J_c(H_i).dx \quad \text{for } i = i_r, (i_r+1), (i_r+2), \dots, n \quad (4.21)$$

If $H_m < H_p$, then,

$$H_{i+1} = H_i - J_c(H_i).dx \quad \text{for } i = i_r, (i_r+1), (i_r+2), \dots, i_p \quad (4.22)$$

And

$$H_i = 0 \quad \text{for } i = i_p+1, i_p+2, i_p+3, \dots, n \quad (4.23)$$

Thus, using the above relations field profile can be generated for applied fields, H_a , from H_m to $-H_m$ in the reverse magnetization case..

Step 3. Calculation of magnetization from the internal field profile.

Having generated the internal field profile inside the sample, in terms of field in the n tubes, magnetization $M(H)$ can be calculated as

$$M(H) = \sum_{i=1}^n \frac{d_i}{A} H_i dx - H \quad (4.24)$$

where, d_i is the length of the current path and A is the area of cross section of the sample

$$d_i = 4.(2x_i' + b - a) \quad (4.25)$$

$$A = 2a \cdot 2b \quad (4.26)$$

where $x'_i = a - (i - \frac{1}{2})dx$. The above relation can be easily extended to cylindrical geometry by assuming $a = b$. And for a more general form, the supercurrent path can be written as [25]

$$d = 4.(cx'_i + b - a) \quad (4.27)$$

and area of cross section as

$$A = 2ca^2 + 4(b - a)a \quad (4.28)$$

where c is the coefficient appropriate to the particular geometry.

Since the critical state hysteresis loop is symmetric, $-M(H) = M(-H)$. Thus $M(H)$ calculated from the $-H_m$ to H_m in the reverse case, the complete loop can be generated.

Step 4. Calculation of complex susceptibility from the magnetization.

Complex susceptibility can be obtained from the $M(H)$ curve numerically as follows:

Let the applied field H be

$$H_j = H_m \cos\left(\frac{\pi(j - \frac{1}{2})}{N}\right) \quad (4.29)$$

where $j = 1, 2, 3, \dots, N$. Magnetization, $M(H_j)$, corresponding to the above fields are calculated. Then, the real and imaginary parts of susceptibility can be calculated as,

$$\chi' = \frac{\sum_{j=1}^N 2M_j H_j}{NH_m^2} \quad (4.30)$$

and,

$$\chi'' = \frac{\sum_{j=1}^N 2M_j \sqrt{H_m^2 - H_j^2}}{NH_m^2} \quad (4.31)$$

where H_m is the peak amplitude of the applied field. Thus by calculating the real and imaginary parts of susceptibility for varying H_m , field variation of susceptibility for any arbitrary $J_c(H_i)$ can be studied.

4.2 TEMPERATURE AND FIELD VARIATIONS OF AC SUSCEPTIBILITY

In high temperature superconductors (HTSC) critical currents estimated from magnetic measurements show two distinct types of behaviors with respect to the magnitude of applied field (H_a). At low fields (fields less than the lower critical field of the grains, H_{c1g}), the J_c measured will be of intrinsic nature of the weak links (J_{cw}) and constitutes Josephson vortices whereas at higher fields ($H > H_{c1g}$) the measured J_c is of the grains (J_{cg}) and is dominated by flux pinning, flux creep, etc [26]. ac susceptibility measurement is a useful tool to measure the coupling status of these materials. Besides, ac susceptibility can give important material parameters such as J_{cw} and J_{cg} . Several studies on various HTSC superconductors can be found in the literature [10,12,27,28]. Mazaki *et al.* [29,30] have reported complex susceptibility in Fe and Co doped $YBa_2Cu_3O_{7.5}$. Guo *et al.* [31] have studied the Sn and In doped $YBa_2Cu_3O_{7.5}$ and have analyzed the results in terms of an assembly of superconducting loops due to Josephson junctions formed in granular structure. They have proposed a specific scaling of $(T-T_b)/H^{1/2}$ for the real and imaginary parts of magnetic susceptibility where T_b is an effective temperature. Zheng *et al.* [32] have studied the temperature variation of ac susceptibility and dc magnetization in aligned powders of Co and Zn doped $YBa_2Cu_3O_{7.5}$ and have reported that though the J_{cw} and the J_{cg} decreased with doping, the ratio of J_{cg}/J_{cw} was found to be insensitive to doping. This had been attributed to weakening of energy barrier at the pinning sites. Kumaraswamy *et al.* [13] have reported ac susceptibility of Fe, Ni, Co and Ga doped $ErBa_2Cu_3O_{7.5}$. Fe doping was found to be more effective in suppressing J_c compared to Ni, Co and Ga.

In the present work we study the effect of Mn at the Cu site of YBCO on the temperature and field variations of ac susceptibility

4.2.1 Experimental:

Temperature variation of ac susceptibility at a constant ac field amplitude and field variation of ac susceptibility at 50 K were carried out using the setup described in the section 2.2.4 of Chapter 2. Temperature variation of ac susceptibility was carried out by a controlled temperature sweep of ~5-10 K per hour. Measurements were done at various ac field amplitudes of 0.2, 1.0, 5, 10, 20 and 30 Oe and in the temperature region of 10-110 K. Field variation of ac susceptibility was carried out at 50 K and 77 K to a maximum field of 30 and 80 Oe respectively. The coil used for

field variation of ac susceptibility at 77 K is made of 2800 turns of primary and two secondaries of 1250 turns each. The primary is wound coaxially on the top of two secondaries, which are connected in series opposition. The primary generates a field of 80 Oe at the maximum limiting energizing voltage of 3.5 V_{rms} in the WaveTek oscillator. All the ac susceptibility measurements were carried out at an operating frequency of 33 Hz. The inphase and the out of phase components of the signal from the secondary coil of the bridge were recorded through a dual phase – phase sensitive detector (PSD). The measured voltages were calibrated to obtain volume susceptibility as described in section 2.2.4 of Chapter 2.

4.2.2 Temperature variation of ac susceptibility:

Figures 4.1, 4.2 and 4.3 show the typical plots of temperature variation of ac susceptibility for YBa₂(Cu_{1-x}Mn_x)₃O_{7-δ} samples with $x = 0, 0.01, 0.015, 0.020, 0.025, 0.035$ and 0.050 , YBa₂(Cu_{0.075}Fe_{0.025})₃O_{7-δ}, YBa₂(Cu_{0.075}Ni_{0.025})₃O_{7-δ} and YBa₂(Cu_{0.075}Zn_{0.025})₃O_{7-δ} samples at energizing fields (H_{ac}) of 1, 10 and 30 Oe respectively. Figures 4.4, 4.5, 4.6 and 4.7 show the typical plots of temperature variation of ac susceptibility for varying energizing fields of 0.2, 1.0, 5.0, 10, 20 and 30 Oe for YBa₂Cu₃O_{7-δ}, YBa₂(Cu_{0.075}Mn_{0.025})₃O_{7-δ}, YBa₂(Cu_{0.075}Fe_{0.025})₃O_{7-δ} and YBa₂(Cu_{0.075}Ni_{0.025})₃O_{7-δ} samples. In the ac susceptibility measurements, the real part, χ' , is due to the inphase component corresponding to the dispersive magnetic response and the imaginary part χ'' is due to the out of phase component corresponding to the energy dissipation in the sample. The diamagnetic onset temperature, $T_{c(onset)}$ measured from the real part of susceptibility, χ' varies marginally around 91.5 K for varying Mn dopant concentrations whereas it falls to 88.2 K for Fe dopant, 84.5 K for Ni dopant and 78.6 K for Zn dopant. At minimum measured temperature (10 K) and (0.2 oe)field all the samples show a perfect diamagnetism, with χ' going to -1. Shielded grain fraction at 10 K, f_{g10} , estimated from the volume diamagnetism (Table 4.1), decreases from a value of 0.83 for the pure one to 0.60 for the 2.5 % Mn doped sample, while it was 0.72 and 0.80 for the 2.5 % Fe and Ni dopants respectively. Zn doped sample showed the least shielded grain fraction of 0.48.

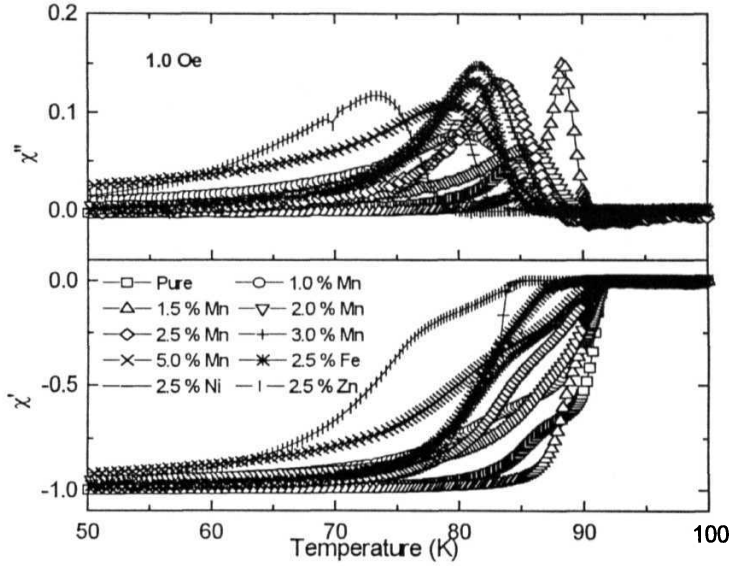


Figure 4.1 Plots of temperature variation of ac susceptibility for $\text{YBa}_2(\text{Cu}_{1-x}\text{Mn}_x)_3\text{O}_{7-\delta}$ samples with $x = 0, 0.01, 0.015, 0.020, 0.025, 0.035$ and 0.050 , $\text{YBa}_2(\text{Cu}_{0.075}\text{Fe}_{0.025})_3\text{O}_{7-\delta}$, $\text{YBa}_2(\text{Cu}_{0.075}\text{Ni}_{0.025})_3\text{O}_{7-\delta}$ and $\text{YBa}_2(\text{Cu}_{0.075}\text{Zn}_{0.025})_3\text{O}_{7-\delta}$ samples at an energizing field (H_{ac}) of 1 Oe.

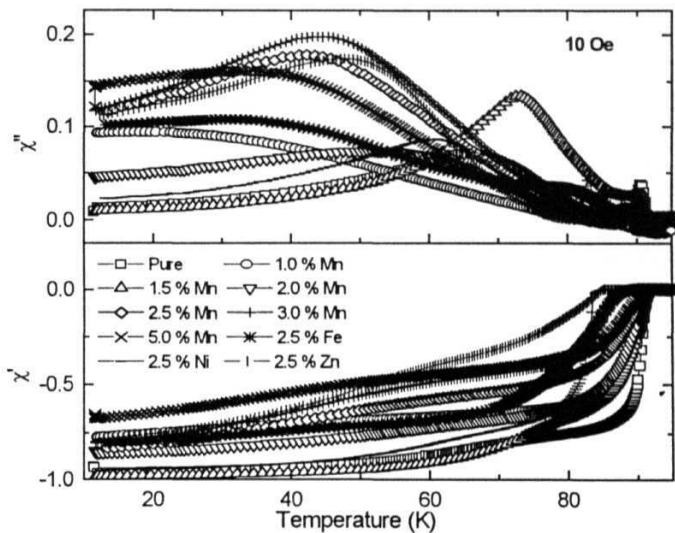


Figure 4.2 Plots of temperature variation of ac susceptibility for $\text{YBa}_2(\text{Cu}_{1-x}\text{Mn}_x)_3\text{O}_{7-\delta}$ samples with $x = 0, 0.01, 0.015, 0.020, 0.025, 0.035$ and 0.050 , $\text{YBa}_2(\text{Cu}_{0.075}\text{Fe}_{0.025})_3\text{O}_{7-\delta}$, $\text{YBa}_2(\text{Cu}_{0.075}\text{Ni}_{0.025})_3\text{O}_{7-\delta}$ and $\text{YBa}_2(\text{Cu}_{0.075}\text{Zn}_{0.025})_3\text{O}_{7-\delta}$ samples at an energizing field (H_{ac}) of 10 Oe.

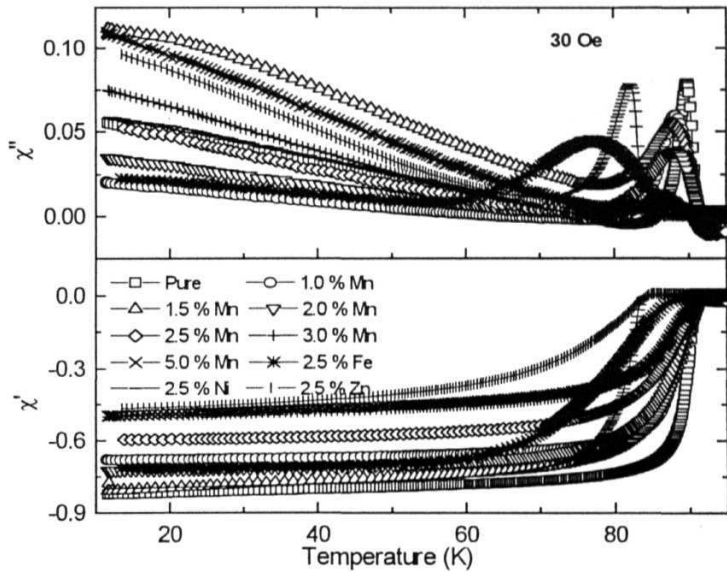


Figure 4.3 Plots of temperature variation of ac susceptibility for $\text{YBa}_2(\text{Cu}_{1-x}\text{Mn}_x)_3\text{O}_{7-\delta}$ samples with $x = 0, 0.01, 0.015, 0.020, 0.025, 0.035$ and 0.050 , $\text{YBa}_2(\text{Cu}_{0.075}\text{Fe}_{0.025})_3\text{O}_{7-\delta}$, $\text{YBa}_2(\text{Cu}_{0.075}\text{Ni}_{0.025})_3\text{O}_{7-\delta}$ and $\text{YBa}_2(\text{Cu}_{0.075}\text{Zn}_{0.025})_3\text{O}_{7-\delta}$ samples at an energizing field (H_{ac}) of 30 Oe.

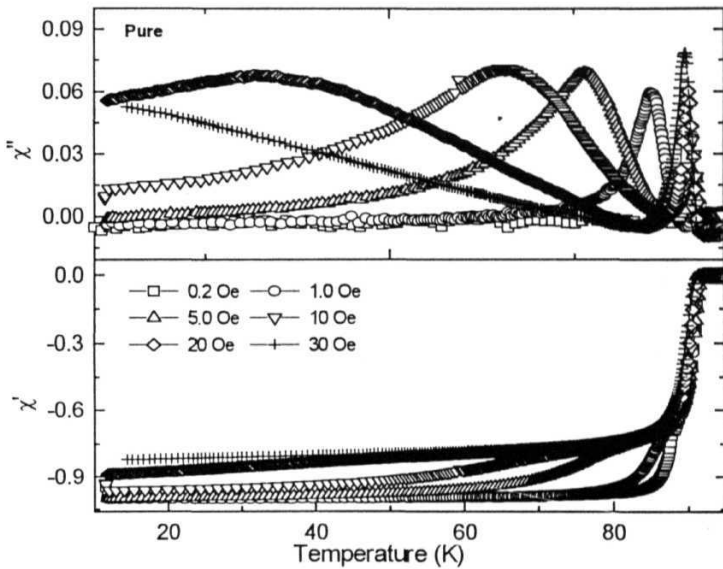


Figure 4.4 Plots of temperature variation of ac susceptibility for varying energizing fields of 0.2, 1.0, 5.0, 10, 20 and 30 Oe for $\text{YBa}_2\text{Cu}_3\text{O}_{7-x}$ sample.

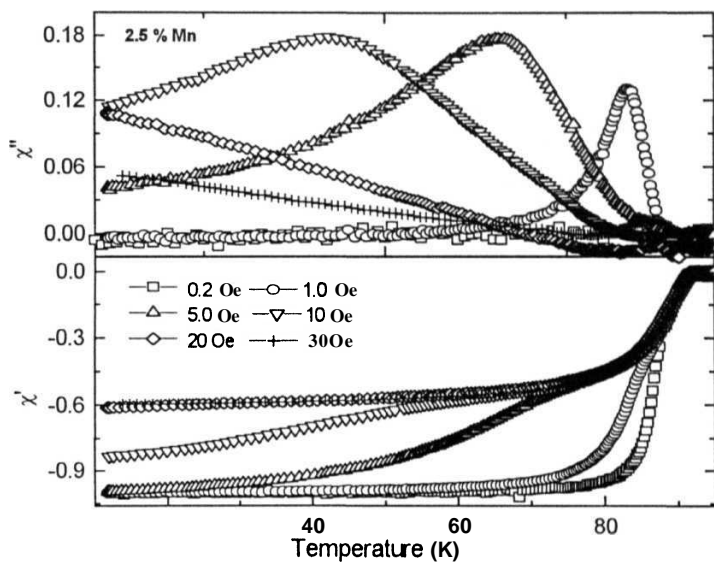


Figure 4.5 Plots of temperature variation of ac susceptibility for varying energizing fields of 0.2, 1.0, 5.0, 10, 20 and 30 Oe for sample.

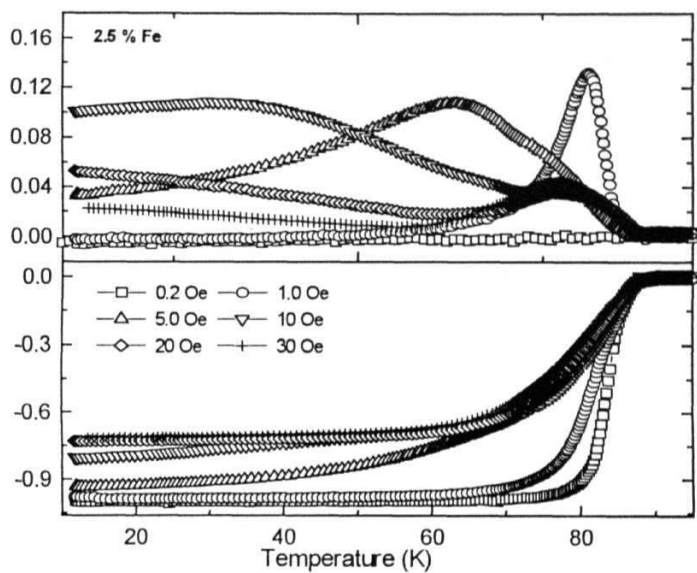


Figure 4.6 Plots of temperature variation of ac susceptibility for varying energizing fields of 0.2, 1.0, 5.0, 10, 20 and 30 Oe for $\text{YBa}_2(\text{Cu}_{0.075}\text{Fe}_{0.025})_3\text{O}_7$ sample.

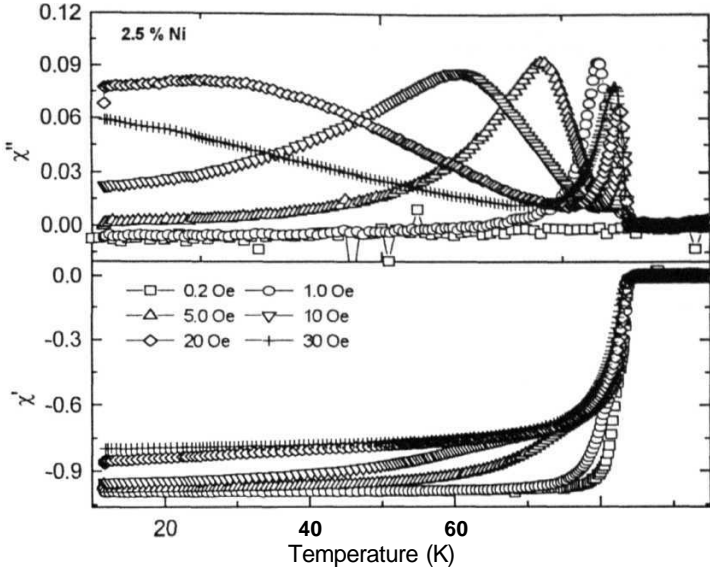


Figure 4.7 Plots of temperature variation of ac susceptibility for varying energizing fields of 0.2, 1.0, 5.0, 10, 20 and 30 Oe for $\text{YBa}_2(\text{Cu}_{0.075}\text{Ni}_{0.025})_3\text{O}_{7.5}$ sample.

$\chi''(T)$ shows a single strong peak at the lowest **experimental** field of 0.2 Oe, whereas at higher fields two peaks were observed at the temperatures T_{mg} and T_{mw} . The peak on the high temperature side (T_{mg}) is due to the granular response of the sample and is of lower magnitude and shows minimum field dependence. The second peak on the lower temperature side (T_{mw}) corresponds to the weak link response and is of higher magnitude and shifts towards lower temperature side with increasing field amplitude. This broad peak had been attributed to the energy losses in the coupling of the grains across the Josephson junctions [33]. For an applied field of 20 –30 Oe, the weak link peak shifts even below the minimum experimentally accessible lowest temperature of 10 K. The dissipation peaks represent **the full** penetration of the magnetic flux into **the** grains and weak links **of the sample** respectively, when the losses become maximum. As the temperature is **lowered** below T_c , the flux flow becomes more and more viscous, it till ultimately gets pinned at T_m . Variation of T_m with field coincides with the irreversibility line if there **is no**

extrinsic pinning present [34]. Thus the T_m Vs. H can roughly picture the flux pinning boundary for the sample in the temperature - field plane.

The critical current density J_c was estimated assuming Bean's critical state model magnitude, at a particular temperature T_m (where χ'' exhibits a peak) for a given field strength as,

$$J_c(T_m) = \frac{H_m}{d} \quad (4.32)$$

where H_m is the applied field amplitude. Here $d = a(1-a/3b)/2$, where a and b are the dimensions of the orthorhombic sample in the case of critical current density of the weak link J_{cw} whereas it represents the average grain size in the case of granular critical current density, J_{cg} .

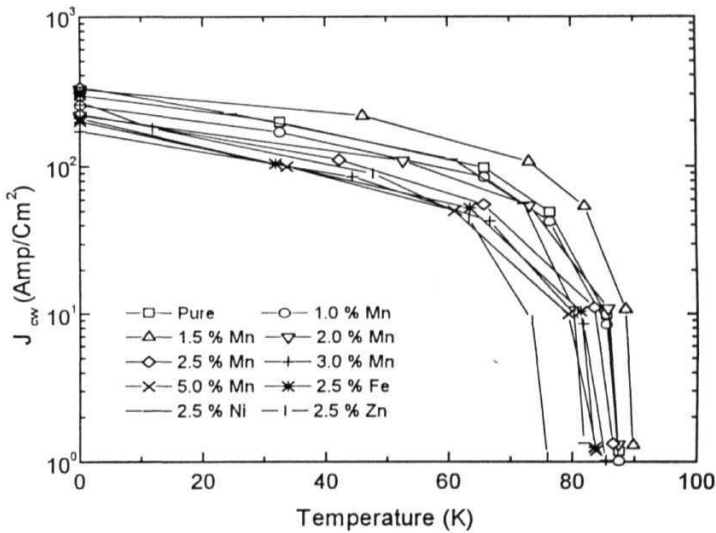


Figure 4.8 Plots of temperature variation of J_{cw} for $YBa_2(Cu_{1-x}Mn_x)_3O_{7-\delta}$ samples with $x = 0, 0.01, 0.015, 0.020, 0.025, 0.035$ and 0.050 , $YBa_2(Cu_{0.075}Fe_{0.025})_3O_{7-\delta}$, $YBa_2(Cu_{0.075}Ni_{0.025})_3O_{7-\delta}$ and $YBa_2(Cu_{0.075}Zn_{0.025})_3O_{7-\delta}$ samples.

Figure 4.8 shows the variation of J_{cw} with temperature which could be described well by a relation of the form

$$J_{cw}(T) = J_{cwo} (1 - T/T_{cj})^{n_j} \quad (4.33)$$

where J_{cwo} and n_j are constants and T_{cj} is the critical temperature of the junction marking the onset of grain coherence [35]. Table 4.1 shows the parameters obtained for different samples. The exponent, n_j , varies close to one which is typical for a SIS (Superconducting-Insulator-Superconducting) type coupling of grains [36]. n_j assumes a value of 2 for SNS (Superconducting-Normal-Superconducting) type of coupling of grains. This could be because of the low density (*i.e.* large porosity) of the samples, also given in the Table 4.1, which are far below the theoretical density of 6.37 gm/cm³ of YBCO.

Table 4.1. Table of the fit parameters of the temperature variation of weak link critical current density, J_{cwo} , T_{cj} and n_j , temperature at which a granular critical current density (J_{cg}) of 2.4×10^4 A/m² was observed, shielded grain fraction at 30 Oe and 10 K, (f_{g10}), apparent density and measured grain size from SEM for all the samples studied.

Sample (doping in %)	J_{cwo} A/cm ²	T_{cj} K	n_j	Temp (K) at which J_{cg} is 2.4×10^4 A/m ²	f_{g10} (Exptl.)	Density gm/cm ³	Grain Size (μ m)
Mn							
0	285.43	86.39	0.77	89.79	0.83	4.72	7.75
1	105.38	85.98	0.87	88.19	0.68	4.09	8.25
1.5	370.61	89.12	0.74	87.82	0.82	4.79	9.42
2	224.78	87.51	0.78	88.07	0.73	4.78	9.65
2.5	206.41	87.00	0.93	86.81	0.60	4.38	15.18
3.5	167.94	85.52	0.92	86.77	0.50	4.45	11.20
5	161.24	84.02	0.92	86.75	0.50	4.04	11.33
Fe							
2.5	149.88	83.68	0.74	77.18	0.72	4.90	13.28
Ni							
2.5	291.40	80.78	0.71	82.19	0.80	5.06	9.45
Zn							
2.5	207.87	75.98	0.86	82.9	0.48	3.72	9.50

It can be seen from a close observation of the above table that the 1.0 % Mn doped sample is highly porous with a density of 4.09 gm/cm³, whereas the 1.5 % Mn doped sample had a better density of 4.79 gm/cm³. The relatively porous 1 % Mn doped sample has the lower f_{g10} compared to the pure and 1.5 % Mn doped samples. Similarly, 1 % Mn doped sample showed the least weak link J_{cwo} of 105 A/cm² while the 1.5 % Mn doped one showed the highest J_{cwo} of 370 A/cm². These jumps in J_{cwo} can be rationalized in terms of the microstructural porosity for the 1 % Mn and the

better density. This difference could be because of some minor unnoticed variations in the processing details that influence the microstructure and the weak link properties drastically. However, the J_{cwo} values for pure, 2.0, 2.5, 3.5 and 5.0 % Mn decreases steadily from 285 A/cm² for pure sample to 161 A/cm² for the 5.0 % Mn doped sample. The weak link J_{cwo} of Fe, Ni and Zn doped samples are 149 A/cm², 291 A/cm² and 207 A/cm² respectively. Dopants at the Cu(I) sites, Mn and Fe, reduce the weak link critical current density more than the Cu(II) site dopants, Ni and Zn. Among the Cu(I) site dopants, effect of Mn is minimal, compared to Fe, in suppressing the weak link J_c .

The granular critical current density J_{cg} was calculated from the $H_m(T_m)$ (corresponding to x'' peak value) of the grains, using the average grain size calculated from the scanning electron micrograph for the above samples. The experimental fields of 0.2 - 30 Oe are too low to probe the grain property. Hence the variation of J_{cg} with field is too scattered near T_c to derive any meaningful functional dependence of J_{cg} with temperature. Hence we here compare the temperatures at which same value of $J_{cg}=2.4 \times 10^4$ A/cm² is observed for different compositions. The J_{cg} of the pure sample was 2.4×10^4 A/cm² at 89.79 K and the J_{cg} for 2.5 % doped sample was 2.4×10^4 A/cm² at 86.81 K. Fe and Ni doped samples showed the same J_{cg} at 77.18 and 82.19 K respectively.

4.2.3 Temperature Dependent ac Loss :

The total ac loss per unit volume of the superconductor is given as

$$W = \frac{1}{2} \omega \chi'' \mu_0 H_a^2 \quad (4.34)$$

where ω is the angular frequency and μ_0 is the permeability of free space. Figure 4.9 shows the temperature variation of ac losses due to weak links, plotted against the reduced temperature of $(1-T/T_c)$, where the $T_{c,d}$ values were taken from the $J_{cw}(T)$ fit. The weak link losses were fitted to a power relation of the form

$$W = W(0)(1 - T/T_c)^m \quad (4.35)$$

where $W(0)$ is the loss at zero Kelvin and m is the exponent that assumes an averaged value of 1.96. The parameters obtained from the power law fit are tabulated in Table 4.2. The amplitudes of ac fields studied are too low, that the calculated granular losses are scattered closer to T_c , to derive any functional dependence for granular losses with temperature or reduced temperature.

Table 4.2. Fit parameters for temperature variation of ac losses at H_m to the power relation (Eq. 4.35) for the $YBa_2(Cu_{1-x}Mn_x)_3O_{7.5}$ samples with x values 0, 0.01, 0.015, 0.020, 0.025, 0.035 and 0.050, $YBa_2(Cu_{0.075}Fe_{0.025})_3O_{7.5}$, $YBa_2(Cu_{0.075}Ni_{0.025})_3O_{7.5}$ and $YBa_2(Cu_{0.075}Zn_{0.025})_3O_{7.5}$ samples

Sample (doping in %)	$W_{fit}(0)$	n_{fit}
Mn		
0	96.93	1.76
1.0	24.85	2.05
1.5	222.33	1.51
2.0	63.81	1.95
2.5	114.58	2.21
3.5	147.78	2.22
5.0	78.08	2.29
Fe		
2.5	39.63	1.82
Ni		
2.5	96.93	1.82
Zn		
2.5	166.28	2.43

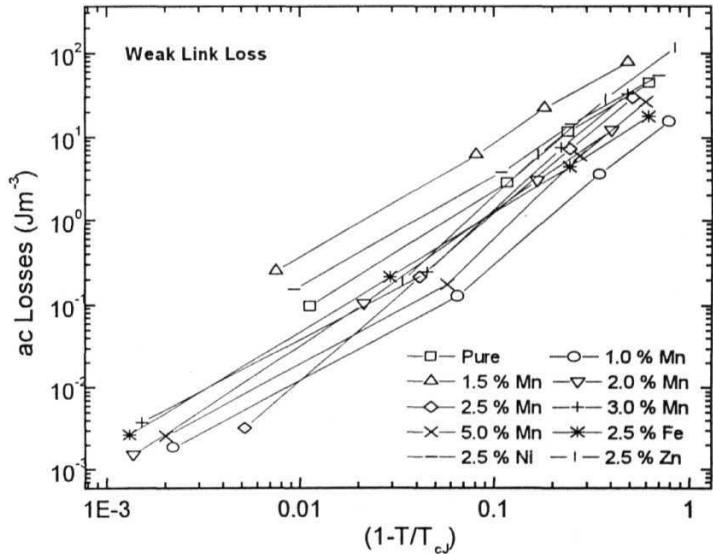


Figure 4.9 Temperature variation of ac loss for $YBa_2(Cu_{1-x}Mn_x)_3O_{7.5}$ samples with $x = 0, 0.01, 0.015, 0.020, 0.025, 0.035$ and 0.050 , $YBa_2(Cu_{0.075}Fe_{0.025})_3O_{7.5}$, $YBa_2(Cu_{0.075}Ni_{0.025})_3O_{7.5}$ and $YBa_2(Cu_{0.075}Zn_{0.025})_3O_{7.5}$ samples.

On Mn doping T_c does not vary much, but $J_{cw}(T)$ and J_{cwo} decrease with increasing Mn dopant. Hence the Mn dopant at the Cu(I) site does not affect the mechanism responsible for superconductivity directly nevertheless alters the magnetic properties by weakening of energy barriers at the pinning site[32].

4.2.4 Field variation of ac susceptibility:

Figure 4.10 shows the plots of field variation of ac susceptibility for $YBa_2(Cu_{1-x}Mn_x)_3O_{7-\delta}$ samples with $x = 0, 0.01, 0.015, 0.020, 0.025, 0.035$ and 0.050 , $YBa_2(Cu_{0.075}Fe_{0.025})_3O_{7-\delta}$, $YBa_2(Cu_{0.075}Ni_{0.025})_3O_{7-\delta}$ and $YBa_2(Cu_{0.075}Zn_{0.025})_3O_{7-\delta}$ samples at 50 K and Figure 4.11 shows the same at 77 K. At 50 K, for a minimum energizing field all the samples show perfect diamagnetism (*i.e* $tf = -1$) whereas at 77 K, pure and low dopant samples ($< 2\%$ of Mn) alone showed closer to $tf = -1$ while others show a positive deviation from -1 . This is because of the non superconducting fraction, f_n , of the weak link region at 77 K. Also the transitions at 50 K are quite sharp compared to those at 77 K.

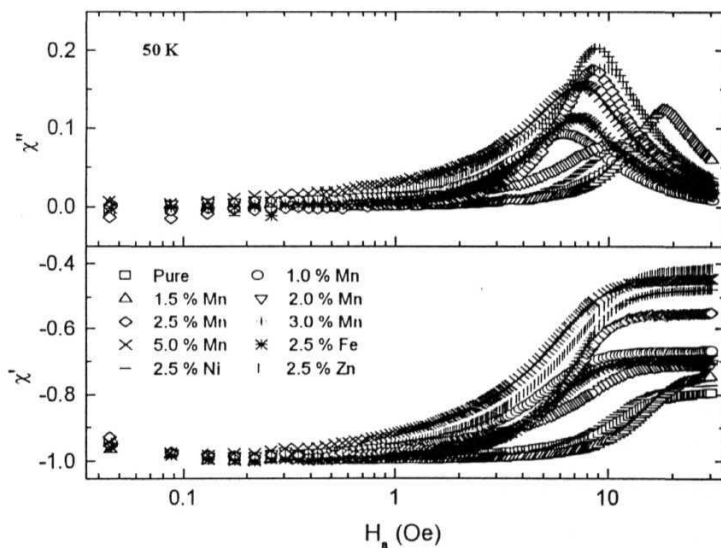


Figure 4.10 Plots of field variation of ac susceptibility for $YBa_2(Cu_{1-x}Mn_x)_3O_{7-\delta}$ samples with $x = 0, 0.01, 0.015, 0.020, 0.025,$

0.035 and 0.050, $\text{YBa}_2(\text{Cu}_{0.075}\text{Fe}_{0.025})_3\text{O}_{7-\delta}$, $\text{YBa}_2(\text{Cu}_{0.075}\text{Ni}_{0.025})_3\text{O}_{7-\delta}$ and $\text{YBa}_2(\text{Cu}_{0.075}\text{Zn}_{0.025})_3\text{O}_{7-\delta}$ samples at 50 K.

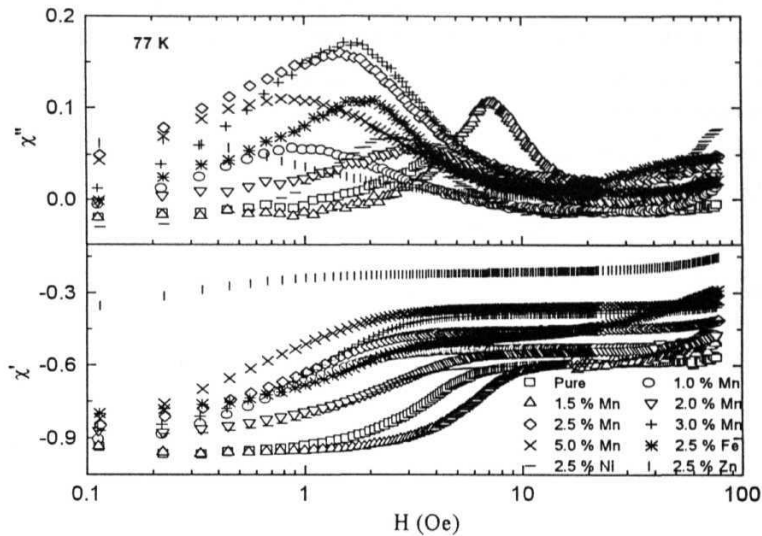


Figure 4.11 Plots of field variation of ac susceptibility for $\text{YBa}_2(\text{Cu}_{1-x}\text{Mn}_x)_3\text{O}_{7-\delta}$ samples with $x = 0, 0.01, 0.015, 0.020, 0.025, 0.035$ and 0.050 , $\text{YBa}_2(\text{Cu}_{0.075}\text{Fe}_{0.025})_3\text{O}_{7-\delta}$, $\text{YBa}_2(\text{Cu}_{0.075}\text{Ni}_{0.025})_3\text{O}_{7-\delta}$ and $\text{YBa}_2(\text{Cu}_{0.075}\text{Zn}_{0.025})_3\text{O}_{7-\delta}$ samples at 77 K.

4.2.4.1 Kims Model Simulation:

The irreversible magnetization of superconducting materials had been successfully explained by the critical state models, in which a variety of field dependence for J_c had been used to describe the local field inside a superconductor. $J_c(H)$ proposed by Kim *et al.* [14] is widely used in describing the weak link magnetization of ceramic superconductors [10,11]. In Kim model (Eqn. 4.6), the full penetration field H_p is defined as[18],

$$H_p = \left((1 + p^2)^{1/2} - 1 \right) H_0 \quad (4.36)$$

where,

$$p = \left(\frac{1}{H_0} \right) (2ka)^{\frac{1}{2}} \quad (4.37)$$

p is related to the inhomogeneities in the current path.

Using the numerical method, described in section 4.1.2, we have simulated the real and imaginary parts of susceptibility at 50 K and 77 K, with H_p , p and f_g as fit parameters. In the case of 77 K susceptibility data, even at the minimum applied field volume susceptibility is not -1. The volume susceptibility value at the minimum applied field is taken as the non superconducting volume fraction, f_n . Then, volume susceptibility due to the grains and weak links can be separated as,

$$X = f_g \chi_g + (1 - f_g - f_n) \chi_w \quad (4.38)$$

The fit parameters and the J_{cw} calculated from the H_p for 50 K and 77 K data are tabulated in Table 4.3 and 4.4 respectively.

Table 4.3 Fit parameters obtained from the Kim's model simulation for the 50 K data. H_p is the full penetration field, p is a constant related to the inhomogeneity in current path, f_{g50} is the effective grain fraction of the grains and the J_{cw} is the weak link critical current density.

Sample (doping in %)	H_p Amp/cm	p	f_{g50}	J_{cw} Amp/cm ²
Mn				
0	15.43	5.11	0.78	152.2
1.0	5.84	2.61	0.67	49.5
1.5	20.81	15.18	0.71	224.8
2.0	8.26	12.11	0.69	90.2
2.5	8.76	25.71	0.54	97.7
3.5	8.74	47.14	0.47	74.8
5.0	6.19	1.38	0.43	62.1
Fe				
2.5	6.47	26.95	0.69	67.9
Ni				
2.5	13.49	10.30	0.76	151.2
Zn				
2.5	8.57	2.44	0.40	77.2

From the full penetration field, H_p , weak link critical current density, J_{cw} , is calculated as,

$$J_{cw} = \frac{2H_p}{a \left(1 + \frac{a}{3b} \right)} \quad (4.39)$$

where a and b are the sample dimensions. The J_{cw} values thus calculated agree well with those obtained in the temperature variation of ac susceptibility.

Figure 4.12a and 4.12b show the typical Kim's model simulations of the real and imaginary parts of field variation of ac susceptibility for all the samples studied, represented at 50 K. The J_{cw} , the full penetration field (H_p), and the p shows similar trend of variation with dopant concentration where the 1.5 % Mn doped sample showed better intergranular properties while the one with 1.0 % exhibits inferior properties which can be correlated to the relative porosity in them. However, further increase in Mn concentration suppressed the magnetic properties.

Table 4.4 Fit parameters obtained from the Kim's model simulation for the 77 K data. H_p is the full penetration field, p is a constant related to the inhomogeneity in current path, f_{g77} is the effective grain fraction of the grains, f_n is the non superconducting fraction at 77 K and the J_{cw} is the weak link critical current density.

Sample (doping in %)	H_p Oe	P	f_{g77}	f_n	J_{cw} Amp/cm ²
Mn					
0	4.64	9.78	0.59	0.04	45.79
1.0	1.17	0.67	0.53	0.09	9.90
1.5	7.46	5.56	0.59	0.04	80.53
2.0	3.20	1.64	0.54	0.13	34.97
2.5	1.47	1.25	0.45	0.16	16.35
3.5	1.65	1.44	0.38	0.14	14.09
5.0	1.03	0.09	0.35	0.18	10.28
Fe					
2.5	1.99	0.01	0.46	0.20	20.84
Ni					
2.5	2.79	4.44	0.60	0.12	31.24
Zn					
2.5	1.03	0.09	0.35	0.65	9.23

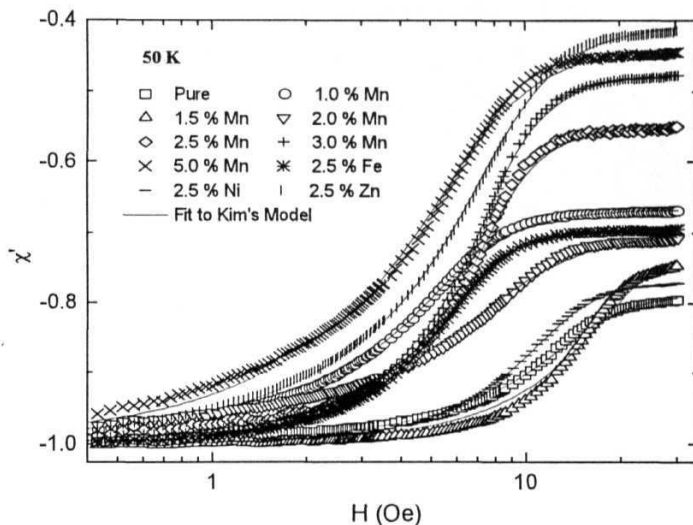


Figure 4.12a Typical Kim's model simulations of the real and imaginary part of field variation of ac susceptibility for the $\text{YBa}_2(\text{Cu}_{1-x}\text{Mn}_x)_3\text{O}_{7-\delta}$ samples with $x = 0, 0.01, 0.015, 0.020, 0.025, 0.035$ and 0.050 , $\text{YBa}_2(\text{Cu}_{0.075}\text{Fe}_{0.025})_3\text{O}_{7-\delta}$, $\text{YBa}_2(\text{Cu}_{0.075}\text{Ni}_{0.025})_3\text{O}_{7-\delta}$ and $\text{YBa}_2(\text{Cu}_{0.075}\text{Zn}_{0.025})_3\text{O}_{7-\delta}$ samples, represented at 50 K.

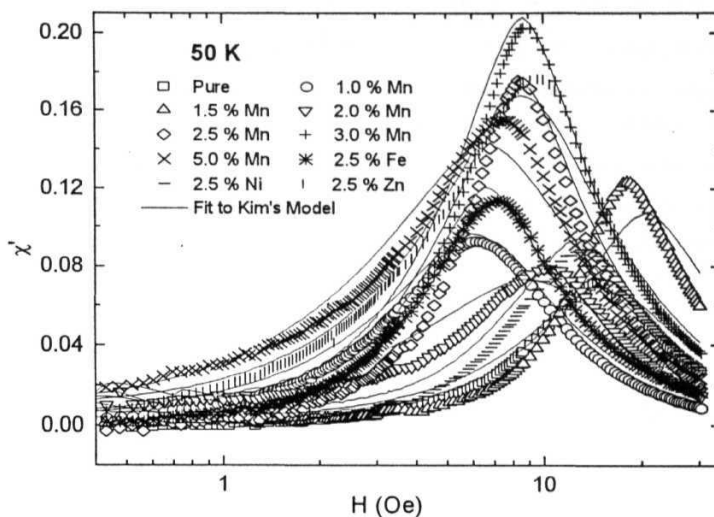


Figure 4.12b Typical Kim's model simulations of the imaginary part of field variation of ac susceptibility for the $\text{YBa}_2(\text{Cu}_{1-x}\text{Mn}_x)_3\text{O}_{7-\delta}$ samples with $x = 0, 0.01, 0.015, 0.020, 0.025, 0.035$ and 0.050 , $\text{YBa}_2(\text{Cu}_{0.075}\text{Fe}_{0.025})_3\text{O}_{7-\delta}$, $\text{YBa}_2(\text{Cu}_{0.075}\text{Ni}_{0.025})_3\text{O}_{7-\delta}$ and $\text{YBa}_2(\text{Cu}_{0.075}\text{Zn}_{0.025})_3\text{O}_{7-\delta}$ samples, represented at 50 K.

4.3 DC MAGNETIC PROPERTIES :

DC magnetization studies on high T_c superconductors has **been of much interest** for the material information that can be obtained from it. In magnetization measurements, as the field is increased, more and more vortices are **generated and** the vortex density increases within the sample. The granular nature of **the** high temperature superconductors (HTSC) causes two kinds of vortices namely Josephson or weak link vortices across the intergranular region and Abrikosov (or granular) vortices within the grain [26]. Magnetization measurements give **a direct** correlation with the vortex dynamics such as vortex pinning, vortex-vortex interaction *etc.* with temperature and field [37]. As the ceramic superconductors are of highly granular nature, the effective usefulness of the material is determined by properties of the weak links and the grains together. While the ac measurements **have been**

widely used to study the weak link behavior, DC magnetization studies are used to probe the grain property. On melt processed (RE)Ba₂Cu₃O_{7-δ} samples, Murakami had carried out an extensive study of critical current density and flux pinning force [38].

Doping at the copper site has been of prime importance to understand the mechanism of superconductivity and to improve the magnetic properties such as flux pinning etc. Zheng et al [32] have studied the Co and Zn doped YBa₂Cu₃O_{7-δ} and reported an increase in the anisotropy of properties on doping. Jirsa et al [39] have calculated the penetration depth from the irreversible magnetization region on Mg doped YBa₂Cu₃O_{7-δ} granular samples.

4.3.1 Experimental:

DC Magnetization measurements were carried out using a *Quantum Design* SQUID magnetometer at TIFR, Mumbai. SQUID magnetometers are very versatile with a wide spectrum of temperature and field over which the magnetic properties of the materials could be studied. Isothermal DC Magnetization measurements on the parallelepiped samples of size ~ 2 mm x 2 mm x 1.2 mm were carried out upto a maximum field of 5 T, at temperatures of 5, 50 and 77 K.

4.3.2 Results and Discussion:

Figures 4.13, 4.14 and 4.15 show the magnetization curves for the YBa₂(Cu_{1-x}Mn_x)₃O_{7-δ} samples with x taking values 0, 0.01, 0.015, 0.020, 0.025, 0.035 and 0.050, YBa₂(Cu_{0.075}Fe_{0.025})₃O_{7-δ}, YBa₂(Cu_{0.075}Ni_{0.025})₃O_{7-δ} and YBa₂(Cu_{0.075}Zn_{0.025})₃O_{7-δ} samples at 5, 50 and 77 K respectively. Magnetization curves were initially recorded as the field is increased from the zero field cooled condition to a maximum field of 5 T and subsequently field reversed cycles of magnetization curves were also recorded reversing the field from H_{max} to zero. The negative peak, H_{c1g} , observed on virgin magnetization is taken as *indicative lower critical field* of the grains. This was normalized with the grain size and plotted In Figure 4.16. At 77 K normalized H_{c1g} falls **monotonically** with the increase of Mn concentration whereas at 50 K and 5 K it shows an increase in normalized H_{c1g} at

2 % Mn concentration and continues to drop with further addition of Mn.

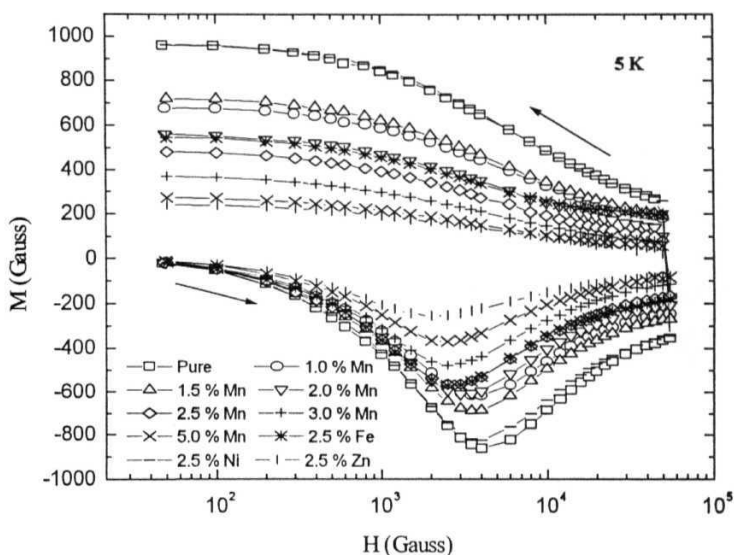


Figure 4.13 Magnetization curve for the $\text{YBa}_2(\text{Cu}_{1-x}\text{Mn}_x)_3\text{O}_{7.5}$ samples with x taking values 0, 0.01, 0.015, 0.020, 0.025, 0.035 and 0.050, $\text{YBa}_2(\text{Cu}_{0.075}\text{Fe}_{0.025})_3\text{O}_{7.5}$, $\text{YBa}_2(\text{Cu}_{0.075}\text{Ni}_{0.025})_3\text{O}_{7.5}$ and $\text{YBa}_2(\text{Cu}_{0.075}\text{Zn}_{0.025})_3\text{O}_{7.5}$ samples at 5 K.

From the remnant magnetization, M_{rem} , (i.e. magnetization at zero field on field cooling) the zero field critical current density $J_{\text{cg}}(0)$ was calculated as $J_{\text{cg}}(0) = 20 M_{\text{rem}} / 4\pi d$, where d is the average grain size calculated from the Scanning Electron Micrograph (SEM). $J_{\text{cg}}(0)$ thus calculated are tabulated in Table 4.4. $J_{\text{cg}}(0)$ at 5 K, 50 K and 77 K are of the order of 10^6 , 10^5 and 10^4 Amp/cm² respectively. It falls monotonically with the substitution of Mn upto 2.5 % and shows saturation there after for the samples which also showed impurity lines of intensity ~ 5 % at around 28 and 30° of 2θ values in XRD pattern. $J_{\text{cg}}(0)$ suppression due to doping is the lowest for Ni substituted samples compared to the Fe, Mn and Zn. However, the rate of fall of $J_{\text{cg}}(0)$ with temperature for Mn doped sample is lower than that of 2.5 % of Ni, Fe and Zn at substituted samples. Figure 4.17 brings out the effect of different dopants and temperature on $J_{\text{cg}}(0)$ of the YBCO system.

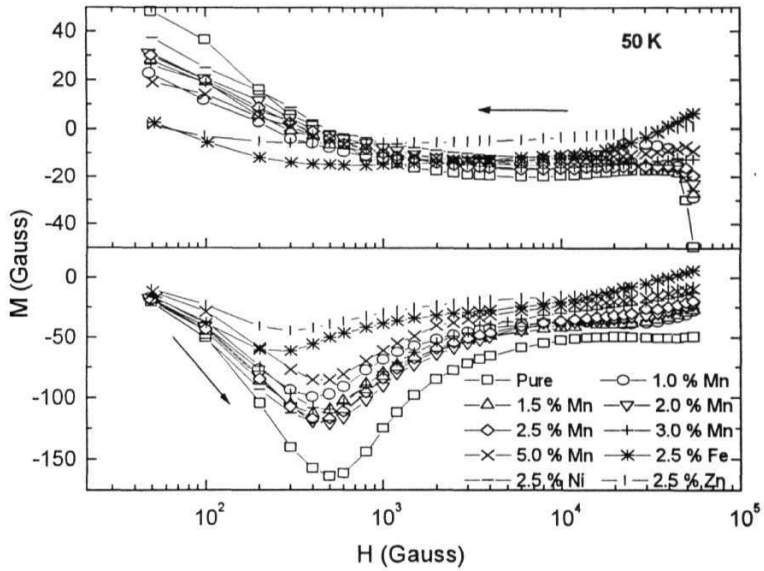


Figure 4.14 Magnetization curve for the $\text{YBa}_2(\text{Cu}_{1-x}\text{Mn}_x)_3\text{O}_{7.5}$ samples with x taking values 0, 0.01, 0.015, 0.020, 0.025, 0.035 and 0.050, $\text{YBa}_2(\text{Cu}_{0.075}\text{Fe}_{0.025})_3\text{O}_{7.5}$, $\text{YBa}_2(\text{Cu}_{0.075}\text{Ni}_{0.025})_3\text{O}_{7.5}$ and $\text{YBa}_2(\text{Cu}_{0.075}\text{Zn}_{0.025})_3\text{O}_{7.5}$ samples at 50 K.

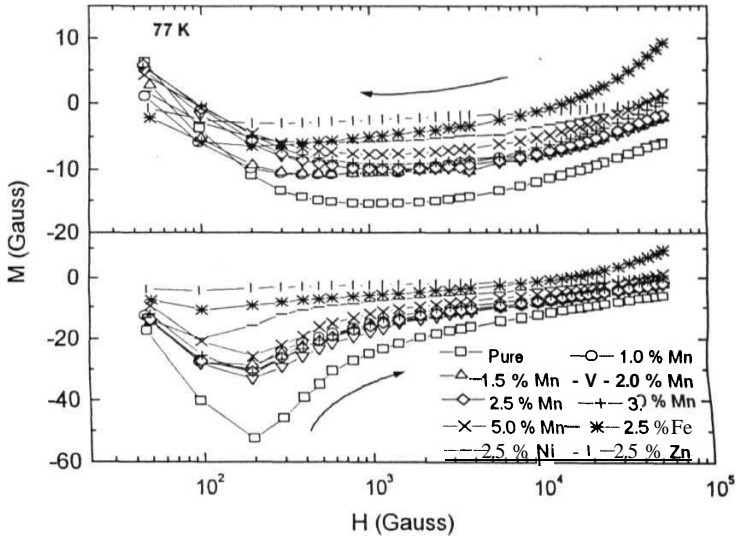


Figure 4.15 Magnetization curve for the $\text{YBa}_2(\text{Cu}_{1-x}\text{Mn}_x)_3\text{O}_{7-\delta}$ samples with x taking values 0, 0.01, 0.015, 0.020, 0.025, 0.035 and 0.050, $\text{YBa}_2(\text{Cu}_{0.075}\text{Fe}_{0.025})_3\text{O}_{7-\delta}$, $\text{YBa}_2(\text{Cu}_{0.075}\text{Ni}_{0.025})_3\text{O}_{7-\delta}$ and $\text{YBa}_2(\text{Cu}_{0.075}\text{Zn}_{0.025})_3\text{O}_{7-\delta}$ samples at 77 K.

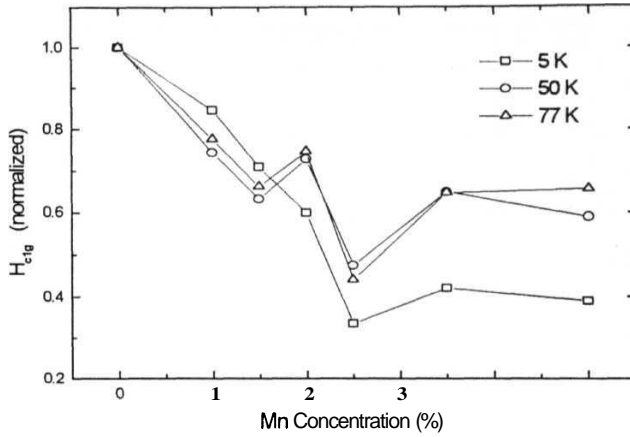


Figure 4.16 Indicative lower critical field, H_{c1g}^* , normalized to the grain size, for the $YBa_2(Cu_{1-x}Mn_x)_3O_{7-\delta}$ samples with x taking values 0, 0.01, 0.015, 0.020, 0.025, 0.035 and 0.050, $YBa_2(Cu_{0.075}Fe_{0.025})_3O_{7-\delta}$, $YBa_2(Cu_{0.075}Ni_{0.025})_3O_{7-\delta}$ and $YBa_2(Cu_{0.075}Zn_{0.025})_3O_{7-\delta}$ samples at 77 K.

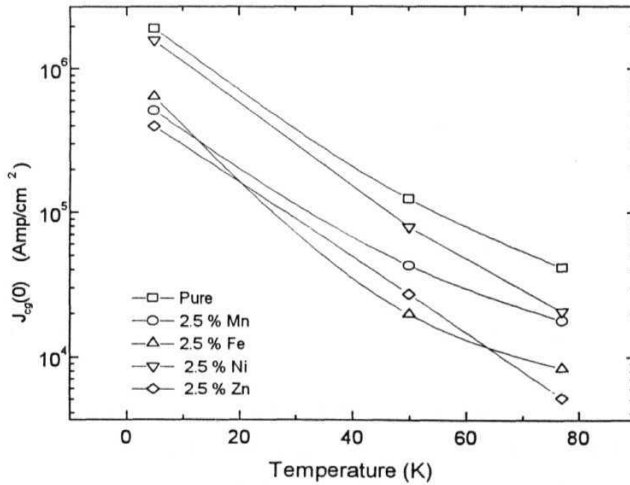


Figure 17 Variation of $J_{c0}(0)$ for the pure and 2.5 % Mn, Fe, Ni and Zn doped $YBa_2Cu_3O_{7-\delta}$ superconductors at 5, 50 and 77 K.

Table 4.S. Table showing the zero field critical current density, $J_{cg}(0)$, calculated from the M_{rem} at 5, 50 and 77 K.

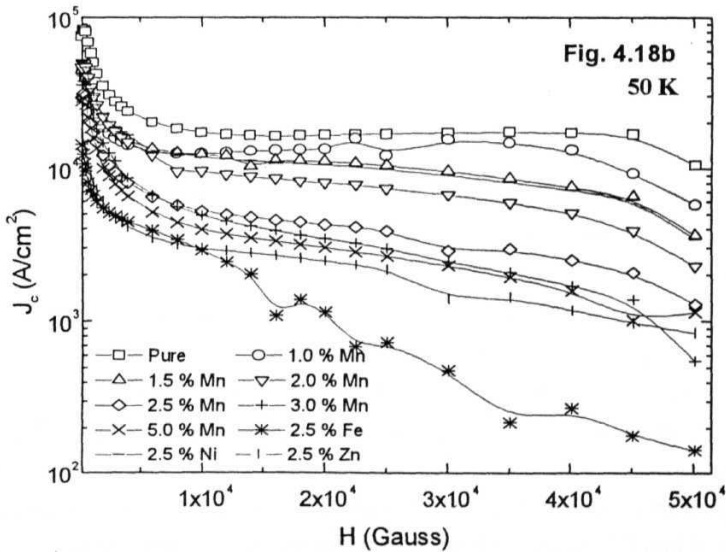
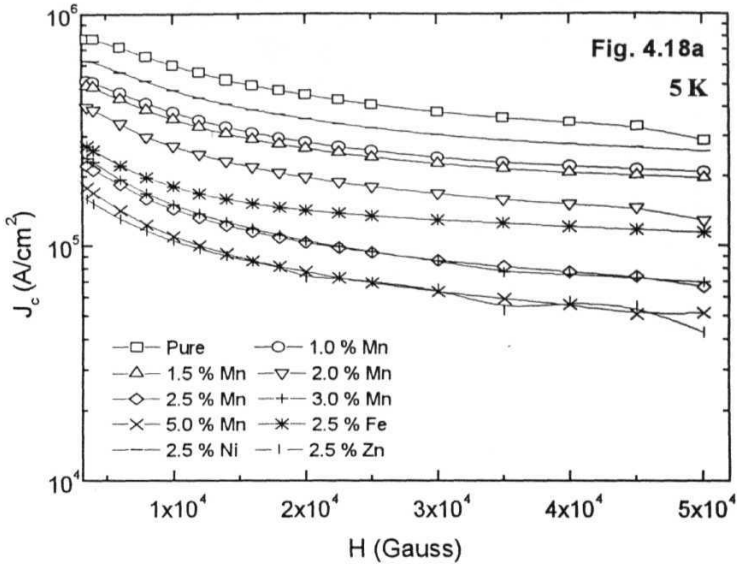
Sample	$J_{cg}(0)$ at 5 K	$J_{cg}(0)$ at 50 K	$J_{cg}(0)$ at 77 K
Mn			
0.0	1.938×10^6	1.241×10^5	4.145×10^4
1.0	1.282×10^6	6.281×10^4	2.602×10^4
1.5	1.188×10^6	6.163×10^4	2.602×10^4
2.0	9.102×10^5	6.653×10^4	2.730×10^4
2.5	5.070×10^5	4.280×10^4	1.779×10^4
3.5	5.184×10^5	5.085×10^4	2.065×10^4
5.0	3.795×10^5	3.859×10^4	1.625×10^4
Fe			
2.5	6.330×10^5	1.975×10^4	8.328×10^3
Ni			
2.5	1.583×10^6	7.866×10^4	2.074×10^4
Zn			
2.5	3.954×10^5	2.721×10^4	5.176×10^3

Field dependence of critical current $J_{cg}(H)$ was calculated from the magnetization curve above H_{c1g} as

$$J_{cg}(H) = \frac{10\Delta M}{4\pi d} \quad (4.40)$$

where ΔM is the width of the magnetization loop at that field and d is the average grain size. Figures 4.18a, b and c show the field variation of J_{cg} at temperatures 5 K, 50 K and 77 K. The $J_{cg}(H)$ at 5 K and 50 K were quite field independent compared to $J_{cg}(H)$ at 77 K. At all temperatures J_{cg} decreases systematically with Mn addition upto a concentration of 2.5 % and shows a saturation in suppression beyond this concentration. This is in contrast with the variation of weak link critical current density, J_{cwl} , with Mn doping, where the 1.5 % Mn doped sample showed the superior magnetic properties. At 5 K, the J_{cg} for the 2.5 % Ni doped sample falls between the J_{cg} of pure and 1.0 % Mn doped sample, at 50 K it falls between that of 2.0 and 2.5 % Mn doped sample. At 77 K the J_{cg} of the 2.5 % Ni falls well below even the 5 % Mn doped sample. However, the J_{cg} of the 2.5 % Ni doped sample is the higher than that of Fe and Zn doped one at all the temperatures studied, 5, 50 and 77 K. At 50 K, the J_{cg} of the 2.5 % Zn doped sample is better than that of the Fe doped sample and is comparable with that of 5 % Mn doped sample whereas at 5 K and 77 K it falls below all other samples. The pronounced temperature dependence of J_{cg} of the Fe, Ni and Zn doped samples is in contrast with the poor temperature dependence of J_{cg} of Mn doped sample at the same dopant concentration of 2.5 %. This suggests that

magnetic Mn at the Cu(I) chain site reduces the temperature dependence of J_{cg} compared to other 3d impurities at either sites.



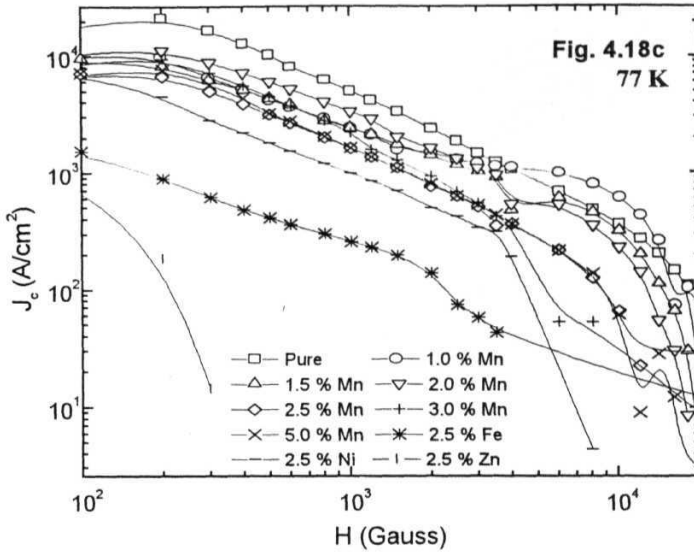
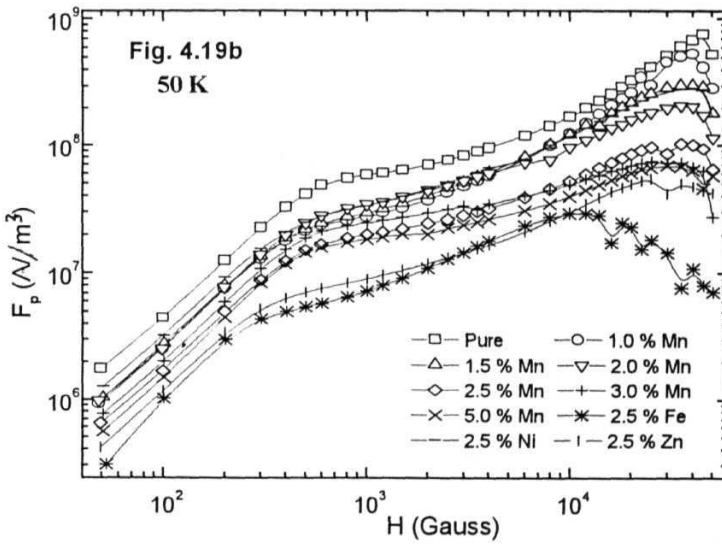
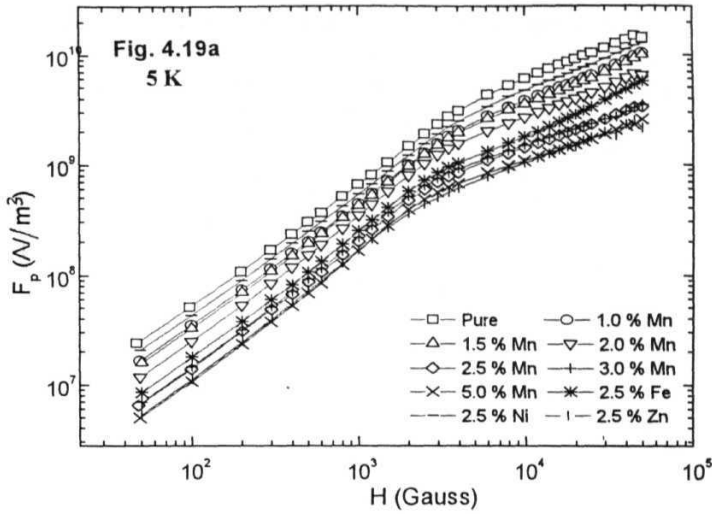


Figure 4.18 Plots of field variation of J_{c0} for the $\text{YBa}_2(\text{Cu}_{1-x}\text{Mn}_x)_3\text{O}_{7.8}$ samples with x taking values 0, 0.01, 0.015, 0.020, 0.025, 0.035 and 0.050, $\text{YBa}_2(\text{Cu}_{0.075}\text{Fe}_{0.025})_3\text{O}_{7.8}$, $\text{YBa}_2(\text{Cu}_{0.075}\text{Ni}_{0.025})_3\text{O}_{7.8}$ and $\text{YBa}_2(\text{Cu}_{0.075}\text{Zn}_{0.025})_3\text{O}_{7.8}$ samples at (a) 5 K, (b) 50 K and (c) 77 K.

The flux pinning force calculated as $F_p = J_{c0}B$ for the $\text{YBa}_2(\text{Cu}_{1-x}\text{Mn}_x)_3\text{O}_{7.8}$ samples with x taking values 0, 0.01, 0.015, 0.020, 0.025, 0.035 and 0.050, $\text{YBa}_2(\text{Cu}_{0.075}\text{Fe}_{0.025})_3\text{O}_{7.8}$, $\text{YBa}_2(\text{Cu}_{0.075}\text{Ni}_{0.025})_3\text{O}_{7.8}$ and $\text{YBa}_2(\text{Cu}_{0.075}\text{Zn}_{0.025})_3\text{O}_{7.8}$ samples are plotted in Figures 4.19a, b and c for temperatures 5, 50 and 17 K respectively. At 5 K, the flux pinning force plotted against field in a log-log scale showed a double slope behavior which is an indication of the dual exponent **power** relation with the field. Whereas at 50 K a triple slope behavior is observed. **At lower** fields (< 500 Oe) the average slope was 1.14 and 1.47 for 5 K and 50 K respectively and increased marginally with doping. At higher fields (> 6000 Oe) it was 0.59 and 0.77 for 5 K and 50 K respectively. At 5 K, F_p decreased with increasing Mn doping whereas at 50 K and 77 K, F_p increased with increasing Mn doping upto 2% and decreased on further doping. In the absence of extrinsic flux pinning, the flux pinning force, F_p , can be related to the condensational pinning energy [32] and is found to decrease with doping at 5 K. However, at 50 K and 77 K, assuming the absence of



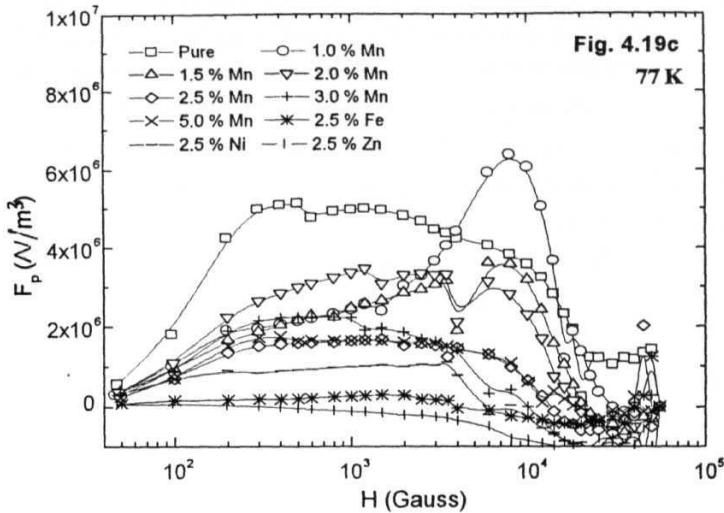


Figure 4.19 Plots of field variation of flux pinning force, F_p , for the $\text{YBa}_2(\text{Cu}_{1-x}\text{Mn}_x)_3\text{O}_{7.8}$ samples with x taking values 0, 0.01, **0.015**, 0.020, 0.025, 0.035 and 0.050, $\text{YBa}_2(\text{Cu}_{0.075}\text{Fe}_{0.025})_3\text{O}_{7.8}$, $\text{YBa}_2(\text{Cu}_{0.075}\text{Ni}_{0.025})_3\text{O}_{7.8}$ and $\text{YBa}_2(\text{Cu}_{0.075}\text{Zn}_{0.025})_3\text{O}_{7.8}$ samples at (a) 5 K, (b) 50 K and (c) 77 K.

extrinsic pinning, Mn doped samples exhibit an increase in condensational pinning energy with doping upto 2.0 % Mn which reduces on further doping.

In summary, the variation of $J_{c9}(0)$, F_p and H_{c1g}^* at 5 K show gradual decrease with increasing Mn concentration whereas at 50 K and 77 K they all exhibit an increase upto 2 % Mn content beyond which they decrease again. Observation of a maximum at 2 % Mn could have been due to the matching of Abrikosov vortex density and the defect induced number of pinning sites [40] due to the Mn doping being optimum at 2 % Mn addition over these temperatures, causing pinning to be effective.

4.4 AC MH LOOPS :

As the ceramic superconductors are of highly granular nature, the effective usefulness of these materials is determined by the properties of the weak links and the grains together. ac measurements have been useful in studying the weak link behavior at low fields. In ac measurements, temperature and field variation of

fundamental susceptibilities are commonly studied while the ac magnetization studies are rare. However, since in ac MH loop measurements the harmonic components are also included, this method is a versatile technique in studying the granular properties. Besides, magnetization measurement can give information on penetration depth in addition to lower critical field, ac losses, etc.

In literature, ac MH loops are reported to have been recorded using electronic integrator method [41,42,43], analog to digital converter method [44], by summing up of the harmonic components which were measured individually [45] etc. $\text{YBa}_2\text{Cu}_3\text{O}_{7-\delta}$ is the widely studied system using the MH loop technique because of the easy formation of this compound and its phase stability. The MH loop obtained had been analysed using exponential model [42] and Kim's model [43]. Ghatak *et al.* [46] have studied the harmonic behavior from the MH loop on the pure and Silver doped YBCO samples. Ji *et al.* [47] have reported varied shapes of the MH curves for different excitation frequencies and have found that curves obtained at higher frequencies are closer to the one obtained from critical state calculations.

Doping studies have been important in modifying the parent material with useful properties such as critical current density flux pinning etc., besides being used as a tool to understand the mechanism of superconductivity. Zheng et al [32] have studied the Co and Zn doped $\text{YBa}_2\text{Cu}_3\text{O}_{7-\delta}$ and reported an increase in the anisotropy on doping. Jirsa *et al* [39] have calculated the penetration depth from the irreversible magnetization region on Mg doped $\text{YBa}_2\text{Cu}_3\text{O}_{7-\delta}$ granular samples. In the previous section, from the temperature and field variations of ac susceptibility, 1.5 % Mn doped sample was found to have superior weak link properties, whereas the DC measurements reveal that the grain properties such as J_{cg} decrease systematically with doping. Hence to study weak link magnetic properties and to extend the analysis of temperature and field variation of ac susceptibility measurements, ac magnetic hysteresis measurements were carried out on Mn doped $\text{YBa}_2\text{Cu}_3\text{O}_{7-\delta}$ superconductor.

4.4.1 Experimental:

In a mutual inductance bridge, if there is only one secondary coupled inductively with the primary, then the voltage induced across the secondary will be proportional to the rate of change of flux density (dB/dt) within the coil. However, If two identical secondaries of equal turns were connected in series opposition and a sample is kept in one of the secondaries, then the cumulative voltage developed

across the secondaries will be proportional to the rate of change of magnetization of the sample. On integrating the output signal from the secondary coil of such a mutual inductance bridge ac MH loop can be obtained. Gomory *et al.* [48] have pointed out that a Phase Sensitive Detector (PSD) operating in the flat band mode can be exploited for this purpose by sweeping the reference phase of the PSD. The output of the PSD, as the reference phase (θ) is swept from 0 to 2π , is given as [49,50]

$$S(\phi) = 4\mu_0 n V f (1/D) M(\phi) \quad (4.41)$$

where μ_0 is the permeability of the free space, n is the number of turns per unit length of the secondary coil, V is the sample volume, f is the frequency of the primary field and D is the demagnetizing factor. The corresponding oscillating field is

$$H(\phi) = H_m \sin(\phi)$$

where H_m is the ac field amplitude.

Using this technique, ac MH loops were recorded on parallelepiped shaped samples of the $\text{YBa}_2(\text{Cu}_{1-x}\text{Mn}_x)_3\text{O}_{7-\delta}$ with $x = 0, 0.01, 0.015, 0.020, 0.025, 0.035$ and 0.050 values, $\text{YBa}_2(\text{Cu}_{0.075}\text{Fe}_{0.025})_3\text{O}_{7-\delta}$, $\text{YBa}_2(\text{Cu}_{0.075}\text{Ni}_{0.025})_3\text{O}_{7-\delta}$ and $\text{YBa}_2(\text{Cu}_{0.075}\text{Zn}_{0.025})_3\text{O}_{7-\delta}$ samples the of size $\sim 2 \text{ mm} \times 2 \text{ mm} \times 10 \text{ mm}$.

4.4.2 Results and Discussion:

Figure 4.20 and 4.21 show the magnetization curves for all the samples studied, at the least and the highest applied fields of 0.2 and 80 Oe respectively. The slope of the MH loop indicates the decreasing superconducting volume fraction with doping. Figures 4.22a and *b*, and 4.23a, *b* and *c* show the typical field variation of MH loops for the pure and $\text{YBa}_2(\text{Cu}_{0.075}\text{Mn}_{0.025})_3\text{O}_{7-\delta}$ samples. At very low fields, in perfect diamagnetically shielded state, the MH loop is a reversible straight line with a slope of magnitude equal to the superconducting volume fraction at that temperature and field. At 77 K, except for the pure sample, the slope of the loop was less than one indicating that the entire bulk of the sample is not superconducting. As the field is increased above lower critical field of the weak link (H_{c1w}) flux penetrates into the weak link regions of the sample and exhibits opening up of the MH loop. However, in the present study even at minimum applied field of 0.2 Oe, at 77 K, all the samples except the pure one showed opened loop, indicating the lower critical field of the weak links, H_{c1w} , is less than 0.2 Oe. The pure sample shows opening up of loop at ~ 0.7 Oe. After the opening up of loop above H_{c1w} , as more flux penetrates into the weak link region, the loop area increases till the flux reaches the center of weak link region. This field, at which the flux just reaches the center of the weak link region, is

represented as weak link - full penetration field, H_{pw} . Beyond this field, since the superconducting volume fraction of the weak link region reduces, the MH loop starts collapsing which is expected to close completely at the upper critical field of the weak links H_{c2w} .

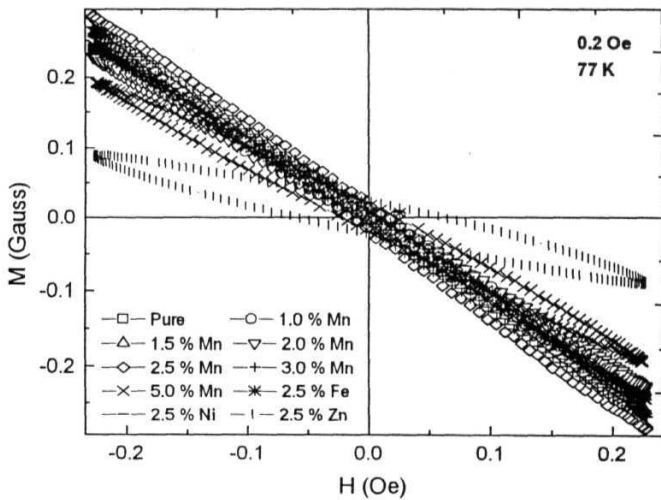


Figure 4.20 ac magnetization curve for the $YBa_2(Cu_{1-x}Mn_x)_3O_{7-\delta}$ samples with x taking values 0, 0.01, 0.015, 0.020, 0.025, 0.035 and 0.050, $YBa_2(Cu_{0.075}Fe_{0.025})_3O_{7-\delta}$, $YBa_2(Cu_{0.075}Ni_{0.025})_3O_{7-\delta}$ and $YBa_2(Cu_{0.075}Zn_{0.025})_3O_{7-\delta}$ samples at 0.2 Oe.

However, since the upper critical field of the weak links H_{c2w} is higher than the lower critical field of the grains, H_{c1g} , the loop does not collapse completely to make a reversible straight line. But, the edges of the loop collapse with an opened central region. The slope of the MH loop when the area of the loop has reached the minimum will be less than -1 , showing a reduced diamagnetism. This reduced slope corresponds to the diamagnetic grain fraction f_{g77} . On further increase of field amplitude, the loop once again starts opening up at a faster rate of increase in bop area. This corresponds to the flux penetration into the grains. The field corresponding to the change in rate of increase of loop area with field is taken as the lower critical field of the grains, H_{c1g} . Table 4.6 gives the H_{pw} and H_{c1g} for all the samples studied, obtained from the plots of field variation of loop area (Fig. 4.24).

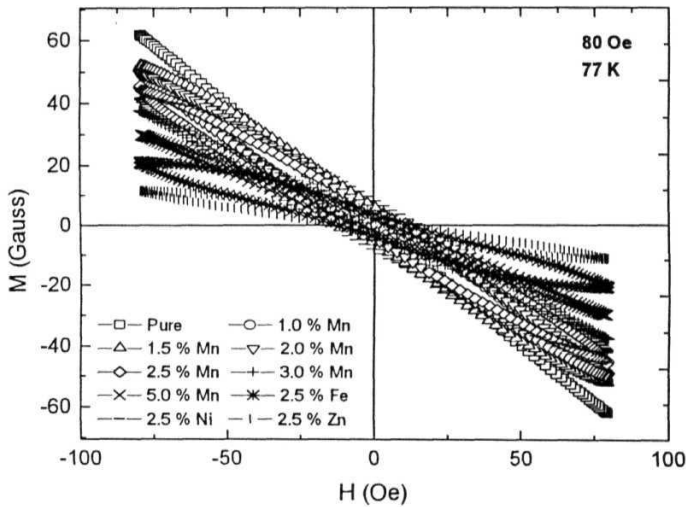


Figure 4.21 ac magnetization curve for the $\text{YBa}_2(\text{Cu}_{1-x}\text{Mn}_x)_3\text{O}_{7-\delta}$ samples with x taking values 0, 0.01, 0.015, 0.020, 0.025, 0.035 and 0.050, $\text{YBa}_2(\text{Cu}_{0.075}\text{Fe}_{0.025})_3\text{O}_{7-\delta}$, $\text{YBa}_2(\text{Cu}_{0.075}\text{Ni}_{0.025})_3\text{O}_{7-\delta}$ and $\text{YBa}_2(\text{Cu}_{0.075}\text{Zn}_{0.025})_3\text{O}_{7-\delta}$ samples at 80 Oe

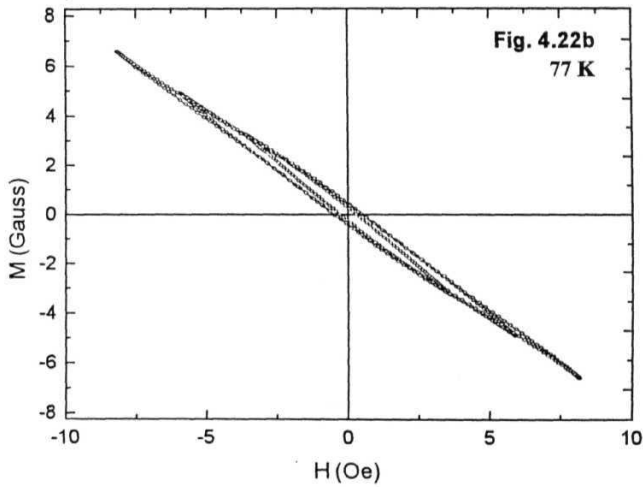
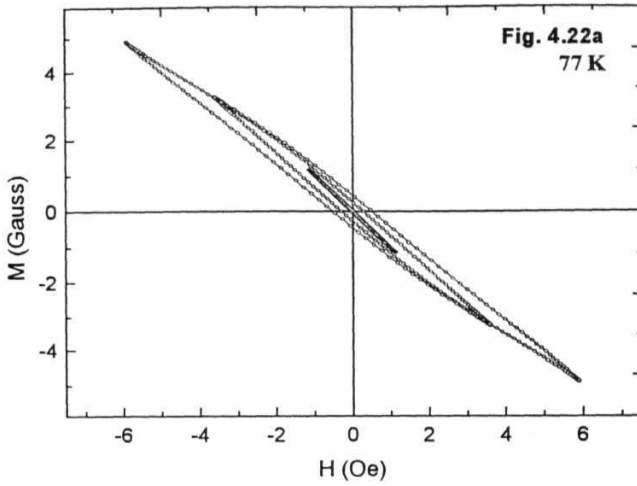
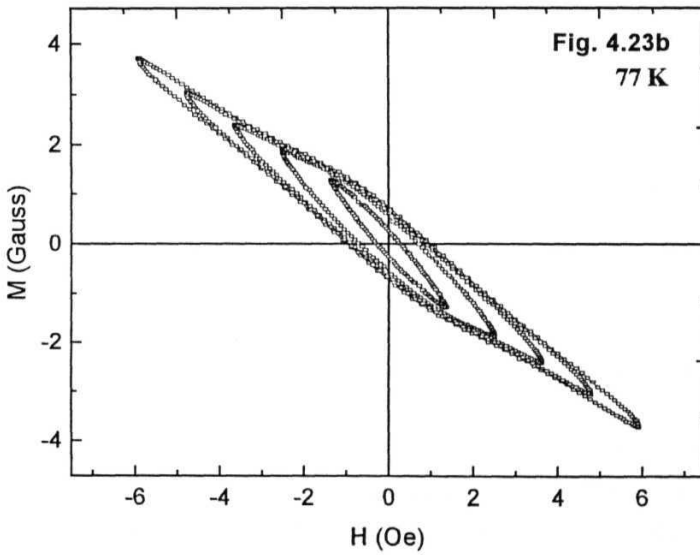
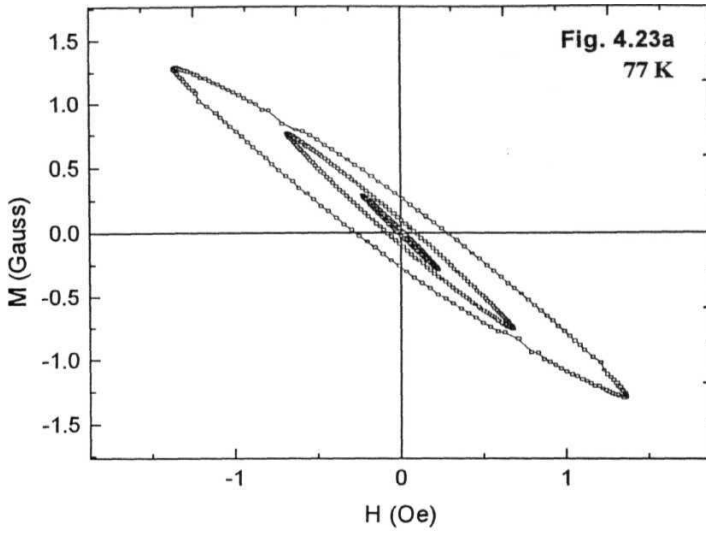


Figure 4.22 ac magnetization curve for the $\text{YBa}_2\text{Cu}_3\text{O}_{7.5}$ sample, showing the different characteristic field regions. (a) Initial loop opening -flux entry into weak link region (b) Loop collapse -beyond the weak link full penetration.



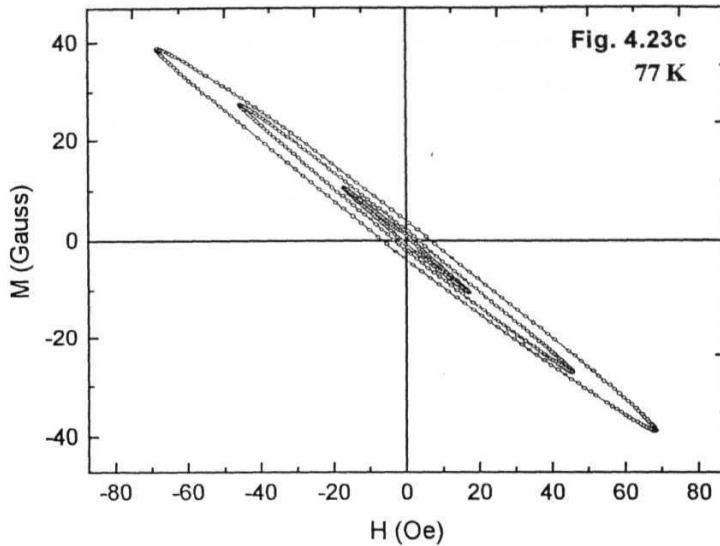


Figure 4.23 ac magnetization curve for the $\text{YBa}_2(\text{Cu}_{0.075}\text{Mn}_{0.025})_3\text{O}_{7-\delta}$ sample showing the different characteristic field regions. (a) Initial loop opening -flux entry into weak link region (b) Loop collapse – narrowing of the tail region beyond the weak link full penetration (c) loop reopening –flux entry into the grains.

4.4.2.1 Flat Band Susceptibility:

The ac MH loop recorded is the resultant sum of the harmonic components of susceptibility and hence the flat band susceptibility can be obtained from the MH loops recorded at different field amplitudes. The real (χ') and imaginary (χ'') components of flat band susceptibility are deduced from the slope and remnant value of the ac MH loop respectively. The slope is calculated from the peak magnetization value, M_p , at the peak applied field, H_m , as (M_p/H_m) . The imaginary part of flat band susceptibility is given as (M_{rem}/H_m) , where M_{rem} is the remnant magnetization, i.e. the magnetization at zero field amplitude. Figure 4.25 shows the real (χ') and imaginary (χ'') components of flat band susceptibility for the $\text{YBa}_2(\text{Cu}_{1-x}\text{Mn}_x)_3\text{O}_{7-\delta}$ samples with $x = 0, 0.01, 0.015, 0.020, 0.025, 0.035$ and 0.050 and $\text{YBa}_2(\text{Cu}_{0.075}\text{Fe}_{0.025})_3\text{O}_{7-\delta}$, $\text{YBa}_2(\text{Cu}_{0.075}\text{Ni}_{0.025})_3\text{O}_{7-\delta}$ and $\text{YBa}_2(\text{Cu}_{0.075}\text{Zn}_{0.025})_3\text{O}_{7-\delta}$ samples, at 77 K. Since the fundamental harmonic susceptibility is the dominant component of the flat band

susceptibility, it can be seen in the figure that the shape of the fundamental harmonic susceptibility is imposed on the flat band susceptibility as well. The real part of flat band susceptibility represents the typical diamagnetic transition of the weak link region with field. As field is increased the diamagnetic signal reduces gradually from a maximum value to a lower value and saturates. The maximum diamagnetic value obtained was -1 for the pure and 1.5 % Mn doped sample, while it was less than -1 for other samples decreasing with increasing dopant concentration. The volume susceptibility, χ' , at the constant region (plateau) corresponds to superconducting grain fraction (f_{g77}) which decreases with increasing dopant concentration. Beyond the plateau as the field is increased, a further rise in the diamagnetic value of the flat band susceptibility is observed. This corresponds to the flux entry into the grains. The diamagnetic signal from the Zn doped sample was remarkably low, because of its low transition temperature.

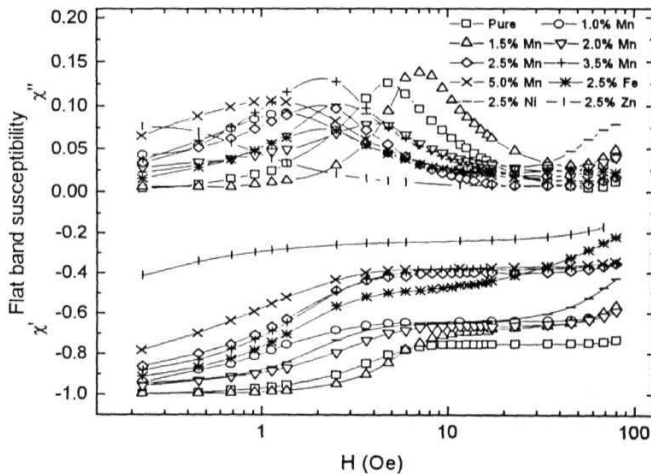


Figure 4.24 Plots of field variation of flat band susceptibility for the $\text{YBa}_2(\text{Cu}_{1-x}\text{Mn}_x)_3\text{O}_{7-\delta}$ samples with x taking values 0, 0.01, 0.015, .020, 0.025, 0.035 and 0.050, $\text{YBa}_2(\text{Cu}_{0.075}\text{Fe}_{0.025})_3\text{O}_{7-\delta}$, $\text{YBa}_2(\text{Cu}_{0.075}\text{Ni}_{0.025})_3\text{O}_{7-\delta}$ and $\text{YBa}_2(\text{Cu}_{0.075}\text{Zn}_{0.025})_3\text{O}_{7-\delta}$ samples derived from the ac MH loop at 77 K.

The imaginary part of the flat band susceptibility showed a loss peak at the weak link full penetration field, H_{pw} , where the flux just reaches the center of the weak links. All samples had H_{pw} less than 8 Oe indicating J_{cw} to be of the order of

$\sim 90 \text{ A/cm}^2$. The 1.5 % Mn doped sample showed the highest H_{pw} of $\sim 8 \text{ Oe}$, which reflects the better weak link characteristics. Beyond the weak link loss peak, as field is increased above H_{c1g} , the imaginary part of the flat band susceptibility shows a little rise due to the granular losses arising from the flux entry into the grains.

4.4.2.2 ac Losses:

The area enclosed by an MH Loop gives the ac loss per cycle per unit volume and is related to the imaginary part of the fundamental ac susceptibility as

$$\chi'' = \frac{2\mu_0}{H_m^2} \oint M \cdot dH \quad (4.42)$$

The area enclosed by the MH loop, at 77 K for an applied field of 0.2 and 80 Oe, for the samples studied, is shown in Figure 4.24. Typically the log-log plots of the area plotted against the applied field amplitude (H_m) exhibited two different slopes at lower and higher fields with a change over region in between. The area enclosed

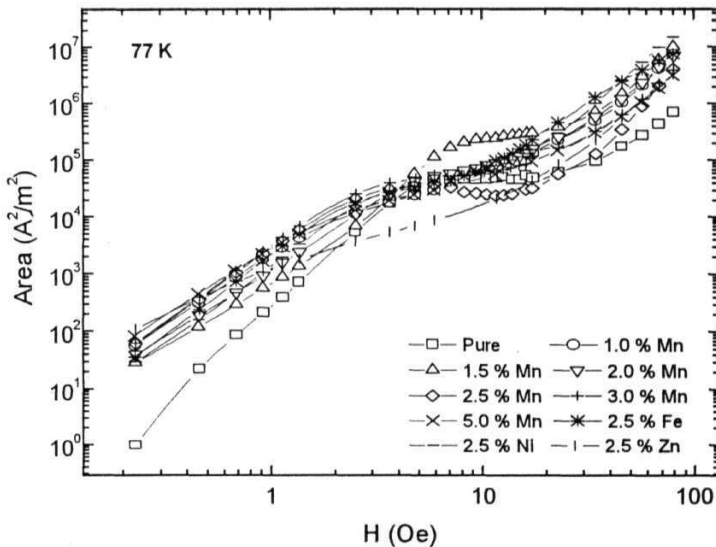


Figure 4.25 Plots of field variation of loop area for the $\text{YBa}_2(\text{Cu}_{1-x}\text{Mn}_x)_3\text{O}_{7-\delta}$ samples with x taking values 0, 0.01, 0.015, 0.020, 0.025, 0.035 and 0.050, $\text{YBa}_2(\text{Cu}_{0.075}\text{Fe}_{0.025})_3\text{O}_{7-\delta}$, $\text{YBa}_2(\text{Cu}_{0.075}\text{Ni}_{0.025})_3\text{O}_{7-\delta}$ and $\text{YBa}_2(\text{Cu}_{0.075}\text{Zn}_{0.025})_3\text{O}_{7-\delta}$ samples.

by the MH loop at the lower field regime corresponds to the ac losses due the weak link region and the area at the higher fields corresponds to the granular ac losses. Both the regions showed power relation with the applied field amplitude with an average exponent of 2.63 and 2.96 respectively. The saturation point in the Initial rise in area corresponds to the full penetration field of the weak links, H_{pw}^* and is tabulated in Table 4.6. The 1.5 % Mn doped sample showed the highest H_{pw}^* value indicating the better weak link property exhibited by it. In the weak link loss region, i.e. at lower fields, pure sample showed a minimum loss and the 5.0 % doped sample showed maximum loss. Ni and Fe doped samples also showed higher granular losses. However, Zn doped sample showed the least loss. This could be because of the lower superconducting fraction of this sample, the experimental temperature of 77 K being too close to its diamagnetic onset temperature of $T_c(\text{onset}) = 78.58$ K.

Table 4.6 H_{c1g} calculated from the flux profile plots and that calculated from the field variation of ac susceptibility and J_{cg} calculated using Eqn. 4.45.

Sample	H_{pw} (Oe)	H_{c1g} calculated from flux profile (Oe)	H_{c1g} calculated from $\chi(H)$ (Oe)	J_{cg} at 77 K $\times 10^4$ (Amp/cm ²)
Mn				
0.0	5.1	43.85	41.10	22.23
1.0	1.5	35.78	30.60	6.05
1.5	7.0	32.09	33.50	3.57
2.0	4.4	31.06	28.30	4.90
2.5	2.8	27.70	23.99	2.62
3.5	2.9	29.60	32.57	7.34
5.0	1.8	28.35	27.47	6.41
Fe				
2.5	2.1	8.13	11.60	1.27
Ni				
2.5	2.7	18.66	17.26	1.74
Zn				
2.5	0.8	20.89	17.02	1.32

Flux Profiles :

The flux profile within the sample can be obtained from the peak magnetization value (M_p). The normalized penetration is given as [49]:

$$\frac{p}{R} = 1 - \sqrt{-\frac{dM}{dH}} \quad (4.43)$$

where p is the extent the flux has penetrated from the surface above the radius, R of the sample. Figure 4.26 shows the flux profiles at 77 K for all the samples studied.

The flux profile, typically increases monotonically to a maximum value at weak link full penetration field, H_{pw} . From this maximum penetration value it drops to a lower value as field is increased further and remains constant. This region where the penetration remains constant, if extrapolated to zero field, will intercept x-axis at (p^*/R) . From this (p^*/R) superconducting grain fraction, f_{g77} , at 77 K can be estimated as [51],

$$f_g = \left(1 - (p^*/R)\right)^2 \quad (4.44)$$

The f_{g77} values obtained using the above relations agrees well with the values obtained from the flat band susceptibility and 77 K field variation of ac susceptibility. As the field is increased, the flux entry into the grains is seen as increase in p/R beyond the (p/R) in the flux profile. The field at which p/R starts increasing beyond the constant region is the lower critical field of the grains, H_{c1g} . The estimated H_{c1g} are tabulated in the Table 4.6. From the slope the $dH_m/d(p/R)$ above the H_{c1g} , critical current density of the grains can be estimated as[51],

$$J_{cg} = \left(\frac{dH_m}{dp} \right)_{(p=p^*)} \left(\frac{R}{R_g} \right) \left(1 - p^*/R \right)$$

The J_{cg} estimated using the above relation are tabulated in Table 4.6. The order of magnitude of J_{cg} as well as the trend of variation in J_{cg} values agree well with those calculated from the M_{rem} of the DC magnetization measurements (Table 4.5), except for the pure sample for which a higher value is obtained in the flux profile method. This supports the versatility of the flux profile calculations from the MH loops.

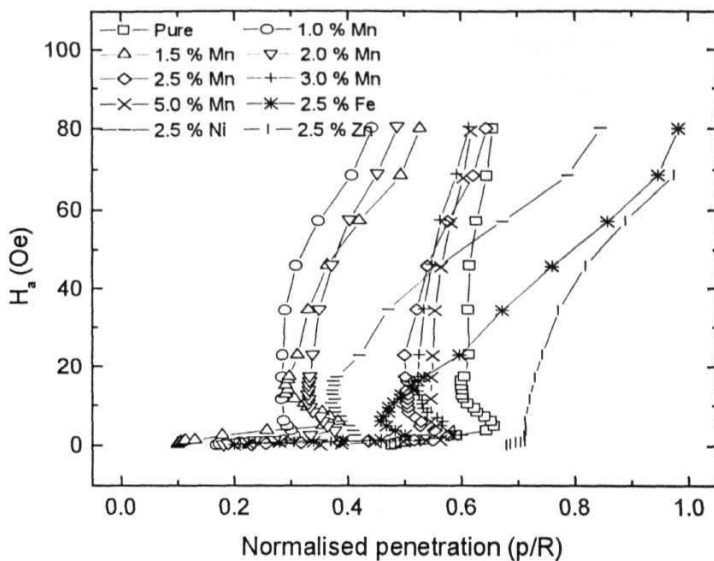
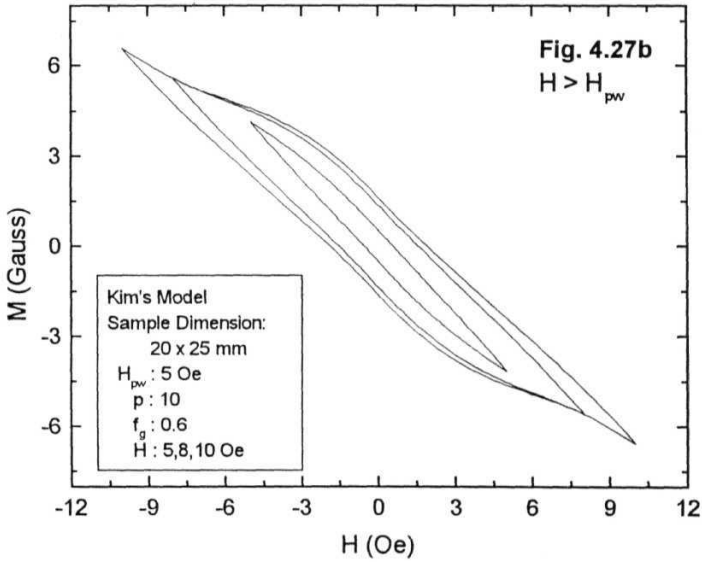
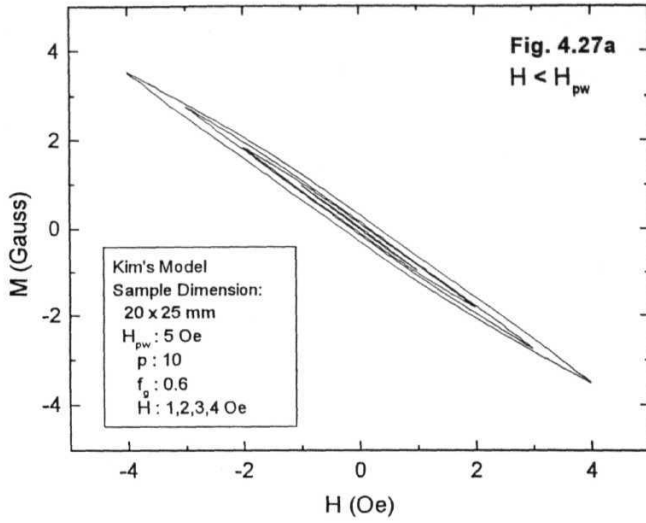


Figure 4.26 Flux profile plots deduced from the ac MH loop for the $\text{YBa}_2(\text{Cu}_{1-x}\text{Mn}_x)_3\text{O}_{7-\delta}$ samples with x taking values 0, 0.01, 0.015, 0.020, 0.025, 0.035 and 0.050, $\text{YBa}_2(\text{Cu}_{0.075}\text{Fe}_{0.025})_3\text{O}_{7-\delta}$, $\text{YBa}_2(\text{Cu}_{0.075}\text{Ni}_{0.025})_3\text{O}_{7-\delta}$ and $\text{YBa}_2(\text{Cu}_{0.075}\text{Zn}_{0.025})_3\text{O}_{7-\delta}$ samples.

Numerical Simulation of MHloops

In order to show effectiveness of the numerical simulation **described** In section 4.1.2, The ac MH loops were calculated following **the procedure given in** Section 4.1.2, using Kim's model of $J_c(H_i)$ for the conditions **that are closer to** experimental MH loop recorded at 77 K. The programme used is given in Appendix I. The simulations were carried out for a typical sample dimension of 20 x 25 mm. **The** full penetration field of the weak link, H_{pw} , was assumed as 5 Oe, p as 10 and f_g as 0.6. MH loops were generated to show the initial loop opening **upto**



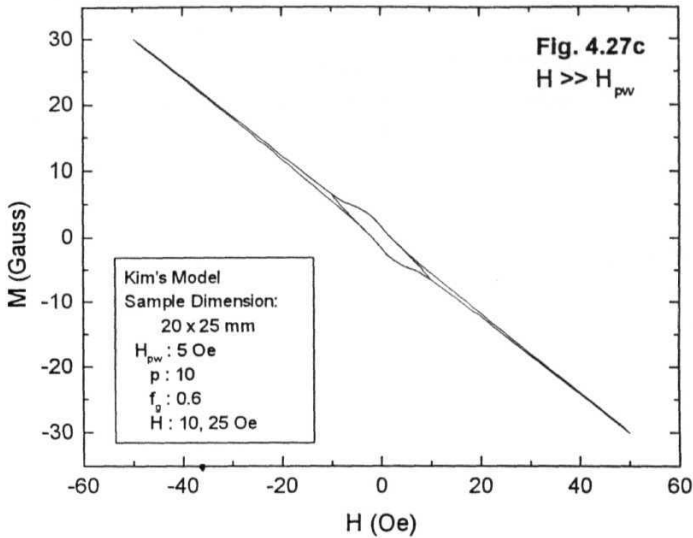


Figure 4.27 Kim's model simulation of MH loop using the numerical procedure described in section 4.1.2. (a) Initial loop opening -flux entry into weak link region (b) Loop collapse - narrowing of the tail region beyond the weak link full penetration (c) complete weak link suppression at $H \gg H_{pi}$. The central opened region correspond to the grain response.

H_{pw} , the loop closure on further increase of field and complete suppression of weak link response ($H \gg H_{pw}$). The loops were generated for an grain fraction, f_g , of 0.6. It can be seen from the Fig. 4.27c that at high fields when the magnetization is **due** to the grains and the slope of the loop will give the grain fraction, which is 0.6 in this simulation.

REFERENCES :

- 1 J. E. Evetts and B. A. Glowacki, *Cryogenics*, 28, 641 (1988).
- 2 P. J. Kung, M. P. Maley, M. E. McHenry, J. O. Willis, M. Murakami and S. Tanaka, *Phys. Rev.* **B48**, 13 922 (1993).
- 3 Y. Xu and M Suenaga, *Phys. Rev.* **B43**, 5516 (1991).
- 4 R. F. Jardim and S. Gama, *Physica* **C159**, 306 (1989).
- 5 I. Dhingra, S. C. Kashyap and B. K. Das, *J. Mater. Res.* **9**, 2771(1994).
- 6 N. L. Saini, P. Srivastava, B. R. Sekhar and K. B. Garg, *Int. J. Modern Phys.*, **B6**, 3575(1992).
- 7 N. L. Saini, K. B. Garg, H. Rajagopal and A. Sequeira, *Sol. State. Comm*, **82**, 895 (1992).
- 8 K. Mendelssohn, *Proc. Roy. Soc. (London)*, **A152**, 34 (1935).
- 9 C. P. Bean, *Rev. Mod. Phys.*, 31, 1935 (1964).
- 10 D. X. Chen, A. Sanchez, T. Puig, L M. Martinez and J. S. Munoz, *Physica* **C168**, 652(1990).
- 11 S. Ravi and V. Seshu Bai, *Phys. Rev.* **B49**, 13 082 (1994).
- 12 S. Ravi and V. Seshu Bai, *Physica* **C230** 51 (1994).
- 13 B. V. Kumaraswamy, R. Lal and A. V. Narlikar, *Phys. Rev. B* 53, 6759 (1996)
- 14 Y. B. Kim, C. F. Hempstead and A. R. Strand, *Phys. Rev. Lett*, **9**, 306 (1962).
- 15 F. Irie and K. Yamafuji, *J. Phys. Soc. Jpn.*, 23, 255 (1967).
- 16 W. A. Fietz, M. R. Beasley, J. Silcox and W. W. Webb, *Phys. Rev.* **A136**, 335 (1964).
- 17 S. F. Wahid and N. K. Jaggi, *Physica* **C184**, 88 (1991).
- 18 D. X. Chen and R. B. Goldfarb, *J. Appl. Phys.* **66**, 2489 (1989).
- 19 K. Yamamoto, H. Mazaki and H. Yasuoka, *Phys. Rev.* **B47**, 915 (1993).
- 20 P. Chaddah, K. V. Bhagwat and G. Ravi Kumar, *Physica* **C159**, 570 (1989).
- 21 N. V. Vuong, *Supercon. Sci. and Tech.* **Xx**, 783 (1995).
- 22 P.O. Hetland, T. H. Johansen and H. Bratsberg, *Cryogenics*, 36, 41 (1996).
- 23 J. R. Clem, *Physica* **C153-155**, 50 (1988).
- 24 D. X. Chen, K. Y. Wang and A. Hernando, *Physica* **C274**, 39 (1997).
- 25 D. X. Chen, A. Sanchez and J. S. Munoz, *J. Appl. Phys.* **67**, 3430 (1990).
- 26 M. Tinkham and C. J. Lobb, *Solid State Physics*, eds. H. Ehrenreich and D. Turnbull (Academic, San Diego, 1989) Vol. 42, pp 91-134.
27. H. Kupfer, I. Apfelstedt, W. Schauer, R. Flukiger, R. Merier-Hirmer and H. Wuhl, *Z Phys. B Condens. Matter* **69**, 159 (1987).

- 28 S. D. Murphy, K. Renouard, R. Crittenden and S. M. Bhagat, *Sol. St. Commun.* 69,367(1989).
- 29 H. Mazaki, S. Katsuyama, H. Yasuoka, Y. Ueda and K. Kosuge, *Jpn. J. Appl. Phys.*, 28, L1909(1989).
- 30 H. Mazaki, S. Katsuyama, H. Yasuoka, and K. Kosuge, *Jpn. J. Appl. Phys.*, 30, 1386(1991).
- 31 S. H. Guo, C. C. Lam, K. C. Lau and M. S. Chang, *Physica* **C247**, 115 (1995).
- 32 D. N. Zheng, A. M. Campbell, J. D. Johnson, J. R. Cooper, F. J. Blunt, A. Porch and P. A. Freeman, *Phys. Rev.* **B49**, 1417 (1994).
- 33 R. B. Goldfarb, M. Lelental and C. A. Thompson in *Magnetic susceptibility of superconductors and other spin systems* eds. R. A. Hein, T. L. Francasilia and D. H. Liebenbery (Plenum, New York, 1991), p.68.
- 34 R. B. Flippen, T. R. Askew, J. A. Fendrich and B. M. Vlcek, *Physica* **C228**, 85 (1994).
- 35 L A Angurel, F. Lera, C. Rillo and R. Navarro, *Physica* **C230**, 361 (1994).
- 36 N. Savvides, *Physica* **C165**, 371 (1990).
- 37 Bokhimi A. Morales, *Physica C*, **234**, 333 (1994).
- 38 M. Murakami in *"Melt processed high temperature superconductors"* (World Scientific, Singapore, 1992) p. 181.
- 39 M. Jirsa, L. Pust, P. Nalevka, L. Papadimitriou, I. Samaras, and O. Valasslades, *Supercond. Sci. Tech.*, **11**, 757 (1998).
- 40 Y. Li, Lijie Cui, Guohui Cao, Q. Ma, C. Tang, Y. Wang, L. Wei, Y. Z. Zhang, Z. M. Zhao and Elisa Baggio-Saitovitch, *Physica* **C314**, 55 (1999).
- 41 W. A. Fietz, *Rev. Sci. Instr.*, **36**, 1621 (1965).
- 42 A. K. Grover, C. Radhakrishnamurthy, P. Chadda, G. Ravikumar and G. V. Subba Rao, *Pramana J. Phys.*, **30**, 569 (1988).
- 43 I. E. Edmond and L. D. Firth, *J. Phys. Cond. Matter*, **4**, 3813 (1992).
- 44 R. Maury, A. R. Fert, J. P. Redoules, J. Ayache, J. Sabras and C. Monty, *Physica*, **C167**, 591 (1990).
- 45 R. Navarro, F. Lera, C. Rillo and J. Bartolome, *Physica*, **C167**, 549 (1990).
- 46 S. K. Ghatak, A. Mitra and D. Sen, *Phys. Rev.*, **B45**, 951 (1992).
- 47 Z. M. Ji, J. F. Geng, W. M. Chen, H. X. Yu, A. M. Sun and Q. H. Chen, S. Z. Yang and X. Jin, *Physica*, **C279**, 233 (1997).
- 48 F. Gomory, *Rev. Sci. Instrum.*, **62**, 2019 (1991).
- 49 N. Harish Kumar and V. Seshu Bai, *Phys. Rev.* **B53**, 15281 (1996).

50 H. Jiang and C. P. Bean, *Rev. Sci. Instrum.*, 66, 3284 (1995).

51 Ah. Dang, P. A. Godelaine, Ph. Vanderbemden, R. Cloots and M. Ausloos,
J. Appl. Phys., 77, 3560 (1995).

CHAPTER - 5

SUMMARY & CONCLUSIONS

Effect of Mn at the Cu site of the YBCO superconductor on its transport and magnetic properties is the objective interest this thesis. YBCO has proved to be of technological importance among the family of HTSC with its phase stability, chemical adaptability and high critical current density. As known, YBCO has a triple perovskite structure stacked along c-axis. The CuO_2 plane along the ab plane and the CuO chains along the b - axis form the center of electronic activity which constitute superconductivity in these materials. The variation of holes in the CuO_2 plane, by means of substitution at Y, Ba and Cu sites, drive this system from underdoped to overdoped regimes. In the underdoped regime metal-to-insulator transition is observed, while at the overdoped regime superconductivity is suppressed mildly.

In doping studies, doping at the copper site has been of prime importance. Primarily, doping an impurity element into the parent superconducting compound may enhance or deteriorate the superconducting properties of the parent compound thereby giving a clue to the origin of superconductivity in it. Secondly doping can be used to enhance the physical properties such as density, ductility etc. which may add to the technological advantage of the material. Dopants such as Co, Fe, Al etc. which go into the Cu(I) site have least effect on T_c and show Orthorhombic to Tetragonal

(OT) transition, whereas the Cu(II) site dopants such as Ni, Zn etc. drastically suppress the T_c and no OT transition is observed. Due to the low solubility limit of Mn in $\text{YBa}_2\text{Cu}_3\text{O}_{7-\delta}$ a thorough study on the transport and magnetic properties of this system is not available in the literature

$\text{YBa}_2(\text{Cu}_{1-x}\text{Mn}_x)_3\text{O}_{7-\delta}$ samples with x taking values 0, 0.01, 0.015, 0.020, 0.025, 0.035 and 0.050 and $\text{YBa}_2(\text{Cu}_{0.075}\text{Fe}_{0.025})_3\text{O}_{7-\delta}$, $\text{YBa}_2(\text{Cu}_{0.075}\text{Ni}_{0.025})_3\text{O}_{7-\delta}$ and $\text{YBa}_2(\text{Cu}_{0.075}\text{Zn}_{0.025})_3\text{O}_{7-\delta}$ samples were prepared under the same conditions through solid state reaction. Samples with 2.5 % Fe, Ni and Zn dopants were also prepared to study the marked similarities and contrast of the Mn doping with the other 3d elemental doping, especially in the context of the doping sites namely Cu(I) and Cu(II). Mn is known to occupy Cu(I) site from the neutron diffraction experiments. On Mn-doping, the lattice parameters, a , b and c , calculated from the XRD pattern remained more or less unchanged. XRD pattern for the 3.5 and 5.0 % Mn doped samples showed impurity lines due to $\text{Ba}_3\text{Mn}_2\text{O}_8$ at $\sim 28^\circ$ and 31° of 2 θ values with intensity less than 3 %. The relative density, which is the ratio of the observed density to the theoretical one, ($D_{\text{obs}}/D_{\text{theo}}$), varied between 62.3 % to 79.3 %. Samples with 1.0 % and 5.0 % Mn dopant comparatively are less densely packed (or more porous) than the other Mn doped samples. While 2.5 % Zn doped had the least relative density of all. The grain size increases gradually from 7.74 μm for the pure YBCO sample to 15.15 μm for the 2.5 % Mn doped sample, beyond which it remains at around $\sim 11.2 \mu\text{m}$.

5.1 TRANSPORT PROPERTIES :

Across the superconducting transition, as the temperature is lowered below T_c , a phase transition marked by the onset of charge carrier condensation occurs which is responsible for the sharp changes in the electromagnetic and kinetic properties of the superconductor. The Fermi Energy (E_f) of $\text{YBa}_2\text{Cu}_3\text{O}_{7-\delta}$ system falls in the vicinity of Cu-3d and O-2p orbitals and these orbitals constitute the superconductivity in this system. Hence the doping at Cu sites had attracted much attention for the information that can be obtained on doping. In the present work, effect of Mn at the Cu(I) site is studied through temperature variation of resistivity and Seebeck coefficient.

5.1.1 Resistivity :

Temperature variation of resistivity showed a single drop, at T_c , from $p(\text{onset})$ to the measurable limit of zero. The onset of resistivity transition, $T_{c(\text{onset})}$ did not vary much, but the zero resistivity temperature T_{zero} dropped significantly on doping. The transition width was typically of the order of 3.5 K, except for the 2.5 % Zn doped sample which showed 5.92 K width and 5.0 % Mn doped sample that exhibited $\Delta T_c = 7.01$ K. The normal state resistivity in general increases monotonically with the dopant concentration. Temperature variation of resistivity decreased linearly from $p(300)$ at 300 K upto ~ 200 K, below which a negative deviation from the linear behavior, indicating an excess conductivity, was observed. This observed excess conductivity at temperatures below 200 K is attributed to the superconducting fluctuation, which manifests itself as rounding-off of resistivity curve above T_c . The thermal coefficient of resistivity, dp/dT and the extrapolated resistivity at absolute zero Kelvin, $p(0)$ were obtained from the linear to the $p(T)$ above 200 K to room temperature. The thermal coefficient, dp/dT increased with doping, while the $p(0)$ increased upto 2.0 % and showed a reduced rate of increase beyond 2 % doping. $p(\text{onset})$ and $p(300)$ exhibit behavior similar to $p(0)$.

5.1.2 Seebeck Coefficient :

Compared to resistivity and Hall coefficient measurements, in Seebeck coefficient measurement, the distortion arising from the defect structures etc, which are not the characteristics of the sample studied, is minimal.

The normal state $S(T)$ shows a change over from a concave behavior for the pure and low dopant concentration, to a convex behavior for doping above 3.5% of Mn and the Fe doped sample. The hole concentration, p_h , estimated from the $S(290)$ vs. p_h universal curve, decreases for increasing dopant concentration. The saturation above 3.5 % of Mn could be due to the solubility limit. The phonon contribution is enhanced with increasing amount of dopant. In our samples, for $x > 0.035$ the phonon drag contribution found to be negative, indicating a reversal in momentum transfer. In the Bosonic term of the Nagaosa Lee model we assume the Bosons to be the Cooper pairs and the effective mass is taken as $2m_e$. Thus a direct correlation between $S(T)$, hole concentration and E_f is obtained in this model. The Fermi energy, E_f , estimated from the fit decreases from 442 meV for the 1 % Mn doped sample to 146 meV for the 3.5 % Mn doped sample. The E_f for the 2.5 % Fe doped sample is

estimated to be 157 meV. This fall in the E_f could be an indication of the reduction of the charge carriers on doping, both Mn and Fe alike.

The temperature independent region of thermopower observed in $YBa_2Cu_3O_{7-x}$ system had been explained by considering a narrow band at the E_f . Quantitative estimation of the transport properties, under the narrow band considerations, using a few phenomenological parameters such as band width(W_D), width of the conduction window(W_G) and degree of band filling(F) is attempted using Gasumyants narrow band model. W_D signifies the width of the narrow band, and F signifies the filling factor related to hole density. The narrow band could be either a single narrow band in the DOS, or a narrow peak on a broad background. The width of the narrow band, as estimated from the W_D , increases from 23 meV for the $x=0.01$ sample to 119 meV for the $x=0.035$ sample. The filling factor increases from 0.515 for the 1% Mn doped sample to 0.524 for the 3.5 % Mn doped sample. The conduction window (W_G) varies marginally around 35% of W_D for the different samples studied but shows no systematic change. This means Anderson localization is invariant with doping.

In all the model calculations, parameters obtained for samples with the dopant concentration above 2.5 % Mn are comparable with that obtained for the Fe doped sample, showing that the effect of both the dopants, Mn and Fe, at Cu(I) site are similar.

5.2 MAGNETIC PROPERTIES :

As the ceramic superconductors are of highly granular nature, the effective usefulness of these materials is determined by the properties of the weak links and the grains together. ac measurements are useful in studying nature of the weak links of the superconductor while DC magnetization measurements are widely used to probe the grain properties with aid of its high field capabilities.

5.2.1 Temperature and Field Variation of ac Susceptibility :

The diamagnetic onset $T_{c(\text{onset})}$ measured from the real part of susceptibility, χ' varies marginally around 91.5 K for varying Mn dopant concentrations whereas it falls to 88.2 K for Fe dopant, 84.5 K for Ni dopant and 78.6 K for Zn dopant. At minimum measured temperature and field all the samples show a perfect diamagnetism, with χ' going to -1. Shielded grain fraction, f_{g10} , at 10 K estimated from the volume diamagnetism, decreases from a value of 0.83 for the pure one to 0.60 for the 2.5 %

Mn doped sample, while it was 0.72 and 0.80 for the 2.5 % Fe and Ni dopants respectively. Zn doped sample showed the least shielded grain fraction of 0.48.

The J_{cw} calculated fails rapidly with temperature. It could be well described by a relation of the form $J_{cw}(T) = J_{cwo} (1 - T/T_{cj})^{n_j}$ where J_{cwo} and n_j are constants and T_{cj} is the coherence temperature marking the onset of grain coherence. The exponent, n_j , varies closer one which is typical for the SIS (Superconducting-Insulator-Superconducting) type coupling of grains.

The relatively porous 1 % Mn doped sample has the lower f_{g10} compared to the pure and 1.5 % Mn doped samples. Similarly, 1 % Mn doped sample showed the least weak link J_{cwo} of 105 A/cm² while the 1.5 % Mn doped one showed the highest J_{cwo} of 370 A/cm². These jumps in J_{cwo} are rationalized in terms of the microstructural porosity for the 1 % Mn and the better density. This difference could be because of some minor unnoticed variations in the processing details that influence the microstructure and the weak link properties drastically. However, the J_{cwo} values for pure, 2.0, 2.5, 3.5 and 5.0 % Mn decreases steadily from 285 A/cm² for pure sample to 161 A/cm² for the 5.0 % Mn doped sample. The weak link J_{cwo} of Fe, Ni and Zn doped samples are 149 A/cm², 291 A/cm² and 207 A/cm² respectively. Dopants at the Cu(I) sites, Mn and Fe, reduce the weak link critical current density more than the Cu(II) site dopants, Ni and Zn. Among the Cu(I) site dopants, effect of Mn is minimal, compared to Fe, in suppressing the weak link J_c . Since the energizing fields in ac susceptibility measurements are low, we compare the temperatures at which same value of $J_{cg} = 2.4 \times 10^4$ A/cm² is observe for different compositions. The J_{cg} of the pure sample was 2.4×10^4 A/cm² at 89.79 K and the J_{cg} for 2.5 % doped sample was 2.4×10^4 A/cm² at 86.81 K. Fe and Ni doped samples showed the same J_{cg} at 77.18 and 82.19 K respectively.

In the field variation of ac susceptibility, at 50 K, for a minimum energizing field all the samples show perfect diamagnetism {i.e $\chi' \sim -1$ } whereas at 77 K, pure and low dopant samples (< 2% of Mn) alone showed closer to $\chi' = -1$ while others show a positive deviation from -1. This is because of the non superconducting fraction, f_n , of the weak link region at 77 K. Also the transitions at 50 K are quite sharp compared to those at 77 K.

Using the Kim's model the full penetration field, H_p and the constant representing the homogeneity in current path, p were obtained. The J_{cw} calculated from the full penetration field (H_p) at 50 K and 77 K agrees well with those obtained in the temperature variation of ac susceptibility and shows similar trend of variation with dopant concentration where the 1.5 % Mn doped sample showed better

intergranular properties while the one with 1.0 % exhibits inferior properties which can be correlated to the relative porosity in them.

5.2.2 DC Magnetization :

The negative peak, H_{c1g}^* , observed on virgin magnetization is taken as *indicative lower critical field* of the grains. At 77 K, H_{c1g}^* normalized with the grain size, falls monotonically with the increase of Mn concentration whereas at 50 K and 5 K it shows an increase in normalized H_{c1g}^* at 2 % Mn concentration and continues to drop with further addition of Mn.

The rate of fall of zero field critical current density J_{c0} with temperature for Mn doped sample is lower than that of 2.5 % of Ni, Fe and Zn at substituted samples. . In other words, Mn improves the temperature dependence, though decreases the magnitude of J_{c0} . The $J_c(H)$ at 5 K and 50 K were quite field independent compared to $J_c(H)$ at 77 K. At all temperatures J_c decreases systematically with Mn addition upto a concentration of 2.5 % and shows a reduced suppression beyond this concentration. This is in contrast with the variation of weak link critical current density, J_{cwl} , with Mn doping, where the 1.5 % Mn doped sample showed the superior magnetic properties. At 5 K, F_p decreased with increasing Mn doping whereas at 50 K and 77 K, F_p increased with increasing Mn doping upto 2% and decreased on further doping. In the absence of extrinsic flux pinning, the flux pinning force, F_p , can related to the condensational pinning energy and is found to decrease.

The variation of $J_{c0}(0)$, F_p and H_{c1g}^* at 5 K show gradual decrease with increasing Mn concentration whereas at 50 K and 77 K they all exhibit an increase upto 2 % Mn content beyond which they decrease again. Observation of a maximum at 2 % Mn could have been due to the matching of Abrikosov vortex density and the defect induced number of pinning sites due to the Mn doping being optimum at 2 % Mn addition over these temperatures, causing pinning to be effective.

5.2.3 ac MH Loop :

From the ac MH loops, flat band susceptibility, ac losses and flux profiles were deduced. At the minimum applied field of 0.2 Oe, at 77 K, all the samples except the pure one showed opened loop, indicating the lower critical field of the weak links, H_{c1w} , is less than 0.2 Oe. The H_{c1w} for the pure sample was ~0.7 Oe., The 1.5 % Mn doped sample showed the highest weak link full penetration field, H_{pw}^* , indicating the better weak link property exhibited by it. In the weak link loss region, i.e. at lower fields, pure sample showed a minimum loss and the 5.0 % doped sample

showed maximum loss. Ni and Fe doped samples also showed higher granular losses. J_{cg} estimated from the flux profiles is of the order of that obtained from the DC magnetization measurements and exhibits the similar trend of variation of J_{cg} with the dopant concentration.

In summary, Mn dopant at Cu(I) site of the YBCO superconductors, do **not** affect T_c substantially. An enhanced grain growth, irrespective of the density is observed upto 2.5 % Mn doping. Transport study indicates a fall in hole concentration in the conduction plane with doping. $J_{cw}(T)$ variation indicates SIS type of grain coupling. J_{cg} estimated from the DC magnetization measurements indicate that J_{cg} exhibits a weak temperature dependence on Mn doping. In general, the weak link properties such as J_{cw} , H_{pw} , H_{c1w} etc. vary with the density of the sample, which in turn is process dependent. While the grain properties such as J_{cg} , H_{c1g} , F_p , etc. vary systematically with Mn doping upto ~2.5 % and show a saturation, which are due to the effect of Mn doping and the consequent solubility limit of Mn in the YBCO system.

....The End

APPENDIX - I

```

c ***** Programme for Numerical simulation *****
c ***** of Hm vs chis for any  $J_c(H_i)$  *****

      real inc,m,n,k,jc,mag,inc1,np,kim
      dimension hi(1000),hk(1000),chi2(1000)
      dimension ypc(1000),ha(1000),chi1(1000)
      dimension ha1(1000)
               open(unit=7,file='outg.dat',status='old')
               open(unit=8,file='tryg.dat',status='old')
      read(8,*)n,m,a,b,hp,p,hm,fg
c      read(8,*)n,m,a,b,h0,k,np,hm,fg

      hm = hm
      hp = hp
c      ***** Exponential Model parameters *****
c      h0=hp/ALOG(1.0+p)
c      k=h0*p/a
c      ***** Kim's Model parameters *****
      h0=hp/(sqrt(1+p**2)-1)
      k=(p*h0)**2/(2*a)
      dx=a/m
      inc1=hm/n

      do 50 l=1,n
      ha(l)=hm-(l-1)*inc1
      c1=0.
      c2=0.

c      ***** Internal Field profile for initial magnetization *****
      do 10 i=1,m
      if (i.eq.1) then
      hi(i)=ha(l)
      else
      h=hi(i-1)
      if (h.le.0) then
      hi(i)=0
      else
      hi(i)=hi(i-1)-kim(h,k,h0)*dx
      if (hi(i).lt.0) hi(i)=0.
      endif
      endif
      continue

```



```

c      ***** Internal Field profile for reverse magnetization *****
      inc=3.1416/(m-1)
      do 20 j=1,m
        ha1(j)=ha(l)*Cos((j-1)*inc)
      do 30 i=1,m
        if (i.eq.1) then
          hk(i)=ha1(j)
        else
          h=hk(i-1)
          if (hi(i-1).eq.0)then

            else
              if (hi(i-1).ge.h) then
                hk(i)=hk(i-1)+kim(h,k,h0)*dx
                hb=hk(i)
              else
                hk(i)=hk(i-1)-kim(h,k,h0)*dx
              endif
            endif
          endif
        endif
      continue
30

c      ***** Calculation of magnetization from the Field Profile *****
      mag=0.
      do 75 i=1,m
        xk=a-(i-0.5)*dx
        mag=mag+(2*xk+b-a)*dx*hk(i)/(a*b)
c      ***** M(H) for a general geometry *****
c      mag=mag+(c*xk+b-a)*dx*hk(i)/(c*a**2/2+(b-a)*a))
75      continue
      ypc(j)=mag-ha1(j)

c      ***** Calculation of Susceptibility from the M(H) *****
      if (abs(ha1(i)).ge.ha(l)) ha1(i)=ifix(ha1(i))
      c1=c1+2*ypc(j)*ha1 G)/(m*ha(l)**2)
      c2=c2+2*ypc(j)*sqrt(ha(l)**2-ha1(j)**2)/(m*ha(l)**2)
20      continue

c      ***** Calculation of Matrix susceptibility *
      chi1(l)=-fg+(1-fg)*c1
      chi2(l)=(1-fg)*c2
c      chi1(l)=-fg*c1+(1-fg)
c      chi2(l)=fg*c2
c      chi1(l)=c1
c      chi2(l)=c2

      write(Y)ha(l),chi1(l),chi2(l)
      write(7,*)ha(l),chi1(l),chi2(l)

50      continue
      stop
      end

```

c ***** Subroutines for different $J_c(H_i)$ '

```
FUNCTION Ex(h,k,h0)
  real k,ex
  ex=k*exp(-(abs(h))/h0)
  write(*,*)h,ex
  RETURN
```

c END

```
FUNCTION kim(h,k,h0)
  real k,kim
  kim=k/(abs(h)+h0)
  write(*,*)h,kim
  RETURN
```

c END

```
FUNCTION pow(h,k,h0,np)
  real k,np
  pow=k*(abs(h)/h0)**(-np)
  write(*,*)h,pow
  RETURN
```

c END

LIST OF PUBLICATIONS

- 1 E. Isaac Samuel, V. Seshu Bai, K. M. Sivakumar and V. Ganesan,
Seebeck coefficient study on Mn doped $\text{YBa}_2\text{Cu}_3\text{O}_y$
Phys. Rev. B59, 7178 (1999)
- 2 E. Isaac Samuel and V. Seshu Bai,
Temperature and field variation ac susceptibility on Mn doped $\text{YBa}_2\text{Cu}_3\text{O}_y$ Superconductor
(Communicated)
- 3 E. Isaac Samuel and V. Seshu Bai,
ac MH loop measurements on Mn doped $\text{YBa}_2\text{Cu}_3\text{O}_y$ Superconductor
(Communicated)
- 4 E. Isaac Samuel, V. Seshu Bai, N. Harish Kumar and S. K. Malik
DC magnetic properties of Mn doped $\text{YBa}_2\text{Cu}_3\text{O}_y$ Superconductor
(Communicated)
- 5 E. Isaac Samuel, S. Ravi and V. Seshu Bai,
Excess conductivity studies in para coherence region of Bi-Pb-Sr-Ca-Cu-O
superconductors.
Solid State communications 96, 441-444 (1995).